

ISSN number 0971 - 9709



IGU
Promoting Earth System Sciences

The Journal of Indian Geophysical Union

AN OPEN ACCESS BIMONTHLY JOURNAL OF IGU

VOLUME 29, ISSUE 5, SEPT. 2025



The Journal of Indian Geophysical Union (JIGU) Editorial Board	Indian Geophysical Union (IGU) Executive Council
Chief Editor O.P. Pandey (Geosciences), Hyderabad	President Dr.M. Ravichandran, Secretary, Ministry of Earth Sciences, New Delhi
Associate Editors Sandeep Gupta (Seismology), Hyderabad B. Srinivas (Geology, Geochemistry), Hyderabad M. Radhakrishna (Geosciences, Geodynamics), Mumbai Vimal Mishra (Hydrology, Climate change), Gandhinagar A.P. Dimri (Environmental Sciences), Mumbai	Vice Presidents Dr.Prakash Kumar, Director, CSIR-NGRI, Hyderabad Dr.A.P. Dimri, Director, IIG, Mumbai Ms. Sushma Rawat, Director (Exploration), ONGC, New Delhi Dr. T. Srinivas Kumar, Director, INCOIS, Hyderabad
Editorial Advisory Committee Solid Earth Geosciences: Vineet Gahlaut (Geodynamics), Hyderabad Prakash Kumar (Seismology), Hyderabad Shalivahan (Exploration Geophysics), Viskhapatnam Rajesh P. Srivastava (Geology, Geochemistry), Varanasi Pradeep Srivastava (Geological Sciences), Roorkee Parampreet Kaur (Geological Sciences), Chandigarh S.P. Sharma (Exploration Geophysics), Kharagpur Mita Rajaram (Geomagnetism), Mumbai J.R. Kayal (Seismology), Kolkata B. S. Dayasagar (Mathematical Geosciences), Bangalore Walter D. Mooney (Seismology, Natural Hazards), USA Ravi P. Srivastava (Exploration Geophysics), Norway Irina Artemieva (Lithospheric Studies), Denmark R.N. Singh (Theoretical and Environmental Geophysics), Ahmedabad Rufus D Catchings (Near Surface Geophysics), USA H.J. Kumpel (Geosciences, App. Geophysics, Theory of Poroelasticity), Germany Jong-Hwa Chun (Petroleum Geosciences), South Korea B.R. Arora (Geosciences), Dehradun Marine Geosciences and Atmospheric and Space Sciences: K.A. Kamesh Raju (Marine Geosciences), Goa Aninda Mazumdar (Geological Oceanography), Goa R. Bhatla (Meteorology), Varanasi Monika J. Kulshrestha (Atmospheric Sciences), New Delhi Subimal Ghosh (Climatology, Hydrology), Mumbai Archana Bhattacharya (Space Sciences), Mumbai Larry D. Brown (Atmospheric Sciences, Seismology), USA Saulwood Lin (Oceanography), Taiwan Xiujuan Wang (Marine Geology, Environment), China Jiro Nagao (Marine Energy, Environment), Japan Managing Editor: ASSSRS Prasad (Exploration Geophysics), Hyderabad	Honorary Secretary Dr. Abhey Ram Bansal, CSIR-NGRI, Hyderabad
	Joint Secretary Prof. M Radhakrishna, IITM, Mumbai
	Org. Secretary Dr. ASSSRS Prasad, CSIR-NGRI(Retd.), Hyderabad
	Treasurer Mr. Md. Rafique Attar, CSIR-NGRI, Hyderabad
	Executive Members Prof. P.Rajendra Prasad, Andhra University, Vishakhapatnam Prof. Devesh Walia, NIHU, Shillong Prof. Rajiv Bhatla, BHU, Varanasi Dr. Naresh Kumar, WIHG, Dehradun Dr. A. Vasanthi, CSIR-NGRI, Hyderabad Dr. P. S. Sunil, CUSAT, Kochi Dr. Manisha Sandhu, Kurukshetra University, Kurukshetra Dr. Uday Laxmi, Osmania University, Hyderabad Prof. Y. Srinivas, MS University, Tirunelveli Dr. Sumer Chopra, ISR, Gandhinagar Prof. Bikram Bali, Srinagar University, Srinagar Prof. Sanjit Kumar Pal, IIT (ISM), Dhanbad
EDITORIAL OFFICE Indian Geophysical Union, NGRI Campus, Uppal Road, Hyderabad- 500 007 Telephone: 91-4027012739, 27012332; Telefax:+91-04-27171564 Email: jigu1963@gmail.com, website: http://iguonline.in/journal/	

The Journal with six issues in a year publishes articles covering
Solid Earth Geosciences; Marine Geosciences; and Atmospheric, Space and Planetary Sciences.
The Journal is Financially supported by MoES, Govt. of India.

Annual Subscription

Individual Rs -1000/- per issue and Institutional Rs- 5000/- for six issues
Payments should be sent by DD drawn in favour of "The Treasurer, Indian Geophysical Union", payable at Hyderabad,
Money Transfer/NEFT/RTGS (Inter-Bank Transfer), Treasurer, Indian Geophysical Union, State Bank of India, Habsiguda Branch,
Habsiguda, Uppal Road, Hyderabad- 500 007
A/C: 52191021424, IFSC Code: SBIN0020087, MICR Code: 500002318, SWIFT Code: SBININBBHO9.
For correspondence, please contact, Hon. Secretary, Indian Geophysical Union, NGRI Campus, Uppal Road,
Hyderabad - 500 007, India; Email: igu123@gmail.com; Ph: 040 27012332

CONTENTS

Research Articles

- Hydro-geophysical assessment of aquifer zones in Niger semi-arid regions
Rehmat Khan , Tanvi Arora , Sohelkhan Pathan, Ronak Dahiya and Rishu Pandey 299
- Geomorphic study of the Late Quaternary-Holocene piedmont fans and fluvial terraces of Kota Dun, Kumaun Himalaya
Jonti Gogoi, Prabha Pandey, Anand K. Pandey and Devender Kumar 312
- Geospatial assessment of groundwater quality and its suitability for drinking and irrigation in semi-arid regions of Andhra Pradesh (India) using water quality index approach
Ravi Kumar Pappaka, Srinivasa Gowd Somagouni, Krupavathi Chinthala, and Pradeep Kumar Badapalli 321
- A geochemical study on the Lansdowne granite and granite gneiss, Garhwal Lesser Himalaya, Uttarakhand (India)
Deepa Arya, Gunjan Arya, R.B. Ananth 339
- Impact of triangular irregularity on the dispersion of SH-waves in a monoclinic crustal layer overlying a dry sandy medium
Tanishqa Shivaji Veer, A. Akilbasha and Vijay Kumar Kalyani 354
- Future projections of land evapotranspiration over India: Insights from Multi Model CMIP6 under SSP2-4.5 and SSP5-8.5
Garima Singh, Harshita Saxena and Sudhir Kumar Sing 367

Hydro-geophysical assessment of aquifer zones in Niger semi-arid regions

Rehmat Khan¹, Tanvi Arora^{1,2*}, Sohailkhan Pathan^{1,2}, Ronak Dahiya² and Rishu Pandey¹

¹Academy of Scientific and Innovative Research (AcSIR), Ghaziabad, 201002, India

²CSIR-National Geophysical Research Institute, Uppal Road, Hyderabad 500 007, India

*Corresponding Author: tanvi.ngri@csir.res.in

Abstract

Recognizing the critical role of groundwater as the primary drinking water source for millions worldwide, particularly in semi-arid regions like Niger, the UN Sustainable Development Goal (UN-SDG) aims to prioritize its sustainable management. Addressing water scarcity challenges through accessible, pure, and naturally filtered groundwater supports UN-SDG objectives for clean water and sanitation (Goal 6), ensuring its availability for domestic, agricultural, and industrial needs. This research contributes to the understanding groundwater potential zones and aquifer protective capacity in Niger's semi-arid region, supporting sustainable water resource management in Niger's semi-arid regions, Tillabery, Niamey, Dosso, Thoua, and Maradi. Using Vertical Electrical Sounding (VES) techniques, 166 data points were collected employing the Schlumberger electrode configuration. Geoelectric properties (resistivity and layer thickness) were derived, and Dar-Zarrouk parameters were calculated. Contoured maps visualizing longitudinal conductance (S), transverse resistance (T), and electrical anisotropy (λ), helped classify groundwater potential zones. The northeastern part showed low resistance, indicating a good groundwater potential zone. The aquifer is encountered at a depth of 11 m to 15 m in a sandy clay environment. Assessment of longitudinal conductance revealed a moderate to very good aquifer protective capacity, particularly in the southwestern and central-western sectors. To validate, eighteen borehole sites were analyzed, correlating findings with borehole drilling data to create a 3D aquifer thickness model. We found that the aquifer thickness is from 1.5 to 3.5 meters in certain regions exhibiting robust protective capacity, enhancing aquifer resilience against surface contamination. Analysis of the electrical anisotropy coefficient provided insights into geological structures like fractures and bedding planes, influencing fluid flow dynamics and contaminant movement.

Keywords: Vertical Electrical Sounding (VES), Dar-Zarrouk parameters, Arc Scene, 3D Aquifer model, Semi-arid region, Niger

INTRODUCTION

Niger is a country located in the African continent within the semi-arid Saharan region, and its main challenge is aridity. The study area is mostly desert and the bulk of the population relies on the Niger River for agriculture and irrigation. (Arora et al., 2023). The population relies on groundwater for essential drinking and domestic water needs, which requires a comprehensive understanding of the aquifer in the challenging hard rock terrain. Reliable information on groundwater recharge mechanisms and rates are scarce in this region, so reliance on seasonal rainfall and flooding is evident to replenish shallow aquifers. Unfortunately, diminishing rainfall by 25-40% since 1930-1960, has made this vital water source precarious (Nicholson et al., 2000). Although recharge rates are generally low across the country, some areas witness adequate water yields from the dug wells, albeit in scarce numbers. Compelling groundwater exploration in the Niger, demands a systematic scientific approach due to inherent uncertainties. With the climate patterns shifting and rainfall increasingly erratic, a nuanced understanding of aquifer composition becomes pivotal for sustainable water management. Addressing these challenges will ensure water security and resilience in evolving climatic conditions.

Leduc et al. (1997) used hydrodynamics and geochemical methods during the early 1990s to evaluate natural groundwater recharge on a regional scale in unconfined aquifers. To determine delineation of aquifer zones, they relied on direct current (DC) resistivity soundings, which is a widely used geophysical technique (Van Nostrand and Cook, 1960;

Zohdy, 1974; Koefoed, 1979; Patra and Mallick, 1980; Dutta et al., 2006; Dar et al., 2017; Arora et al., 2023). The electrical resistivity of the subsurface is closely linked to pore spaces, with layers featuring larger pores filled with fluid exhibiting lower resistivity than those with more compact pore structures. Groundwater exploration can be challenging due to the geological heterogeneity of the subsurface. It introduces complexities, highlighting the need for a nuanced understanding of subsurface geological variations. Thus, a scientific approach integrating hydrodynamics, geochemistry, and geophysical techniques can contribute to a more comprehensive understanding of natural groundwater recharge dynamics on a regional scale.

Groundwater exploration was conducted in the present study area, utilizing 166 electrical-sounding surveys by employing the Schlumberger electrode configuration. The gradual variation in DC sounding provides a reliable representation of subsurface changes with depth, similar to other geophysical methods. This data was then inverted to create a representative subsurface model. To enhance the reliability of the information, data from 18 specific sites were cross-referenced with borehole drilling data. These records provided a comprehensive understanding of subsurface characteristics, enabling the identification and delineation of potential aquifer zones. The obtained information was validated at 18 specific sites through correlation with borehole drilling data. This integration of data from borehole drilling served as a critical source, offering a comprehensive understanding of subsurface characteristics. This approach facilitated the delineation of potential aquifer zones tailored specifically for prospecting

drinking water resources. The combination of electrical sounding surveys and borehole drilling data analysis, enhances the scientific rigor and accuracy of the groundwater exploration process, particularly in urban settings like Niger.

STUDY AREA AND HYDROGEOLOGY

Situated in the heart of West Africa, Niger is a landlocked country officially known as the Republic of Niger. It shares borders with several neighboring countries, including Algeria, Libya, Chad, Nigeria, Benin, Burkina Faso, and Mali (Figure 1). The study area boasts a diverse topography encompassing deserts, semi-arid plains, mountains, and fertile valleys. The region's topographic elevation varies from 174 to 302 meters above mean sea level (msl). The Sahara desert dominates the north, while the Sahel, a transitional zone between desert and savanna landscapes, characterizes the southern region. The study area includes, Tillabery, Niamey, Dosso, Tahoua, and Maradi of Niger regions, together with Tillabery, show casing a hard rock terrain having an Archean basement. Figure 2 shows the geology and soil maps of the study area. Granite is the primary rock type, with gneisses serving as a basement for intrusive rocks. The gneisses are a massive, rich in quartz, feldspar, and mica minerals, and the area is highly dissected with lineaments such as dolerite dykes and quartz veins (Arora et al., 2023). The Niger river, one of Africa's longest rivers, is a significant geographical feature traversing the Niamey

region in the Niger. Originating in the Guinea Highlands, it converges with its primary tributaries, the Bani and Milo rivers, before flowing through Mali and entering into Niger. The Niger river, coursing eastward, culminates its journey in the Atlantic ocean via Nigeria. Along the Niamey region, geological formations reflect a history of erosion and deposition, intricately shaping the landscape over time. These processes have sculpted the region's geological characteristics (Chappell and Oliver, 1997). The Dosso region, located in a sedimentary terrain, is characterized by abundant lacustrine and marine deposits, particularly fine to medium-grained sand. Notably, the Niger river has Gondwana sandstone deposits in the Dosso. Niamey, Tahoua, and Maradi regions which are characterized by sedimentary terrains composed mainly of laterites and sandstone. In Maradi's composite soil cover, dry laterites and sand is prevalent. These geological features give each region its unique sedimentary composition and topography. Meanwhile, the Dosso region, located along the Niger river, boasts an abundance of Gondwana sandstones and fine to medium-grained sand. The Niger river is renowned for its vast alluvial deposits, which consist primarily of sedimentary materials like sand, silt, and clay. These deposits are formed as the river continually erodes adjacent rocks and deposits sediment along its path. The fertile floodplains make the Niger river, a critical water resource for agriculture in the area.

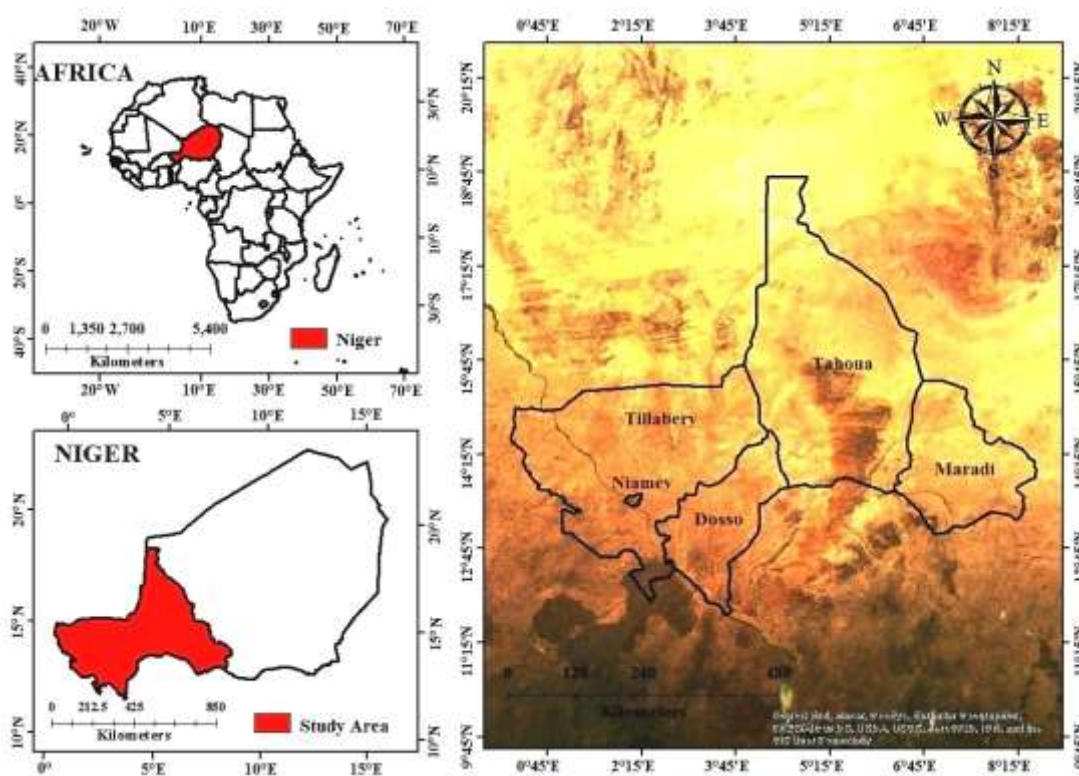


Figure 1. Location map of the study area including cities of Niamey, Tillabery, Tahoua, Maradi and Dosso in Niger.

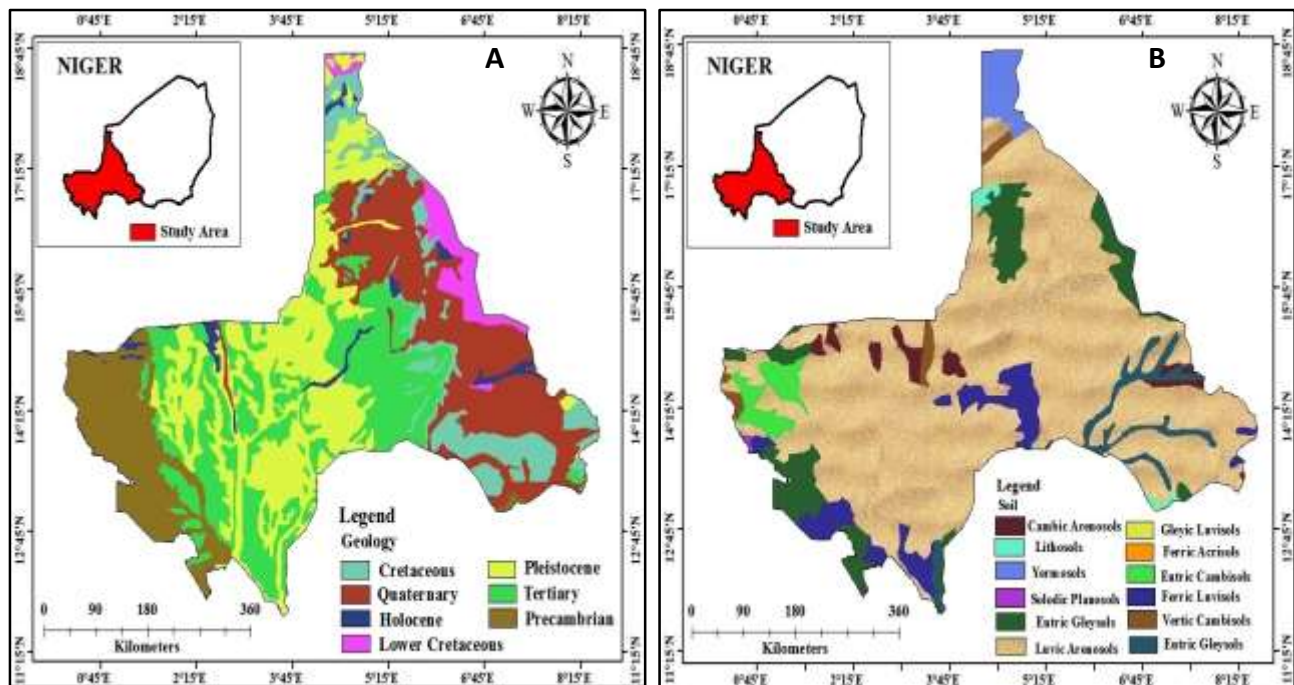


Figure 2. (A) Geology map, and (B) Soil map of the study area in Niger.

A previous study done by Arora et al. (2023) has recorded water table depths ranging from 3 to 50 m below ground level in southwest Niger; the potential aquifer zones identified are located in sandy clay or sandstone formations, exhibiting unconfined and confined aquifers (Vouillamoz et al., 2007), attributed to the accumulation of unconsolidated formations above the basement. This complex interaction between geological formations and water movement dynamics, highlight the importance of impermeable layers in determining groundwater conditions. Along the Niger river and its tributaries, diverse alluvial deposits with varying compositions, serve as potential aquifers (Thevoz et al., 1994). Accurate determination of layer thickness is thus essential. The Niger river plays a significant role in the hydrogeology of the Niamey region, recharging local aquifers through direct infiltration. Therefore, sustaining ecosystems and supporting human activities rely heavily on replenishing groundwater systems along the river.

The main objective of the study is to identify potential groundwater resources within the five regions (Niamey, Tillabery, Tahoua, Maradi, and Dosso) of Niger, using the integration of the vertical electrical sounding and lithological information. This involves mapping the extent and thickness of the aquifer utilizing GIS. By integrating various datasets and analytical techniques, the spatial distribution of groundwater resources and their availability for sustainable utilization is to be assessed.

METHODOLOGY

The Vertical Electrical Sounding (VES) method, a geophysical electrical survey technique, efficiently probes the earth's shallow subsurface resistivity structure. Renowned for its convenience and minimal environmental impact, it utilizes direct current as its energy source. Resistivity is the inherent property of a material that quantifies its resistance to electrical current flow. Ohm's Law describes the relationship between voltage (V), current (I), and resistance (R) in a circuit, is given by

$$V=I \times R \quad (1)$$

The SYSCAL resistivity equipment was used as the main instrument for this investigation. It worked as a signal averaging system, calculating voltage by multiplying current and a constant field configuration. The apparent resistivity values were plotted on a bi-logarithmic sheet, with the X-axis denoting the distance AB/2 and the Y-axis indicating the resistivity values. We created resistivity models and used the IX1D (Interpex, 2006) computer software to interpret the data.

The lithological model is constructed from stacked raster surfaces, representing the vertical arrangement of sedimentary layers, with the highest surface being the Digital Elevation Model (DEM) and the lowest being the upper boundary of ancient Precambrian basement rocks. By visualizing lithostratigraphic logs, this method accommodates various stratigraphic data sources, including boreholes, outcrops, and water wells.

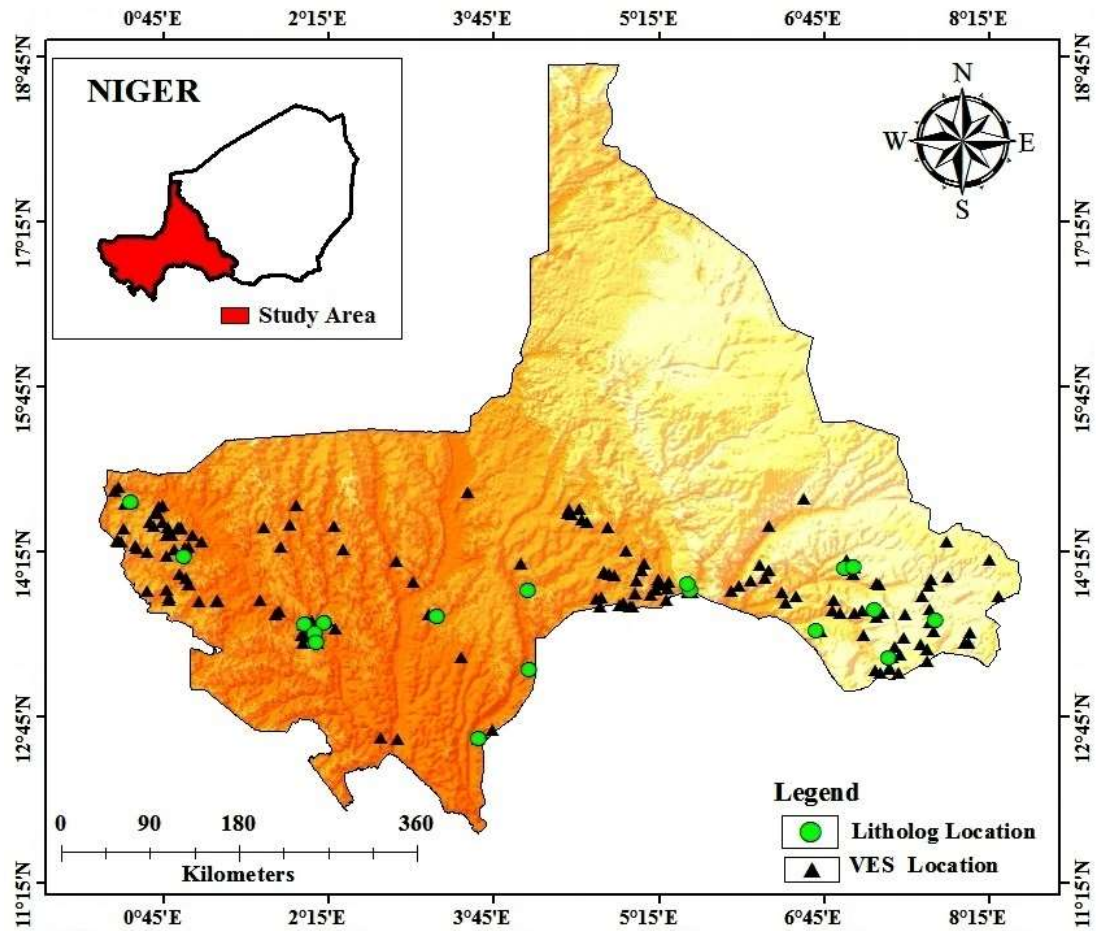


Figure 3. Map of the study area showing the location of Vertical Electrical Sounding (VES) and drilled litholog locations within the various regions of the study area. DEM: digital Elevation Model.

The study incorporates 18 locations with lithological data (Figure 3), encompassing three geological layer boundaries, each with distinct XYZ coordinates.

Dar-Zarrouk parameters

The Dar-Zarrouk (D-Z) parameters, which include transverse resistance (T) and longitudinal conductance (S), were first introduced by Maillet (1947). These parameters, especially longitudinal conductance (S) and transverse resistance (T), are crucial for interpreting subsurface characteristics and identifying water-bearing zones (Sri Niwas and Olivar, 2003). Transverse resistance measures the resistance perpendicular to groundwater flow for a unit cross-sectional area. In contrast, longitudinal conductance measures the conductance parallel to groundwater flow for a unit cross-sectional area. These parameters are essential in resistivity soundings, as they help determine the hydrological properties of aquifers. In this study, we analyze the data using the D-Z parameters, specifically longitudinal unit conductance (S), transverse unit resistance (T), and electrical anisotropy (λ), as outlined by Batte et al. (2010) and Singh et al. (2004).

Let us consider a prism of unit cross-section, which is characterized by its thickness 'h' and resistivity ρ . Then, the resistance (T) perpendicular to the face of the prism (Mondal et al., 2013) can be written as:

$$T = h \times \rho \quad (2)$$

and

$$S = \frac{h}{\rho} \quad (3)$$

It is considered that the prism consists of n-geoelectric layers and is entirely characterized by its thickness h_1, h_2, \dots, h_n and resistivity's $\rho_1, \rho_2, \dots, \rho_n$, respectively. Then, the total resistance of the current flowing perpendicular to the layers will be the sum of resistance offered by each layer and that can be expressed as follows

$$T = h_1\rho_1 + h_2\rho_2 + \dots + h_n\rho_n \quad (4)$$

or

$$T = \sum_{i=1}^n h_i \rho_i \quad (5)$$

Where T is transverse resistance.

The transverse resistivity to the current flowing perpendicular to the layers is given by

$$\rho_t = \frac{T}{H} \quad (6)$$

where H is the sum of n layers in the prism.

Similarly, the total conductance of the current flowing parallel to the layers is given

$$S = \frac{h_1}{\rho_1} + \frac{h_2}{\rho_2} + \dots + \frac{h_n}{\rho_n} \quad (7)$$

or

$$S = \sum_{i=1}^n \left(\frac{h_i}{\rho_i} \right) \quad (8)$$

which is longitudinal conductance.

The longitudinal resistivity of the current flowing parallel to layers is given by

$$\rho_l = \frac{H}{S} \quad (9)$$

and the coefficient of anisotropy (λ) is given by

$$\lambda = \sqrt{\frac{\rho_t}{\rho_l}} \quad (10)$$

The above parameters were used to delineate the subsurface freshwater zones in the study region and determine aquifer protective capacity.

3D Modeling in Arc Scene

The available borewell data was used to create a lithology unit in Arc Scene. Arc Scene was used to improve mathematical precision while interpolating surfaces for analysis and building sedimentary packages for layers. Depending on the dispersion and trends in the data points, point clouds for each interpreted surface were imported into Arc Scene and interpolated with either inverse distance weighting (IDW) or Kriging. For surfaces having a clear trend to the data points, such as a steady inclination in one direction, a Universal Kriging (UK) interpolation method using a Semi-variogram model of "linear with ordinary" was applied. The UK interpolation approach extends ordinary kriging by integrating the local trend inside the chosen neighborhood search radius as a smoothly evolving function of the coordinates (Li and Heap, 2008). For surfaces with higher imperfections, such as the top surface of a sedimentary package containing huge boulders, ordinary kriging with a spherical semi-variogram

model, or IDW, was utilized for interpolation. IDW determines the values in the voids between the points using a linear combination of values from sampled points.

In this case, the values of the nearest data points are weighted more heavily in the distance function for interpolation, presuming that they are more comparable to the unsampled region than the values of the data points further away (Kristine and Karlsen, 2019). The outcomes of these interpolations consist of raster data, wherein each cell holds a single height value with a spatial resolution of 0.16. These interpolated raster datasets were then transformed into a Triangular Irregular Network (TIN) model, creating a three-dimensional representation. It is observed that the points extracted from the CSV file alongside the corresponding TIN-generated surface derived from Grid 2. The final stage in constructing a three-dimensional model for underground sedimentary layers involved utilizing the "Extract Package" tool in Arc Scene. This tool facilitated the generation of radar packages between specific radar surfaces, culminating in representing subsurface sedimentary sequences in a 3D format. Generating TIN (Triangulated Irregular Network) models, through interpolation, was explicitly undertaken to obtain 3D outcomes for Grid 2. The data at 50 MHz was initially acquired in 2D profiles, which inherently constrains the 3D representation of subsurface structures. The points corresponding to the borehole data beneath the ground, were transformed into polylines to address this limitation. This transformation was accomplished utilizing Arc Scene's Data Management tools' "Points to Line" function. Subsequently, the "Extrusion" technique was applied to the layer properties of each point dataset, allowing for the elevation-based extension of the point data into 3D space.

RESULTS

Aquifer characteristics using the Dar-Zarrouk parameters

The Dar-Zarrouk (DZ) parameters were systematically computed for the subsurface layers encompassing local aquifers composed of sand, clay-mixed sand, weathered formations, and fractured rocks extending down to the bedrock within the investigated region. Potential groundwater zones were delineated by the geoelectric characteristics derived from resistivity interpretation and the calculated DZ parameters. The assessment of groundwater potential in the study area hinged upon using maps generated from VES interpretation results, explicitly focusing on the anisotropic coefficient, transverse resistance, and longitudinal conductance. These maps serve as valuable tools for identifying optimal yield areas within the aquifer, particularly in the challenging terrain of shallow aquifers within hard rock formations. The presentation and discussion of these maps offer valuable

insights into realistic groundwater modeling within the specified geological context.

Longitudinal conductance (S)

The S map of the study area is divided into three potential zones: good, moderate, and low. The area's longitudinal conductance (S) ranges from 0.02 Siemens at VES-136 to 9.6 Siemens at VES-59, with a contour interval of 1. Areas with an S value of less than 2 Siemens is considered good groundwater potential zones, those with S values between 2–4 Siemens are moderate, and those above 4 Siemens are of low potential zones (Ndatuwong and Yadav, 2015). Figure 4 shows low S values in 83% of the study area, while 8% have moderate S values, and 9% have high S values.

Aquifer protective capacity can be classified into poor, weak, moderate, good, very good, and excellent using longitudinal conductance (S) values (Oladapo et al., 2004). Clayey overburden is known to have high longitudinal conductance, protecting against contaminants permeating the underlying aquifer (Oladapo and Akintorinwa, 2007).

Table 1 shows that the modified classification system quickly categorizes an area's protective capacity. The longitudinal conductance map (Figure 4) shows that 38.54% of the area falls within the good protective capacity, 5.42% within the

very good protective capacity, and 1.20% within the excellent protective capacity. About 35.54% fall within the moderate protective capacity, and 7.85% within the poor protective capacity. These results indicate that the study area is dominated by moderate to excellent protective capacity.

Transverse Resistance (T)

Aquifer transmissivity indicates the ability of the layer of known hydraulic conductivity to transmit fluids through its entire thickness. On a purely empirical basis, it can be admitted that the transmissivity of an aquifer is directly proportional to transverse resistance (Henriet, 1976; Ward, 1990). The transverse resistance ranges from 126.79 Ωm^2 at VES 154 to 80101.66 Ωm^2 at VES 34 as shown with contour interval 10,000 Ωm^2 in Figure 5. It is classified into good, moderate, and low potential zones. Values of T that range between 20,000–40,000 Ωm^2 and those above 40,000 Ωm^2 are considered moderate and good potential zones respectively and while values less than 20,000 Ωm^2 , are considered low potential zones (Ndatuwong and Yadav, 2015). Figure 5 shows low T values in 73% of the study area while 17% have moderate T values, and 10% have high T values. This suggests that about 27% of the study area is characterized by moderate to high transverse resistance, considering the groundwater potential zone. This increasing T value also indicates the high transmissivity of the aquifer

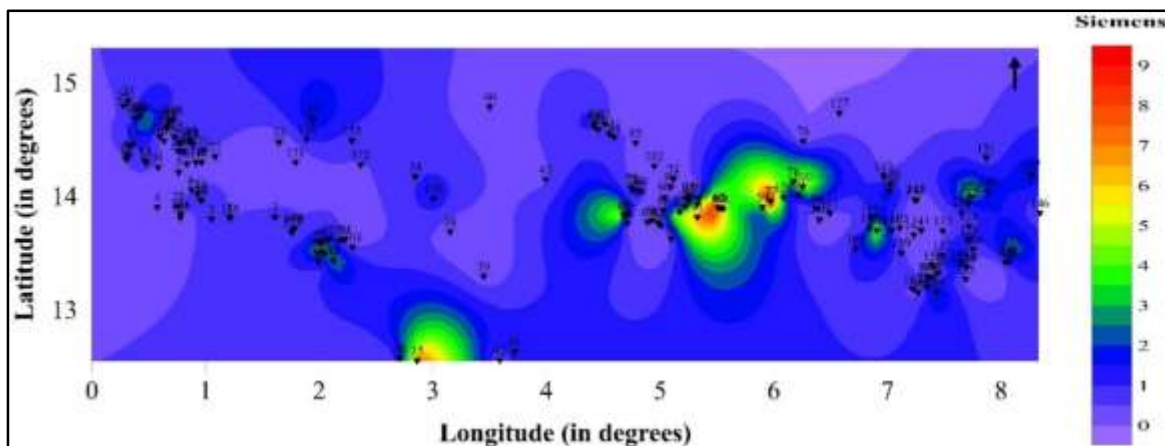


Figure 4. Spatial distribution of longitudinal conductance (S) in Siemens in the study area.

Table 1. Modified longitudinal conductance/ protective capacity ratings (Oladapo et al., 2004)

Longitudinal conductance (S)	Protective capacity rating
<0.1	Poor
0.1–0.19	Weak
0.2–0.69	Moderate
0.7–4.9	Good
5–10	Very good
>10	Excellent

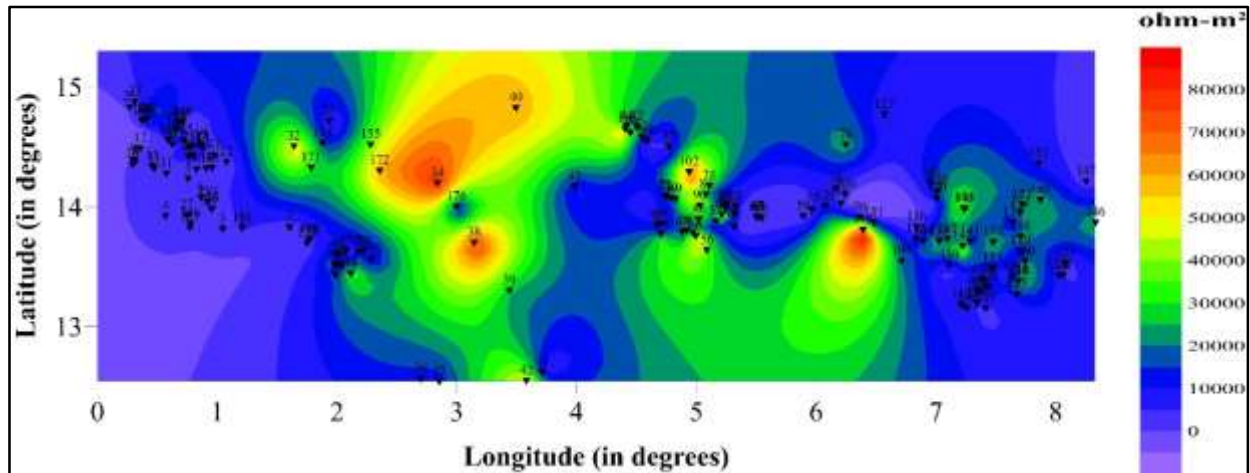


Figure 5. Spatial distribution of transverse resistance (T) in Ohm-m² in the study area.

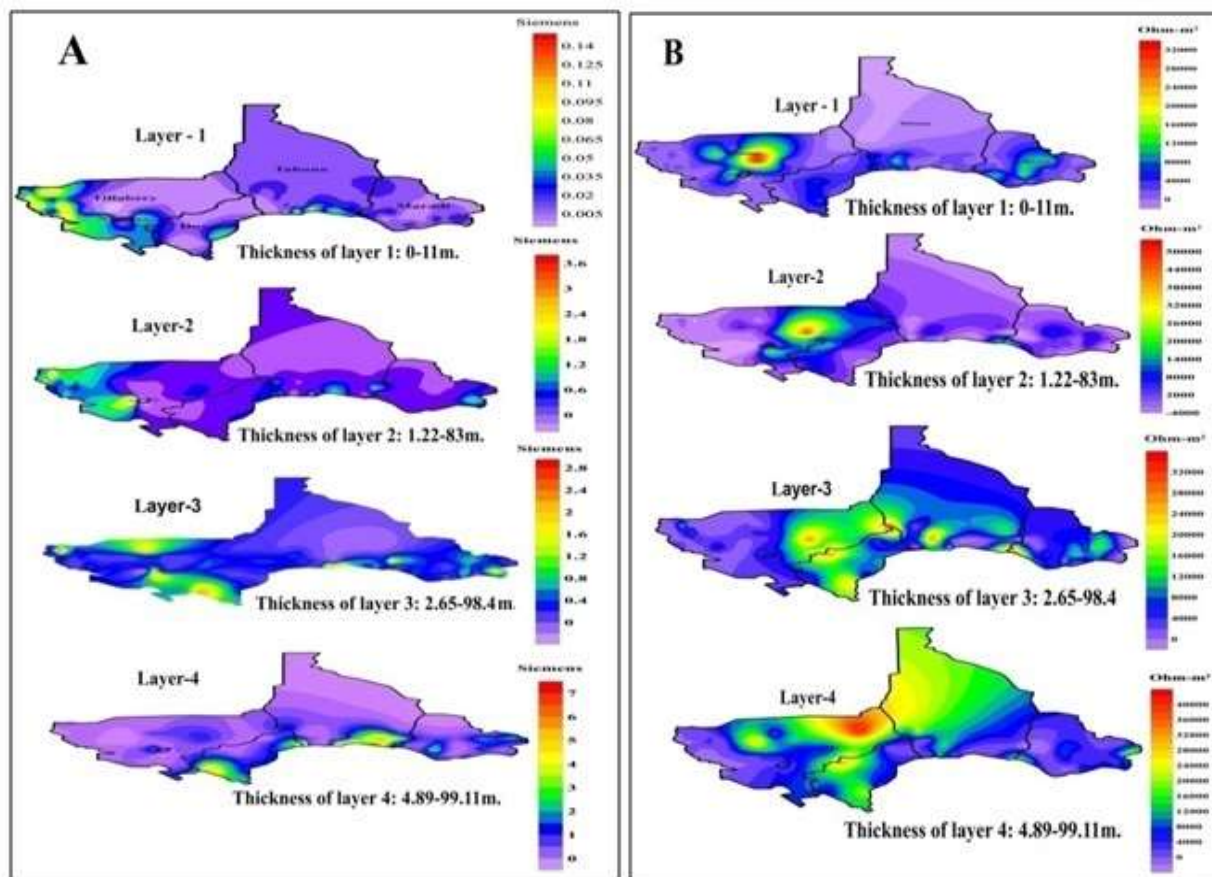


Figure 6. (A) Layer-wise spatial variation of longitudinal conductance in Siemens, and (B) transverse resistance (T) in Ohm-m² in the study area.

Depth-wise layered variation of longitudinal conductance (S) and transverse resistance (T)

Based on the observations illustrated in Figure 6, it is evident that there is a discernible pattern in the longitudinal conductance (S) and transverse resistance (T). Notably, there is a horizontally elongated zone in both conductance and

resistance. Further analysis of the borehole data corroborates these observations. Figure 6 clearly represents the variation in S and T values as we delve deeper into the earth, from the first layer to the last. The S value increases from the top to the bottom, with the second and third layers displaying moderate S values that suggest promising potential zones. Similarly, the

second and third layers in the transverse resistance map show moderate values, indicating good aquifer transmissivity. Thus, based on the findings in Figure 6, we can conclude that the second and third layers, from a depth of 11 m to the third layer, may harbor a good groundwater potential zone.

Electrical anisotropy

Incorporating transverse and longitudinal resistivity introduces the anisotropy coefficient, which measures basement terrain heterogeneity resulting from near-surface effects, weathering, and structural elements (Adelusi et al., 2014). The values of longitudinal resistivity and transverse resistivity are used to compute anisotropic coefficient. The longitudinal resistivity value ranges from 9.64 Ωm at VES-20 to 1885.54 Ωm at VES-95. The value of longitudinal resistivity indicates the geoelectric inhomogeneity in the subsurface (Murali and Patangay, 1998). The transverse resistivity value ranges from 3.55 Ωm at VES-8 to 74001 Ωm at VES-95. According to Salem (1999)'s observation, transverse resistivity (ρ_t) tends to be greater than longitudinal resistivity (ρ_l). This suggests that current flow and hydraulic conduction along lithological boundaries (longitudinal) are more robust than perpendicular to the boundary plane.

The anisotropic coefficient typically range from 1 to 2, as noted by Zohdy et al. (1974) and Dutta et al. (2006), which is influenced by rock hardness and compaction. Areas with higher rock hardness and compaction are associated with higher coefficients, indicating lower porosity and permeability. According to Keller and Frischknecht (1966), this parameter measures the competency of subsurface materials. In addition, it is vital in identifying areas with high porosity and permeability and, thus, used in mapping groundwater potential zones. In the studied region, this

coefficient was utilized to identify subsurface freshwater zones and evaluate the aquifer's protective capacity. Understanding such zones helps delineate the distribution of porous and permeable layers within the aquifer system.

The study area's anisotropy coefficient varies from 1 at VES-154 to 4.17 at VES-44 (Figure 7). This parameter is handy in identifying groundwater potential zones, with values of 1.5 or lower indicating high porosity and permeability. The anisotropy coefficient map categorizes areas with values <1 as low potential, between 1 and 1.5 as good potential, and values >2 as areas with lower porosity and permeability (Keller and Frischknecht, 1966). This comprehensive analysis provides valuable insights into subsurface characteristics and identifies areas with favorable groundwater potential for further exploration and resource management.

Aquifer Thickness Map

The creation of the 3D Lithological model serves the purpose of facilitating hydrogeological modeling of the Niger sands groundwater. The geological surfaces, obtained by interpolating borehole data, define the sedimentary formations' spatial and vertical extents. The raster surfaces constituting the geological model act as practical barriers, enabling the precise delineation of aquifers for hydrogeological modeling (Dar et al., 2017). When viewed from a northeast perspective, the depiction reveals the presence of alluvial sediment deposits along the Niger river and its tributaries, which are markedly different from the eastern region, where the stratigraphic sequence is more comprehensive. In the latter area, sedimentary layers span from the Quaternary period to the entire Proterozoic series, ultimately reaching the Precambrian bedrock.

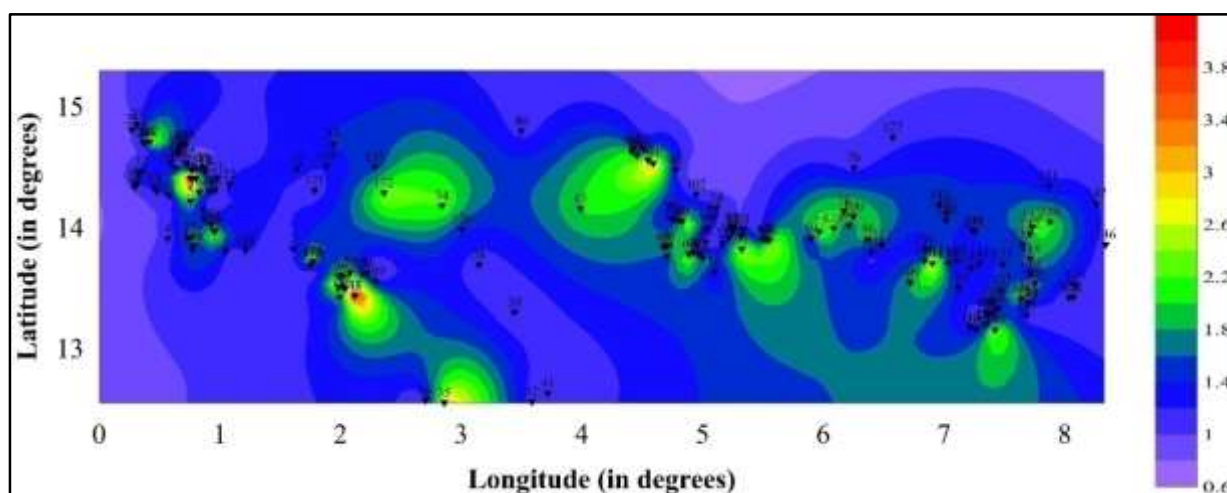


Figure 7. Spatial distribution of electrical anisotropy coefficient (λ) in the study area.

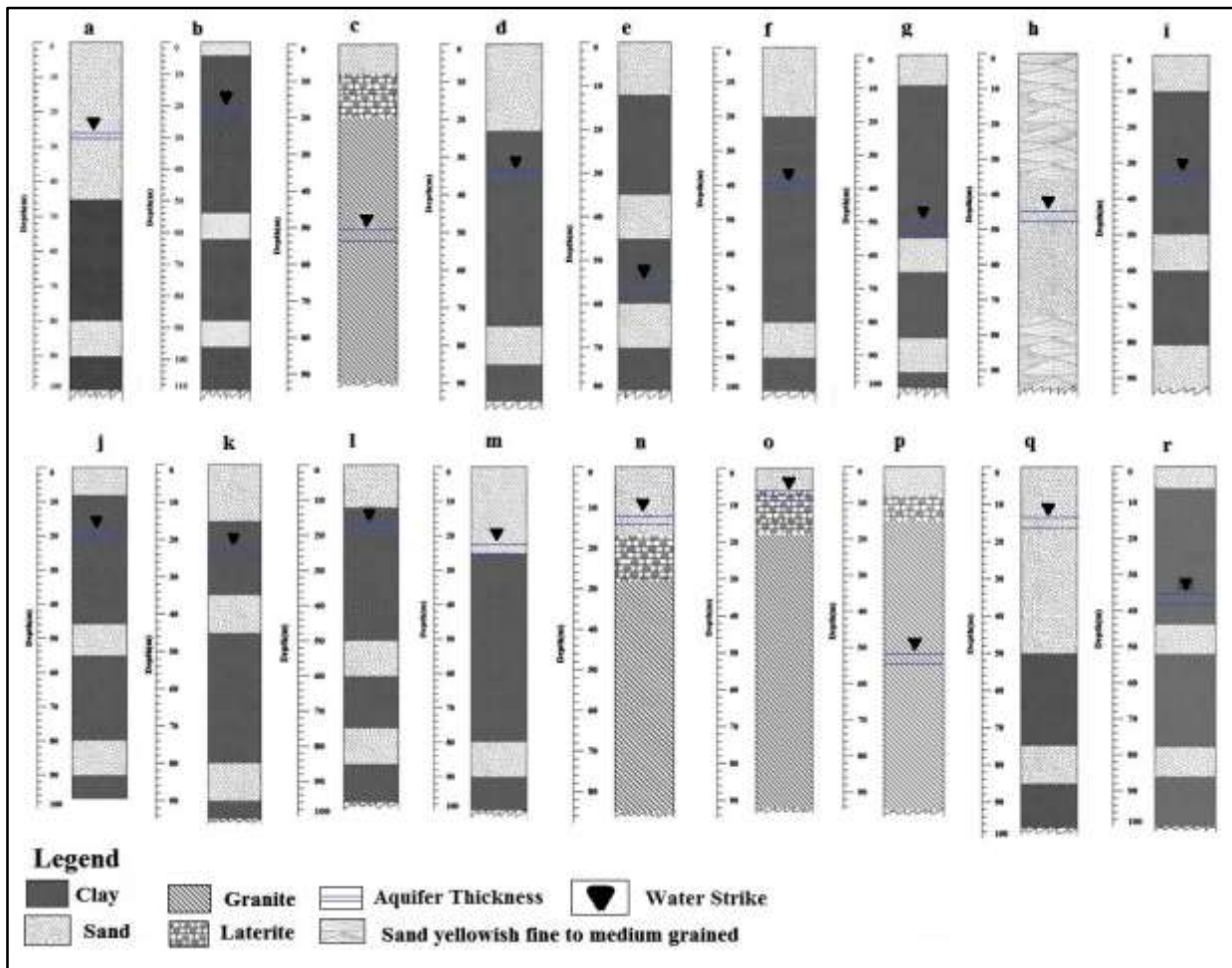


Figure 8. Details of the 18 litholog sites down to a depth of 110 m, revealing various geological litho-units. (a) BalideySoujedy, (b) Karki, (c) Wadata, (d) AngoulMayaki, (e) GuidanDamou, (f) Guidan Karo, (g) Guidan Kata, (h) GuidanTokkou, (i) Toudawa, (j) GorouKongou, (k) SoudourePeulh, (l) TchroudiElhSadoua, (m) Timire, (n) Dabagawa I, (o) GuidanBararou, (p) KozoroHahi, (q) Malbaza and (r) Bouloukogo.

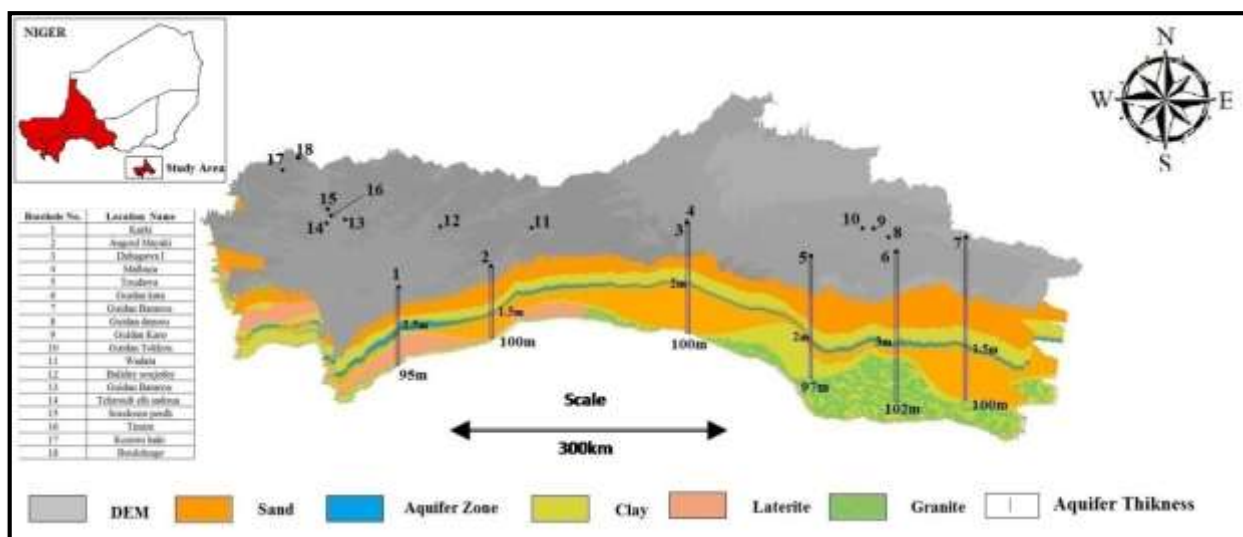


Figure 9. Aquifer thickness distribution spatial patterns and variability in the studied area

The interpolation of drilling data results in raster top surfaces for each geological layer, allowing the visualization of boreholes, outcrops, and other geological data sources as lithological columns. These modeled geological layers can be displayed collectively or individually using Arc Scene, offering clear visualization. 18 locations with lithological data have been charted within sedimentary deposits, with eight of them identified as aquifers in which Karki, Angoul Mayaki, Dabagawa, Toudawa, Guidan kata, and Guidan Bararou, consist of sand/granite (SG), and the sub-sand/granite laterite (SSGL). In the study areas of northern, southern-central, and southeastern regions, the presence of sub-sand/granite (SSG) is prevalent.

As per Table 2, the litholog of Balidey Soujeday and Malbaza, correlates very well with the VES locations 34, 37, 38, 166,

58, 70, 69, and 90. Balidey Soujeday aquifer thickness lies in a range of 1.5 to 4.5 m, and Malbaza aquifer thickness in a range of 1.5 to 5 m. The litholog of Wadata, Guidan Karo, Guidan Kata, Guidan Tokkou, and Gorou Kongou, correlates very well with the VES locations 42, 79, 120, 121, 134, 137, 138, 100, 101, 125, 126, 127, 141, 120, 121, 134, 135, 136, and 50. The thickness range in these locations varies from 2 to 5 m. The litholog data of Angoul Mayaki and Timire, correlates moderately with the VES locations 38, 44, 45 and 48, where the aquifer thickness lies within a range of 3 to 8 m, because the aquifer present here is, clay saturated and due to the presence of clay, the resistivity value show high aquifer thickness. The litholog data of Karki and Kozoro Hahi correlates at the limit with the VES location 35, 36, 40, 41, 5, 6, 16, 17, 18, 151. Karki aquifer thickness lies in a range of 4 to 8 m, while Kozoro Hahi aquifer lies in a range of 2 to 5 m.

Table 2. Comparison between aquifer thicknesses from the litholog and VES data.

Sr. No.	Litholog name	Latitude	Longitude	Aquifer thickness (m)	VES Locations in the vicinity	Aquifer thickness (m) from VES Data	Remarks
1	Balidey Soujeday	13.666	3.233	1.5	34, 37, 38, 166	1.5-4.5	Correlate very well
2	Karki	12.55	3.6	2.5	35, 36, 40, 41	4-8	Correlative at the limit
3	Wadata	13.893	4.051	2	42, 79	2-5	Correlate very well
4	Angoul Mayaki	13.176	4.070	1.5	38	3-8	The aquifer present here is clay-saturated and due to the presence of clay, the resistivity value shows high aquifer thickness.
5	Guidan Damou	13.718	7.2027	2.8	98, 106, 132, 133,	2.5-6	Correlate very well
6	Guidan Karo	14.0988	6.933	2	120, 121, 134, 137, 138	2-5	Correlate very well
7	Guidan Kata	13.2833	7.333	3	100, 101, 125, 126, 127, 141	2-5	Correlate very well
8	Guidan Tokkou	14.112	7.018	2.5	120, 121, 134, 135, 136	2-5	Correlate very well
9	Toudawa	13.527	6.676	2	92, 102	1-5	Correlate very well
10	Gorou Kongou	13.606	2.202	2.2	50	2-5	Correlate very well
11	Soudoure Peulh	13.590	2.024	2.5	43, 52	2-6	Correlate very well
12	Tchroudi ElhSadoua	13.511	2.125	2.5	46, 47, 49	3-6	Correlate very well
13	Timire	13.430	2.136	2.5	44, 45, 48	3-8	The aquifer present here is clay-saturated and due to the presence of clay, the resistivity value shows high aquifer thickness.
14	Dabagawa I	13.902	5.529	2.5	55, 57, 59, 60	1-6	Correlate very well
15	Guidan Bararou	13.622	7.754	1.5	109, 111, 110,	1-4	Correlate very well
16	Kozoro Hahi	14.206	0.929	1.7	5, 6, 16, 17, 18, 151	2-5	Correlative at the limit
17	Malbaza	13.960	5.507	2	58, 70, 69, 90	1.5-5	Correlate very well
18	Boulokogo	14.697	0.441	3.5	24, 26, 152, 153	3-5	Correlate very well

The litholog data of Tchroudi ElhSadoua and Boulokogo correlates quite well with the VES locations 46, 47, 49, 24, 26, 152, and 153. Tchroudi ElhSadoua aquifer thickness lies within a range of 3 to 6 m and Boulokogo aquifer, in a range of 3 to 5 m. Similarly, the litholog data of Guidan Damou and Soudoure Peulh correlates very well with the VES locations 98, 106, 132, 133, 43, and 52. At Guidan Damou, aquifer thickness lies in a range of 2.5 to 6 m, and Soudoure Peulh, 2 to 6 m. During the project, government of Niger has drilled eighteen deep exploratory boreholes in five regions (Tillabery, Niamey, Dosso, Thoua, and Maradi) in order to validate the geophysical results. The depth of each borehole is around 90 m to 110 m. All the drilled borehole lithologs were studied in detail for the sand property and for their hydrogeological significance (Figure. 8). It was seen that the alternate bands of sand with clay and sand from near surface layer to the bottom 110 m depth is seen at Karki site in Dosso, while sand, clay, sand, fine sand up to 50 m depth, later alternate bands of sand and fine sand, was depicted at the Guidan Tokkou site until 90 m depth. This illustrates the layered structure of the alluvium formation in the study area.

The southwestern region is potentially a significant SG and SSGL recharge area. The lithological model indicates the presence of sand deposits at the land surface, and water well records suggest that these deposits may be relatively thicker to approximately 25 meters. The thickness of the SSGL in this region ranges from 28 to 85 m in the subsurface. While it is improbable that the SSGL aquifer is directly in contacts with the bedrock aquifer, it is underlain by relatively continuous deposits of the Walworth Formation (ranging from 23 to 75 m). An aquifer thickness is 2.5 m in Karki, 1.5 m in Angoul Mayaki, 2 m in Dabagawa and Toudawa, 3 m in Guidan Kata and 1.5 m Guidan Bararou as shown in the Figure 9. Nonetheless, due to the erosion of the fine-grained sand (a regional aquifer confining unit) in the Niger river, this location could serve as an essential recharge area for the regional bedrock aquifer. As demonstrated in this study, the two-dimensional features initially defined in cross sections, can be transformed into a three-dimensional environment. These resulting 3D features can be visualized as fence diagrams within the exact Geographic Information System (GIS) environment using Arc Scene or exported to external software packages to construct 3D lithological models.

DISCUSSION

The geoelectric soundings with Dar-Zarrouk parameters and lithological models, helped to determine the groundwater potential zones and assess the protective capacity and thicknesses of the aquifers. The map of longitudinal conductance indicates that 83% of the study area has low S values, 8% has moderate S values, and 9% has high S values.

Using the unit conductance values, the protective capacity of the overburden in the area has been evaluated. The results show that 38.54% of the area falls within the good protective capacity, 5.42% within the very good protective capacity, and 1.20% within the excellent protective capacity. About 35.54% fall within the moderate protective capacity, and 7.85% fall within the poor protective capacity. These findings suggest that the study area has moderate to excellent protective capacity. The map of transverse resistance shows that low T values cover 73% of the study area, while 17% have moderate T values, and 10% have high T values.

The mapping of anisotropy coefficients aided in the delineation of the groundwater potential zones, with areas exhibiting values below 1 classified as having low potential, those between 1 and 1.5 deemed to have good potential, and values exceeding 2 indicative of lower porosity and permeability. The anisotropy coefficient, ranging from 1 to 4.17 across the study area, served as a valuable indicator of groundwater potential. Lower values (<1.5) correspond to areas with high porosity and permeability, while higher values (>2) indicate lower permeability. Further, the erosion of fine-grained sand along the Niger River, enhances the potential of this region as a critical recharge area for the bedrock aquifer. Utilizing advanced geospatial techniques, two-dimensional cross-sectional features are transformed into three-dimensional representations, facilitating enhanced visualization and understanding of lithological structures. The southwestern region exhibits significant potential as a recharge area for both shallow groundwater (SG) and semi-confined sandstone/granite/limestone (SSGL) aquifers. Geological investigations reveal the presence of surface sand deposits, estimated to be approximately 25 m thick, while subsurface analysis indicates SSGL thickness ranging from 28 to 85 m. Although direct contact between the SSGL aquifer and bedrock aquifer is unlikely, the SSGL is consistently underlain by the Walworth Formation, with thicknesses varying from 23 to 75 m. Notably, localized variations in aquifer thickness are observed across different locations, ranging from 1.5 to 3.5 m. This comprehensive analysis offers crucial insights into subsurface characteristics, guiding further exploration and facilitating effective water resource management strategies.

CONCLUSIONS

Based on the longitudinal conductance, it can be concluded that the study area is dominated by low S values, indicating an excellent potential zone with poor to moderate aquifer protective capacity. Also, based on transverse resistance, it can be concluded that about 27% of the study area is characterized by moderate to high transverse resistance, indicating a good groundwater potential zone. Areas with low longitudinal

conductance and high transverse resistance values are promising groundwater zones. Out of 166 studied locations, 44 had these characteristics. This means that 26.5% of the study area has a good potential for groundwater. A depth-wise variation of longitudinal conductance (S) and transverse resistance (T) was also studied. The results showed that in some places, the second layer and in others, the third layer, has favorable characteristics for groundwater potential.

The Dar-Zarrouk parameters also reveal heterogeneous anisotropic lithology in the study area. The concept coefficient of anisotropy measures the degree of in homogeneity in a basement terrain that arises from near-surface effects. The assessment of Dar-Zarrouk parameters for groundwater potential zones and aquifer protection studies, holds significant value in addressing societal concerns related to groundwater exploration and pollution prevention. These findings enhance our understanding of the complex geological characteristics in the study area and establish a foundation for future groundwater resource investigations utilizing the electrical resistivity method. Integration of geophysical data with borehole information, such as lithological logs and groundwater level measurements, enhances the accuracy of aquifer thickness assessments. On the bases of low longitudinal conductance and high transverse resistance values, 44 VES locations have shown good groundwater potential zone, and all these sites correlated very well with the 18 drilled boreholes where aquifer thickness lies with a range of 1.5 to 3.5 m.

Acknowledgements

The authors wish to thank the Director, CSIR-NGRI, Hyderabad for his support, encouragement and the permission to publish this paper. This work was carried out as a part of project supported by Government of Niger. The CSIR-NGRI library reference number of the manuscript is NGRI/Lib/2024/Pub-003.

Author credit statement

RK: Data curation, data analysis methodology, editing and processing of complete data. This work is a part of his doctorate thesis, TA: conceptualization, data curation, quality checks, methodology, funding acquisition, draft editing and revision and supervision, SP: data analysis, methodology, data structuring, RD: Methodology, data quality check, data curation, RP: preparation of maps

Data availability

DEM Data sourced from <https://earthexplorer.usgs.gov>; Soil from <https://www.fao.org>; geology from <https://certmapper.cr.usgs.gov> and litholog from Unpublished Project Report

Compliance with ethical standards

The authors declare that there is no conflict of interest and adhere to copyright norms.

References

- Adelusi, A.O., Ayuk, M.A. and Kayode, J.S., 2014. VLF-EM and VES: an application to groundwater exploration in a Precambrian basement terrain SW Nigeria. *Ann. Geophys.*, 57(1), 1–11.
- Arora, T., Kumar, S., Khan, R., Jalander, D. and Ahmed, S., 2023. Electrical imaging to decode the potential aquifer locations for water security in semiarid Niger, Africa. *Geosyst. Geoenviron.*, 2(2), 100072.
- Batte, A.G., Barifaijo, E., Kiberu, J.M., Kawule, W., Muwanga, A., Owor, M. and Kisekulo, J., 2010. Correlation of geoelectric data with aquifer parameters to delineate the groundwater potential of hard rock terrain in Central Uganda. *Pure Appl. Geophys.*, 167(12), 1549–1559.
- Chappell, A. and Oliver, M.A., 1997. Geostatistical analysis of soil redistribution in SW Niger, West Africa. In: E.Y. Baafi and N.A. Schofield (Eds), *Quantitative Geology and Geostatistics*, Vol. 8(2), pp. 961–972. Kluwer.
- Dar, F.A., Arora, T., Warsi, T., Devi, A.R., Wajihuddin, M., Grutzamer, G., Bodhankar, N. and Ahmed, S., 2017. 3-D hydrogeological model of limestone aquifer for managed aquifer recharge in Raipur of central India. *Carbonates and Evaporites*, 32, 459–471.
- Dutta, S., Krishnamurthy, N.S., Arora, T., Rao, V.A., Ahmed, S. and Baltassat, J.M., 2006. Localization of water bearing fractured zones in hard rock area using integrated geophysical techniques in Andhra Pradesh, India. *Hydrogeol. J.*, 14, 760–766.
- Henriet, J.P., 1976. Direct application of Dar Zarrouk parameters in groundwater survey. *Geophys Prospect*, 24(2), 344–353.
- Interpex, 2006, Golden Software, IX1D. One Dimensional Resistivity Interpretation Software. Golden Software Inc.
- Keller, G.V. and Frischknecht, F.C., 1966. *Electrical Methods in Geophysical Prospecting*. Pergamon, Oxford.
- Koefoed, O., 1979. *Geosounding Principles 1: Resistivity Sounding Measurements*. Elsevier Scientific Company, Amsterdam.
- Kristine, I. and Karlsen, H., 2019. 3D Subsurface Modeling based on Ground Penetrating Radar Survey of Glaciomarine Deposits – Hagadrag Aquifer, Norway. A sedimentological, hydrogeological and geophysical study. *Proc. Vol.*, p. 562, <https://api.semanticscholar.org/CorpusID:210293160>
- Leduc, C., Bromley, J. and Schroeter, P., 1997. Water table fluctuation and recharge in semi-arid climate: some results of the HAPEX-Sahel hydrodynamic survey (Niger). *J. Hydrology*, 188–189, 123–138.
- Li, J. and Heap, A.D., 2008. A review of spatial interpolation methods for environmental scientists. *Geoscience Australia, Record* 2008/23.
- Maillet, R., 1947. The fundamental equations of electrical prospecting. *Geophysics*, 12(4), 529–556.
- Mondal, N.C., Singh, V.P. and Ahmed, S., 2013. Delineating shallow saline groundwater zones from southern India using geophysical indicators. *Environ. Monit. Assess.*, 185, 4869–4886.
- Murali, S. and Patangay, N.S., 1998. *Principles and applications of groundwater Geophysics*, Published. by AEG, OU, Hyderabad, pp. 421

- Ndatuwong, L.G. and Yadav, G.S., 2015. Application of geo-electrical data to evaluate groundwater potential zone and assessment of overburden protective capacity in part of Sonebhadra district, Uttar Pradesh. *Environ. Earth Sci.*, 73, 3655–3664.
- Nicholson, S.E., Some, B. and Kone, B., 2000. A note on recent rainfall conditions in West Africa, including the rainy season of the 1997 ENSO year. *J. Clim.*, 13, 2628–2640.
- Oladapo, M.I. and Akintorinwa, O.J., 2007. Hydrogeophysical study of Ogbese, Southwestern Nigeria. *Global J. Pure and Appl. Sci.*, 13, 55–61.
- Oladapo, M.I., Mohammed, M.Z., Adeoye, O.O. and Adetola, B.A., 2004. Geoelectrical investigation of the Ondo State Housing Corporation Estate, Ijapo Akure, Southwestern Nigeria. *J. Mining Geol.*, 40(1), 41–48.
- Patra, H.P. and Mallick, K., 1980. *Geosounding Principles: 2. Time-Varying Geoelectric Soundings*. Elsevier, Amsterdam.
- Salem, H. S., 1999. Determination of fluid transmissivity and electric transverse resistance for shallow aquifers and deep reservoirs from surface and well-log electric measurements. *Hydrology and Earth System Sciences*, 3(3), 421–427. <https://doi.org/10.5194/hess-3-421-1999>
- Singh, U.K., Das, R.K. and Hodlur, G.K., 2004. Significance of Dar-Zarrouk parameters in the exploration of quality-affected coastal aquifer systems. *J. Environ. Geol.*, 45, 696–702.
- Sri Niwas and Olivar, A.L. de Lima, 2003. Aquifer parameter estimation from surface resistivity data. *Groundwater*, 41(1), 94–99.
- Thevoz, C., Ousseini, I. and Bergeoin, J.P., 1994. Aspects geomorphologiques de la vallée du Niger au sud de Niamey (secteur Saga Gourma - Gorou Kirey). *Rev. Géographie Alpine*, 1, 65–83.
- Van Nostrand, R.E. and Cook, K.L., 1960. *Interpretation of Resistivity Data*. USGS Professional Paper 499, Washington. <https://doi.org/10.3133/pp499>.
- Vouillamoz, J.M., Favreau, G., Massuel, S., Boucher, M., Nazoumou, Y. and Legchenko, A., 2007. Contribution of magnetic resonance sounding to aquifer characterization and recharge estimate in semiarid Niger. *J. Appl. Geophys.*, 64(3–4), 99–108.
- Ward, S.H. 1990. Resistivity and Induced Polarization Methods in Geotechnical and Environmental Geophysics. *Society of Exploration Geophysicists*, Tulsa, 147-189.
- Zohdy, A.A.R., 1974. Use of Dar Zarrouk curves in the interpretation of vertical electrical sounding data—new techniques in direct-current resistivity exploration. *Geol. Surv. Bull.*, 1313-D.
- Zohdy, A.A.R., Eaton, G.P. and Mabey, D.R., 1974. *Application of Surface Geophysics to Groundwater Investigation*, 2nd ed. United States Geological Survey, Reston, USA. <https://doi.org/10.3133/twri02D1>.

Received on: 16-06-2025; Revised on: 14-08-2025; Accepted on: 16-08-2025

Geomorphic study of the Late Quaternary-Holocene piedmont fans and fluvial terraces of Kota Dun, Kumaun Himalaya

Jonti Gogoi^{1,2,3}, Prabha Pandey^{1,2}, Anand K. Pandey^{1,2*} and Devender Kumar^{1,2}

¹CSIR-National Geophysical Research Institute, Uppal Road, Hyderabad- 500 007, India

²Academy of Scientific and Innovative Research (AcSIR) Ghaziabad- 201002, India

³RMIT University, 124 La Trobe St, Melbourne, Victoria 3000, Australia

* Corresponding Author: akpandey.ngri@csir.res.in

ABSTRACT

The Kota-Pawalgarh Dun is a Half-Dun structure shaped by spatial variation in active deformation partitioning within the Main Boundary Thrust (MBT)-Himalayan Frontal Thrust (HFT) wedge in the Central Kumaun Himalayan front. The post-Siwalik Piedmont fans consist of Dun gravels and provide a geomorphic and stratigraphic constraint on the deformation partitioning on the Dun. Though the fans were mapped, the lack of ages failed to constrain the definition of their stratigraphic and structural significance in the Late Quaternary evolution of the Dun. We present the new mapping results using field and remote sensing data with chronological constraints from the Optically Stimulated Luminescence (OSL) dating of river terraces and alluvial fans across the Dun valley. These new OSL ages of the fan and terrace sediments, in addition to published dates, reveal multiple phases of fan aggradation since > 90 ka until ~19 ka and incision during the Holocene with differential uplift, fan truncation, and fluvial reorganization, driven by ongoing tectonic activity. These findings offer valuable insight into the neotectonic development of the Kota Dun valley and contribute to a better understanding of the deformation processes in the mountain front in the Himalaya Central Seismic Gap region.

Keywords: Geomorphic features, Fluvial terraces, Alluvial fan, OSL dating, Kumaun Himalaya.

INTRODUCTION

The Himalayan region evolved as a consequence of the collision and convergence of the Indian plate underneath the Eurasian plate at a rate of ~50 mm/yr since the Eocene (Molnar and Tapponnier, 1975). The continued convergence produced a series of south-propagating thrusts; namely, the Main Central Thrust (MCT), Main Boundary Thrust (MBT), and Himalayan Frontal Thrust (HFT), originating from the Main Himalayan Thrust (MHT), with younger thrusts initiating towards south (Valdiya, 1992). During the Quaternary period, while the MBT experienced segmental reactivation (Valdiya, 1992; Mugnier et al., 1994), the HFT remained the primary active fault, producing surface ruptures and shaping the topography of the Sub Himalayan Mountain front (Nakata, 1972; Karunakaran and Ranga Rao, 1979; Valdiya, 1992; Yeats et al., 1992; Bollinger et al., 2014). The Sub Himalaya, bounded by the MBT and HFT, comprises deformed foreland basin sediments and features piggyback basins filled with the Piedmont gravel, called Duns (Nakata, 1972; Valdiya, 1992; Thakur et al., 2007). These Duns, namely Soan-Pinjore Duns in Punjab, Haryana and Himachal Pradesh, Dehra Dun and Kota Dun in Uttarakhand, and the Rapti-Dang Duns in Nepal, have varied dimensions and are filled with post-Siwalik debris and fluvial deposits called Dun Gravels (Figure 1a). The Kota Dun is unique as a Half Dun, featuring asymmetric lateral boundaries and a southward step-over by the HFT, making the southward migration of the deformation front towards east; has undergone active deformation during the Late Pleistocene (Nakata, 1972; Valdiya, 1992; Goswami and Pant, 2007; Figure 1b). The changing width of the MBT-HFT wedge, is reflected in the form of lateral variation in geology, structures, landscape pattern and topography in the Kota Dun area. It is situated in the Central Seismic Gap region of Himalaya, where

some major events of the 20th century, such as the 1905 Kangra and 1934 Bihar–Nepal earthquakes, did not produce surface rupture, but are manifested in folds or subtle surface deformation (Yeats and Lillie, 1991). This has emphasized the importance of temporal investigations to uncover the long-term history of surface deformation due to the recurring earthquakes in tectonically active regions (Yeats et al., 1992).

Previous studies in the Kota Dun have provided a broad understanding of the geomorphic setup and evidences of active tectonics (Nakata, 1972; Kumar et al., 2006; Goswami and Pant, 2007; Jayangondaperumal et al., 2013, 2017; Luirei et al., 2015; Rajendran et al., 2015, 2018; Malik et al., 2017; Figure 1). Following the preliminary geomorphic and tectonic setup of the region, which includes the geomorphic and structural expressions of HFT, MBT, and intra-wedge faults (Nakata, 1972; Valdiya, 1992; Joshi and Singh, 2006), Goswami and Pant (2007, 2008) and Luirei et al. (2015) mapped the river terraces, alluvial fan surfaces, wind gaps, and drainage diversions of the Dabka and Baur rivers. The paleoseismic signatures of past surface rupture earthquakes along the HFT during past millennia are explored by the trenching experiments with temporal constraints from the radiocarbon dates of the detrital charcoal samples in the colluvial wedges (Kumar et al., 2006; Malik et al., 2014; Rajendran et al., 2015, 2018; Jayangondaperumal et al., 2017; Malik et al., 2017). Further, the radiocarbon dates from terrace sediments near Ramnagar also provided evidence of fluvial incision along the Kosi River during 4985±25 yrs - 6630±25 yrs (Kumar et al., 2006). The broad geomorphic features, such as terraces and piedmont fans, and geological setup are mapped, but due to the lack of age constraints, it is challenging to build an evolutionary history of the Kota Dun.

This study attempts to improve on the temporal constraints on the lateral variation in active deformation and incision, to enhance our understanding of the Late Quaternary evolution of the Kota Dun. High-resolution 12.5 m resolution Advanced Land Observing Satellite Digital Elevation Model (ALOS-DEM) and 30 m resolution Shuttle Radar Topography Mission Digital Elevation Model (SRTM-DEM) data were processed in Geographic Information System (GIS) software along with Google Earth satellite imageries, to map the deformed and displaced fluvial and alluvial fan surfaces in the Kota Dun region. Extensive field mapping was conducted to validate satellite observations and collect geomorphic data and sediment samples for dating. This will help in understanding the structural and active tectonic control in the evolution of the

Half Dun structure and comparing the similar coeval deformations in the adjoining Duns in the Sub Himalayan Mountain front (Figure 1b).

GEOLOGICAL AND GEOMORPHIC SETUP

The Kota-Pawalgarh Dun, located in the Central Seismic Gap of the Himalaya within the Kumaun region (Figure 1), extends in NW-SE direction along the Himalayan strike and is bounded by the Kosi River (west) and Baur River (east). The Kota Dun extends for approximately 62×33 km on the eastern flank of the Corbett National Tiger Reserve. The Dun valley is drained by the Kosi River and several smaller piedmont rivers, namely Khichari, Dabka, and Baur rivers (Figure 2).

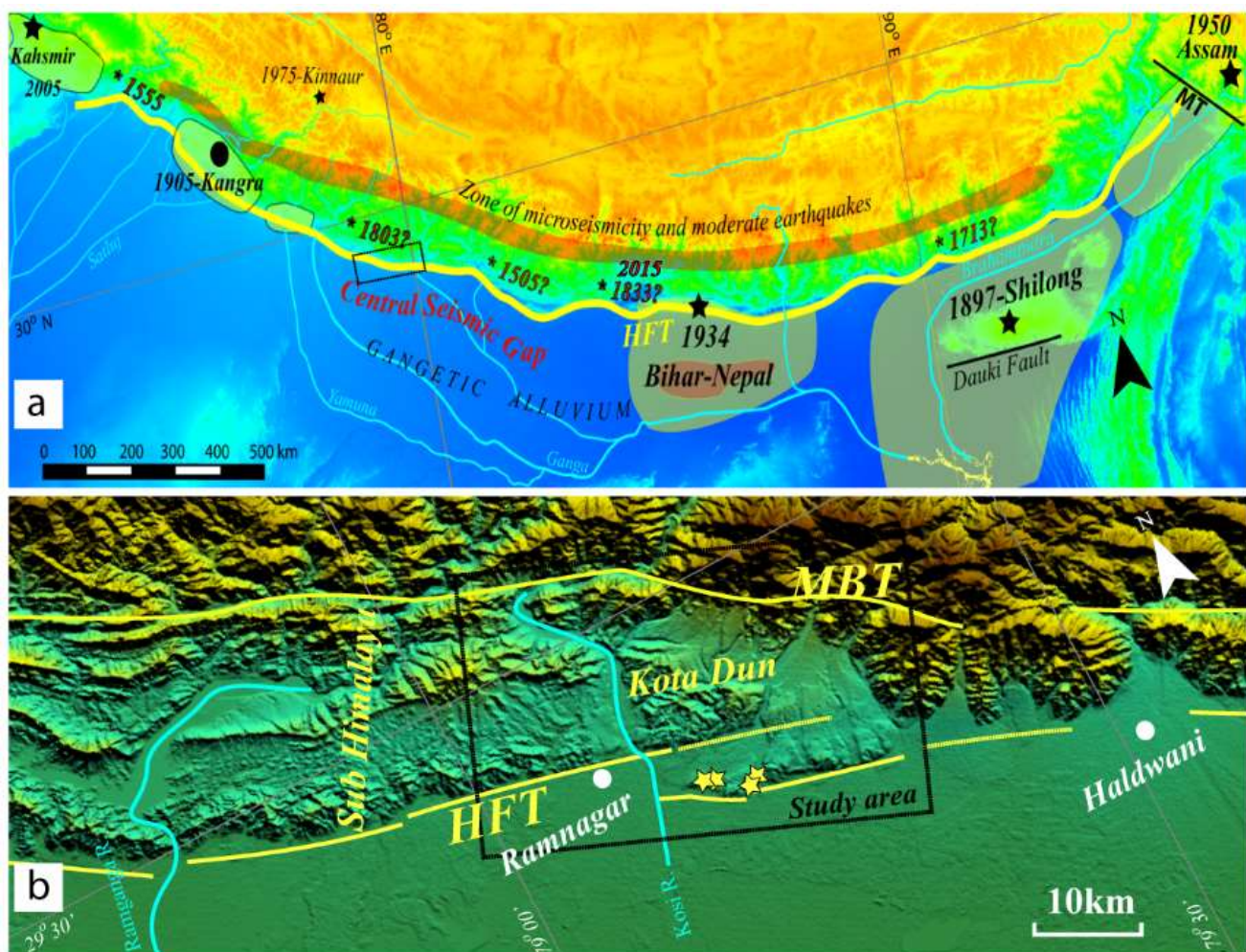


Figure 1. (a) Map of the Himalaya tectonic domains showing the rupture zones of major historical earthquakes. The Black box highlights the study area within the Central Seismic Gap. (b) The blowup topography of the Kota Dun in the Kumaon Himalaya, drained by the Kosi River and other piedmont channels within the MBT-HFT wedge.

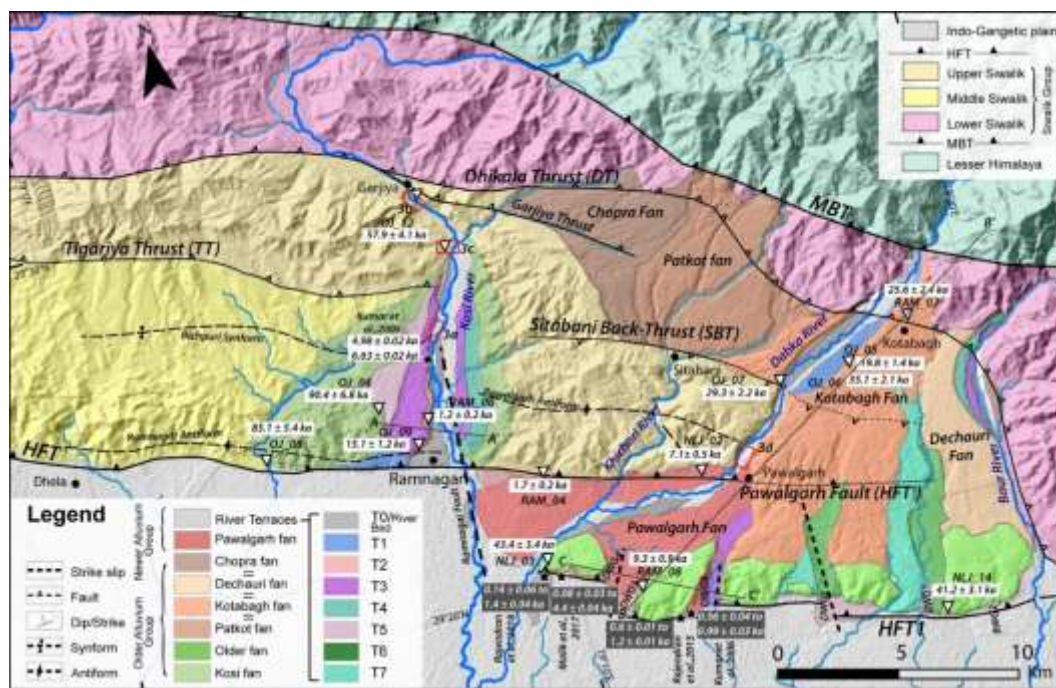


Figure 2. Modified map of Kota-Pawalgarh Dun in the Kumaun Himalaya. White inverted triangles indicate current OSL sampling sites; black stars denote ages from previous studies (white labels for terrace ages, black labels for ages from trenches). Red boxes mark locations of the field photographs. A-A', B-B' and C-C' are the location of the profiles as discussed in Fig. 5.

The study area exhibits a distinctive geological framework, with the Pre-Tertiary Lesser Himalayan sequence tectonically separated from the younger Tertiary-Quaternary formations of the Sub Himalaya across the MBT. The Sub Himalayan foreland sediment of the Siwalik Super Group was deposited during the Middle Miocene to the Pleistocene. The exposed Siwalik succession in the study area is broadly classified into Lower, Middle, and Upper Siwaliks with increasing order of superposition. The Lower Siwalik Formation consists of medium- to coarse-grained sandstone, interbedded with mudstone or shale of Mid to Late Miocene ages, which is exposed in the footwall of the MBT and is thrust onto the Mid-late Pleistocene Upper Siwalik Conglomerate Formation along the out-of-sequence Dikala Thrust (DT) (Figure 2). The Upper Siwalik sequence is thrust onto the Late Miocene Middle Siwalik sandstone and mudstone in the hanging wall of the Tigariya Thrust (TT) to the west of the Kosi River. However, the Upper Siwalik forms the HFT-bound Himalayan front east of the Kosi, which flows along the Kosi Tear Fault/Ramnagar Fault.

The Siwalik sequences are unconformably overlain by piedmont fan deposits of polymictic conglomerate, soft sandstone, and mudstone, which are defined as Dun gravels. These Piedmont Dun gravels have often been mistaken for the Upper Siwalik Boulder Conglomerate due to vaguely similar lithology, but careful observation clearly distinguishes them. The Dun gravel consists of alternate mudstone and matrix-to clast-supported gravels, which are poorly sorted and

subrounded to subangular polymictic clasts derived mainly from the Siwalik and Lesser Himalaya. The Upper Siwalik Boulder Conglomerate consists of well-sorted and rounded clasts primarily derived from the Lesser Himalayan Quartzites and Higher Himalayan crystallines alternating with indurated sandstones. Further, the sediments of Dun gravels are derived from the piedmont catchments, and bed load is controlled by the fluvial discharge, which helped the growth and evolution of the landform.

The gravel sediments are regulated by two major fan systems, namely, the coeval Kotabagh-Chopra-Patkot-Dechauri fans in the Kota-Pawalgarh Dun towards the east and the Kosi Fan along the Kosi River in the west of the study area (Figure 2). Previous studies have mapped and named the coeval fans in the Kota-Pawalgarh Dun (Goswami and Pant, 2007) but have limited information about the Kosi Fan, which is often referred to as the Upper Siwalik sequence (Kumar et al., 2006; Rajendran et al., 2015; Luirei et al., 2015). The gravel deposits in the Kosi Fan along the Kosi River show characteristics of poorly sorted sub-rounded to sub-angular granules and pebbles within the fine-grained matrix alternating with fine sandstone and mudstone (Figures 3a, b, c). These gravel beds dip gently northward and are cemented by calcareous cement near Garjiya (Figures 3a, b), unlike the expected southward-dipping beds in a piedmont fan deposit. These gently northward-dipping gravel beds are incised by the Kosi River with development of 4-5 levels of strath and fill terraces (Figures 2; 3a, b). Unlike the Kosi Fan, the Kotabagh-Chopra-Patkot-Dechauri fans have

older Kota Dun with the piedmont drainage originating from the Lesser Himalayan ranges, and the younger Pawalgarh Dun lies within two HFT strands in the frontal belt (Figure 2). The Dun Gravel in the Kota Dun consists of oxidized, compacted gravel with a sandy-silty matrix that originated from coalescing alluvial fans (Dechauri fan, Kotabagh fan, Patkot fan, Chopra fan) from the Lesser Himalaya and deposited over the Siwalik formations. The sorting and roundness of the clasts in the gravels increase southward (Figures 3d, e). They are considered equivalent to the Varanasi Older Alluvium of Late Pleistocene age (Valdiya, 1992). The Chopra-, Patkot- and part of Kotabagh fans abut against the Sitabani Back Thrust (SBT), whereas the latter grow to the mountain front in the HFT zone. The Kotabagh Fan is dissected by the SBT as well as the Pawalgarh Thrust (HFT'), suggesting that the tectonic activity continued even after the fan deposition. In the frontal HFT belt, the Kotabagh Fan overlies the Older Fan, which occurs as isolated patches along the HFT zone (Figure 2). The HFT zone is dissected by a series of wind gaps of the Dabka River with decreasing elevations towards the west, suggesting progressive westward deflection of the river (Malik et al., 2014; Luirei et al., 2015). The deflected Dabka River deposits bedload between the HFT' and HFT1 as the Pawalgarh Fan (Figure 2).

The Kota Dun and adjoining areas are drained by the Kosi, Dabka, and Baur rivers, from west to east, respectively. Between the Kosi and Dabka rivers, the HFT is marked by a ~3 m high, NW–SE trending scarp, and Kichari and Dabka rivers have incised the Upper Siwalik rocks and piedmont sediments

(Luirei et al., 2015). Near Ramnagar, a south verging anticline (Ramnagar antiform) with a steep $\sim 70^\circ$ dip in the south forelimb and a synform (Bichpuri synform) near the Bichpuri range, characterizes the landscape morphology along the west bank of Kosi Fan. On the eastern side, the HFT splits into two strands, HFT' and HFT1 (Figure 2), and the streams and topography are wedged by the Pawalgarh antiform with a southern dip of $\sim 35^\circ$ and a gentle northern dip of $\sim 10^\circ$. Along the Kosi River, five levels of unpaired terraces are observed. The Kosi river bed (T_0) is at an elevation of 373 m a.s.l., T_1 , T_2 , T_3 , and T_5 on the right bank are at a height 9 m, 20 m, 26 m, and 86 m high above river bed, respectively; whereas the left bank preserves T_1 , T_3 , and T_4 terraces at 4 m, 29 m, and 45 m above river bed (Figure 2). The T_1 , T_2 , and T_3 have a narrow lateral growth, suggesting high incision, while T_4 and T_5 have wide lateral growth (Figure 2). The Dabka River with various Wind Gaps (DWG) preserves seven levels of terraces, viz. T_5 , T_6 , and T_7 are mapped along the DWG1; DWG2 has three terrace levels and one each at DWG3 and DWG4 (Malik et al. 2017). Dabka River bed (T_0) is at an elevation of 357 m a.s.l. and T_1 , T_2 , and T_3 are at the height of 6 m, 62 m, and 71 m above the river bed. The terraces along DWGs mostly overlap or lie at the same level as the Pawalgarh Fan sediments. The eastern Baur River shows asymmetrical uplift, with sediment fill over Lower Siwalik mudstones and sandstones on the left bank and Upper Siwalik conglomerates on the right, where five terrace levels are present in contrast to two levels in the left bank (Goswami and Pant, 2007).



Figure 3. (a,b) North-tilted gravel deposit/ Kosi Fan material overlain by terrace sediments along the Kosi River. (c) Kosi Fan sediments near Dhikuli along the left bank of the Kosi River, OSL samples marked with inverted triangles. (d) Fan deposit along the Dabka River (e) Zoomed-in view of clast and matrix from the Dabka River section, showing sub-rounded to sub-angular granules.

OPTICALLY STIMULATED LUMINESCENCE (OSL) DATING

Sediment samples were collected from the terraces and fan surfaces in opaque, light-proof aluminium/PVC tubes to prevent sunlight exposure prior to OSL dating (Aitken, 1998). In the lab under subdued red light conditions, fourteen samples were sieved to isolate the desired grain size (90-150 μm for OJ and NLJ samples; 150-250 μm for RAM samples). The sieved material was then chemically treated sequentially with HCl, H_2O_2 , and HF to remove carbonates, organic matter, and feldspars, respectively, to get quartz grain concentrates. Equivalent dose (ED) measurements on quartz grains were conducted using the Risø TL/OSL DA-20 reader employing the single-aliquot regenerative (SAR) dose protocol (Murray et al., 2021). Uranium (U), thorium (Th), and potassium (K) concentrations were measured using WD-XRF and gamma counting techniques. Moisture content was determined on samples “as received” from the field to calculate the dose rate. More details of the method can be found in Thomas et al. (2007) and Reddy et al. (2013).

Signals from Quartz OSL and K-Feldspar Infrared Stimulated Luminescence (IRSL) show < 5% feldspar content

during quartz purity test, indicating that the sample contains datable quartz signal (Figure 4 a, b). Preheat plateau tests were conducted at temperatures ranging from 160 °C to 280 °C in 20 °C increments, for 10 seconds each. For each temperature, three aliquots were analyzed, and the mean values were calculated individually for each condition (Figure 4c). For our analysis, the plateau temperature is attained at 220 °C, which we have used for the preheat step in the SAR protocol. This is consistent with the commonly used preheat temperature by other workers in the Himalayan region (De Sarkar et al., 2013; Srivastava et al., 2013). The LDAC (version 1.0) platform was used to determine ages (Liang and Forman, 2019) for all the samples except the RAM series, for which we used the DRAC Program (Durcan et al., 2015). For the determination of the ED of the samples, we used a recycling ratio of 10% and a recuperation ratio of 5%. Bailey and Arnold (2006) recommended using the Central Age Model (CAM) for ED values with low (< 40%) overdispersion (OD) and the Minimum Age Model (MAM) for EDs with high (> 40%) overdispersion. Since all our ED values exhibit low dispersion (< 40%), we applied the CAM for age estimations in this study. The OSL ages of samples from different stratigraphic horizons are summarized in Table 1.

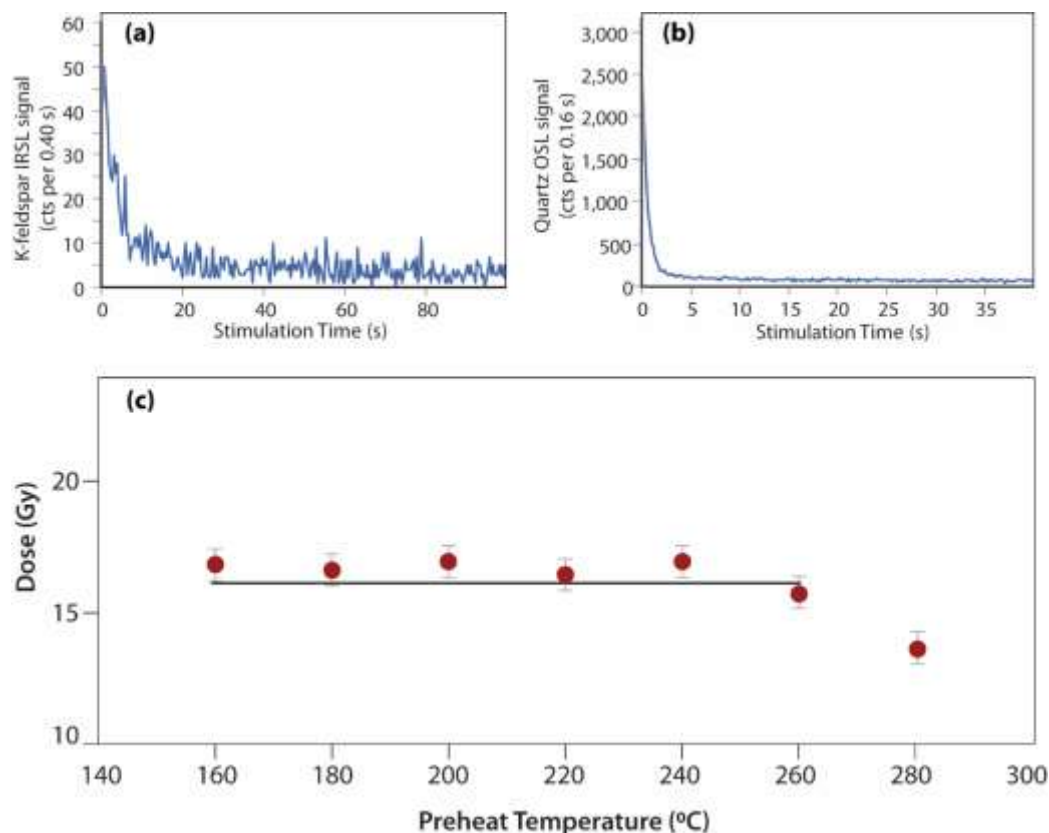


Figure 4. Typical natural OSL decay curve for sample OJ_12 (a) K-feldspar (IRSL) (b) quartz (c) A representative Preheat plateau test for sample OJ_13 at the different preheat temperatures.

Table 1. OSL ages of the alluvial and fluvial sediments

Sl. No.	Feature	Sample code	No of aliquots (N)	Equivalent Dose (Gy)	Dose Rate (Gy/ka)	Depth below ground surface (m)	Water content (%)	K (%)	U (ppm)	Th (ppm)	OD (%)	Age (ka)
1	T1	RAM_06	10	3.6782	3.298	1.2	0.68	1.65	2.7	12.11	34	1.2±0.2
2	T2	RAM_08	12	38.3296	4.238	10.0	3.15	2.5	3.4	14.7	20.6	9.3±0.9
3	T3	OJ_09	18	26.4600	1.747	1.3	1.802	1.615	0.112	0.12	19.7	15.1±1.2
4	Pawalgarh Fan	RAM_04	14	5.1092	3.033	2.0	1.24	1.49	2.2	12.7	28	1.7±0.2
5		NLJ_02	18	25.4405	3.592	1.2	1.329	3.155	0.989	1.349	20.4	7.1±0.5
6	Kotabagh Fan	OJ_05	16	83.7760	3.592	1.9	5.742	3.197	2.217	11.36	34.1	19.8±1.4
7		RAM_07	13	110.2188	4.404	3.0	6.02	2.47	3.9	17.0	21.2	25.6±2.4
8		OJ_07	9	91.1540	3.11	1.1	12.711	2.886	1.287	4.332	7.41	29.3±2.2
9		OJ_06	14	131.7050	3.754	4.6	11.760	3.378	0.087	12.79	4.2	35.1±2.1
10	Older Fan	NLJ_14	16	124.9075	3.033	8.0	1.017	2.505	0.556	3.837	13.45	41.2±3.1
11		NLJ_03	10	183.872	4.231	12.0	1.763	2.997	0.231	16.12	14.5	43.4±3.4
12	Kosi Fan	OJ_12	16	108.4175	1.871	1.7	0.666	1.043	0.1	0.12	17.6	57.9±4.1
13		OJ_08	21	152.609	1.792	1.6	0.521	1.329	1.41	0.12	8.5	85.1±5.4
14		OJ_04	12	281.69	3.114	2.0	5.863	2.541	0.897	7.439	14.4	90.4±6.8

T= Terrace

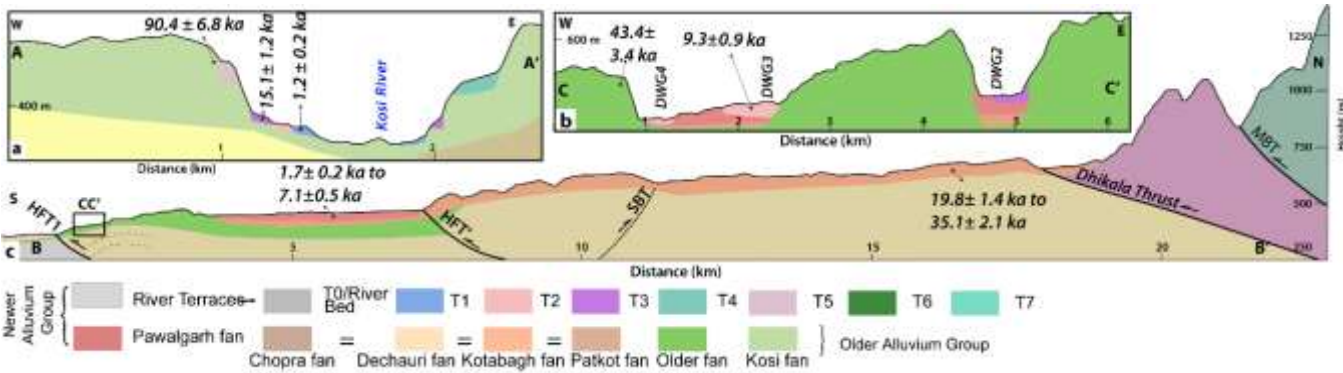


Figure 5. Elevation profiles AA', BB', and CC' (marked in Figure 2) across the study area, highlighting the various fluvial terraces and alluvial fans along with OSL dates (a) at Ramnagar across the Kosi River, (b) at the Dabka River wind gaps, south of the Kota Dun, and (c) across the Kota-Pawalgarh Dun valley.

RESULTS AND DISCUSSION

Three elevation profiles, AA', BB', and CC', representing the stratigraphic and structural relationship of the fans and terraces, are plotted across the study area to highlight the geomorphic variations in the region (Figure 5). The Kosi River has five levels of unpaired fluvial terraces (Figure 5a). The OSL ages along the Kosi River vary from 57.9±4.1 ka to 90.4±6.8 ka for the Kosi Fan sediments. Terraces T₁ and T₃ from the right bank yielded 1.2±0.2 ka and 15.1±1.2 ka OSL ages, respectively, while the T₂ yielded 4.98±0.02 ka and 6.63±0.02 ka radiocarbon ages (Kumar et al., 2006). The unpaired terraces and narrow lateral growth suggest that the river's lack of peneplanation and rapid incision in response to the tectonic activity along the active structures during the wet climatic period. The heights for T₁, T₂, and T₃, terraces of the Kosi River are 9 m, 20 m, and 26 m above the river bed, respectively. Dividing it by their respective ages, the incision rates are estimated to be 7.5±1.2 mm/yr, 3.01±0.01 mm/yr, and

1.72±0.13 mm/yr, respectively. These values suggest higher incision rates during the Holocene when the intensified Indian Summer Monsoon (ISM) activity enhanced the runoff and stream power along the Kosi River. The Oldest Kosi Fan is back-tilted and dips at ~12° due north, suggesting the region is undergoing uplift along the HFT. Considering the age of the highest fan level (90.4±6.8 ka at 87 m above the river bed; Figure 5a), which approximates the riverbed elevation at the time of deposition, the long-term incision rate during the Late Quaternary is estimated to be ~1 mm/yr.

We plotted a geological profile along the Dabka River (BB') through the Kota-Pawalgarh Fan to understand the stratigraphic expressions of different Piedmont aggradation and incision cycle vis-à-vis deformation partitioning within HFT1-DT Thrust wedge (Figures 2, 5c). The Older Fan, occurring as isolated ridges along HFT1 in the south, yielded 43.5±3.4 ka and 41.2±3.1 ka OSL ages (Figures 2, 5c; Table 1). The Kotabagh Fan yielded 35.1±2.1 ka, 29.3±2.2 ka,

25.0 \pm 2.7 ka, and 19.8 \pm 1.4 ka ages with increasing order of superposition along the Dabka section (Figures 2, 5c; Table 1). Progressive aggradation within the Dun valley is clearly observed until ~19 ka, the youngest age in the Kotabagh Fan (Figure 2, Table 1). The ages for the Pawalgarh Fan are estimated as 7.1 \pm 0.5 ka at Pawalgarh and 1.7 \pm 0.2 ka near Kiari Kham (Figures 2, 5c; Table 1). To understand the Dabka River deflection and associated landform growth, we plotted a profile through the Older Fan ridges parallel to HFT1 in the hanging wall (Figures 2, 5b). The Dabka Wind Gaps (DWG2, DWG3, DWG4) along this transect expose the abandoned exit points of the Dabka River, which formed the Kota-Pawalgarh Fan, and the terraces preserve incision history. OSL age for T₂ at DWG3 is recorded to be 9.3 \pm 0.9 ka (Figure 5b; Table 1).

The incision rates for both the Kosi Fan and the Kotabagh Fan are almost similar, although the Kosi Fan's growth predates that of the Kota Dun valley fans. The Youngest gravel of the Kosi fan yielded an age of 57.9 \pm 4.1 ka, and it lies adjacent to the cemented gravel deposits of the Kosi Fan at Garjia (Figures 3b, c). It indicates that the cementation occurred during a cool, wet period that facilitated chemical weathering; specifically, the dissolution of calcite, which subsequently cemented the existing rocks within available pore space and fractures, as observed in the Dehra Dun valley (Pandey et al., 2014). The Older Fan deposits in the Kota Dun date 41.2 \pm 3.1 ka, over which the Kotabagh and other coeval fans continued aggradation during 35.1 \pm 2.1 ka-19.8 \pm 1.4 ka (Figures 2, 5c, Table 1). The sedimentation in the western part of the Kota Dun was perturbed by the topographic barrier created by the uplift of the Upper Siwalik rocks in the form of the Pawalgarh anticline bounded by the HFT and SBT as a pop-up structure (Figures 2, 5c). The tectonic deformation along the HFT-SBT did not propagate eastward with the same intensity as evidenced by the growth of the Kota Dun fan, which records continuous aggradation upto 19.8 \pm 1.4 ka near the HFT1 zone. Though the reduced vigor of the HFT' (=Pawalgarh Thrust), SBT eastward caused back-tilting and drainage disruption in the Kotabagh fan, causing westward migration of the Dabka River after ~19 ka. The progressive westwards deflections are preserved in the DWGs 1-4 (Figures 2, 5b). The terrace sediments in the DWG3 yielded an OSL age of 9.3 \pm 0.9 ka, suggesting at least two major episodes of drainage deflection during DWG1 and DWG2 between 19.8 \pm 1.4 ka and 9.3 \pm 0.9 ka due to the uplift of the frontal belt consisting of the older fan and Kotabagh fan along the HFT1 (Figures 2, 5c). The river Dabka shifted its course from DWG3 to DWG4 between 9.3 \pm 0.9 ka to 7.1 \pm 0.5 ka. Later dates from the Pawalgarh Fan indicate that channel aggradation started within the HFT1-HFT' wedge, with deposition continuing through 1.7 \pm 0.2 ka and into the present. Considering the elevations of the dated fan (63 m above the river bed) and T₂ terrace (62 m above the river bed) within the DWG3 sediments, the Older Fan is estimated

to be incising at a rate of 1.45 \pm 0.11 mm/yr, while the terrace incision rate in the HFT1 zone is significantly higher at 6.6 \pm 0.6 mm/yr. The incision rate of 1.86 \pm 0.13 mm/yr near HFT' at Pawalgarh (14 m above the river bed), suggests the deformation front shifted to HFT1 and is responsible for the lack of topography growth comparable to the HFT-SBT wedge. These incision rates are similar to those observed in the Kosi fan and terraces along the Kosi River. The incision rates of 6.6 \pm 0.6 mm/yr at Dabka and 7.5 \pm 1.2 mm/yr in the HFT zone resemble well with previous uplift/incision rates of 5-6 mm/yr at Ramnagar (present study area) along the Kosi river (Kumar et al., 2006), 6.9 \pm 1.1 mm/yr in the DehraDun (Wesnousky, 1999); ~4 mm/yr at Kala Amb and ~4-6 mm/yr at Chandigarh, further west (Kumar et al., 2006).

Importantly, in the present study, two distinct systems of structural evolution have been observed: one associated with the Kosi fan and its terraces, and the other linked to the structurally complex Kotabagh and other fans within the Kota Dun area. Along the Kosi River, the fluvial discharge and active tectonic structures associated with the HFT control the spatial variation in erosion-aggradation and bedrock uplift. Contrastingly, within the Kota Dun, the fans are perturbed by the obstruction due to intra-wedge deformation and growth of structural hills and valleys, such as the Pawalgarh anticline and Pawalgarh fan, located between HFT' and HFT1 trough (Figures 2, 5). The phases of piedmont gravel aggradation and fan growth in Kota Dun are similar to and coeval with those observed in the neighboring Dehra Dun (41-11.5 ka) (Thakur et al., 2007). This synchronicity suggests coeval tectonic activity and landform growth and evolution of the Himalayan Front in both the Kumaun and NW Himalaya regions. It is also important to highlight that, despite previous studies using geomorphic and stratigraphic classifications and structure-bound landscape analysis (Nakata, 1972; Valdiya, 1992; Kumar et al., 2006; Goswami and Pant, 2007; Jayangondaperumal et al., 2013, 2017; Luirei et al., 2015; Rajendran et al., 2015, 2018; Malik et al., 2017), the lack of temporal constraint failed to comprehensively characterize the Late Quaternary tectonogeomorphic evolution of the Kota Dun. The present work highlights the lateral variations in sediment aggradation, landform growth, and deformation partitioning in two distinct fan systems of Kota Dun in the Kumaun Himalaya, highlighting their similarity with the other Duns along the Sub Himalayan mountain front.

CONCLUSIONS

The growth of new faults causes lateral variation in the active deformation front and controls the landscape evolution along the Sub Himalayan mountain front. The Kota Dun in Kumaun Himalaya provides a unique opportunity to explore growth of a half-Dun through its distinctive geomorphic, stratigraphic, and structural expressions supported by robust temporal

constraints. The southward fan progradation, truncation of geomorphic surfaces by fold-fault growth, and unpaired terraces, constrain the lateral variations in active deformation and incision during Late Quaternary. The study reveals multiple phases of piedmont fan aggradation and fluvial incision, controlled by climatic variations and tectonic activity, especially along the HFT and intra-wedge deformation, including backthrusting. Some important findings are given below.

- (i) The lateral variations in structural growth, such as the Pawalgarh Anticline pop-up structure between HFT-SBT, and growth of HFT1 as a stepover, resulting into the HFT' (= Pawalgarh Thrust), without a significant deformation locus, have influenced the Late Quaternary landscape evolution, including fan geometry and drainage deflection in the Kota Dun.
- (ii) The study highlights that lateral variations in sedimentation and uplift patterns between the Kosi and Kota fan systems are controlled by the deformation partitioning, which is more pronounced in the structurally complex Kota Dun due to intra-wedge deformation.
- (iii) OSL dating provides a well-constrained temporal framework for the formation of fans and terraces. Aggradation of the Kosi Fan began prior to 90.4 ka and continued until ~57.9 ka; while the Kotabagh and Pawalgarh Fans, span from ~43.4 ka to ~1.7 ka.
- (iv) The estimated incision rates range from ~1.4 to 1.0 mm/yr based on fan incision data, while the terraces derived rates during the Holocene period are distinctly higher, between 7.5 and 6.6 mm/yr. The elevated Holocene incision rate is similar to that observed across the HFT zone in the NW Himalaya. This pronounced incision is attributed to the intensification of the Indian Summer Monsoon in the Holocene.
- (v) The geomorphic and tectonic evolution patterns observed in Kota Dun closely resemble those of adjacent Duns such as Dehra Dun, indicating regionally synchronous tectono-geomorphic development across the NW Sub-Himalaya during the Late Quaternary.
- (vi) Unlike previous studies that primarily relied on geomorphic classification and landscape evolution, the present study integrates robust chronological data with detailed structural and geomorphic analyses, providing a comprehensive understanding of Late Quaternary landscape evolution in Kota Dun.

Acknowledgement

The authors highly appreciate the three anonymous reviewers for constructive comments and valuable suggestions that improved the quality of data presentation and interpretation. We highly appreciate Dr. O. P. Pandey, Editor, for his apt

handling and constructive suggestions to improve the manuscript. The authors thank the Director of CSIR-NGRI for his support and permission to publish this work (NGRI/Lib/2025/ Pub-87). The authors thank the Forest Department and the Government of Uttarakhand for allowing us to work within the Corbett Tiger Reserve in Kota-Pawalgarh Dun. JG acknowledges the financial support from CSIR-NGRI and DST Inspire research fellowship to pursue a PhD. AKP, PP and DK thankfully acknowledge the financial support from CSIR project no. MLP-0001-28-FBR-0001 (SHIVA) at CSIR-NGRI. Satish C Verma and K. Raghuveer are acknowledged for their help in the OSL dating.

Author Credit Statement

JG: Field work, Investigations, visualization, data acquisition, data curation and writing-original draft; PP: Conceptualization, visualization, data curation, methodology, supervision, writing-review and editing; AKP: Conceptualization, visualization, data curation, funding acquisition, methodology, project administration, supervision, writing-review and editing; DK: Field work, Formal analysis, writing- review and editing.

Data Availability

Data can be made available on reasonable request to the corresponding author.

Compliance with Ethical Standards

The authors declare that they have no conflict of interest and adhere to copyright norms.

References:

- Aitken, M. J., 1998. An introduction to optical dating: the dating of Quaternary sediments by the use photon stimulated Luminescence. Oxford Publications.
- Bailey, R. M. and Arnold, L. J., 2006. Statistical modelling of single grain quartz De distributions and an assessment of procedures for estimating burial dose. *Quat. Sci. Rev.*, 25(19-20), 2475-2502.
- Bollinger, L., Sapkota, S. N., Tapponnier, P., Klinger, Y. R. M., Woerd, J. V. der, Tiwari, D.R., Pandey, R., Bitri, A. and Berc, S. B. de., 2014. Estimating the return times of great Himalayan earthquakes in eastern Nepal: Evidence from the Patu and Bardibas strands of the Main Frontal Thrust. *J. Geophys. Res., Solid Earth*, 119(9), 7123–7163.
- De Sarkar, S., Mathew, G., Pande, K., Chauhan, N. and Singhvi, A. K., 2013. Rapid denudation of Higher Himalaya during late Pliocene, evidence from OSL thermochronology. *Geochronometria*, 40(4), 304-310.
- Durcan, J. A., King, G. E. and Duller, G. A., 2015. DRAC: Dose Rate and Age Calculator for trapped charge dating. *Quat. Geochronology*, 28, 54-61.
- Goswami, P. K. and Pant C. C., 2007. Geomorphology and tectonics of Kota-Pawalgarh Duns, Central Kumaun Sub-Himalaya. *Curr. Sci.*, 92(5), 685–690.
- Goswami, P. K. and Pant, C. C., 2008. Tectonic evolution of Duns in Kumaun Sub-Himalaya, India: A remote sensing and GIS-based study. *Int. J. Remote Sens.*, 29(16), 4721-4734.

- Jayangondaperumal, R., Mugnier J. L. and Dubey, A. K., 2013. Earthquake slip estimation from the scarp geometry of Himalayan Frontal Thrust, western Himalaya: implications for seismic hazard assessment. *Int. J. Earth Sci.*, 102, 1937-1955.
- Jayangondaperumal, R., Daniels, R. L. and Niemi, T. M., 2017. A paleoseismic age model for large-magnitude earthquakes on fault segments of the Himalayan Frontal Thrust in the Central Seismic Gap of northern India. *Quat. Int.*, 462, 130-137.
- Joshi D.D. and Singh R. J., 2006. Active fault studies in the Himalayan Frontal Belt between Kosi and Gaula rivers, Nainital district, Uttarakhand (f. S. 2004-05 and 2005-06). GSI report.
- Karunakaran, C. and Ranga Rao. A., 1979. Status of exploration for hydrocarbon in the Himalayan region: Contribution to stratigraphy and structure. *Geol. Surv. India, Miscellaneous Publ.*, 41 (5), 1-66.
- Kumar, S., Wesnousky, S. G., Rockwell, T. K., Briggs, R. W., Thakur, V. C. and Jayangondaperumal, R., 2006. Paleoseismic evidence of great surface rupture earthquakes along the Indian Himalaya. *J. Geophys. Res., Solid Earth*, 111, B3.
- Liang, P. and Forman, S., 2019. LDAC: Luminescence dose and age calculator (v 1.0) (computer software). Luminescence dating research lab, Baylor University. <https://www.baylor.edu/geosciences/index.php?id=962356>
- Luirei, K., Bhakuni, S. S. and Kothiyari, G. C., 2015. Drainage response to active tectonics and evolution of tectonic geomorphology across the Himalayan Frontal Thrust, Kumaun Himalaya. *Geomorphology*, 239, 58-72.
- Malik, J. N., Shah, A. A., Naik, S. P., Sahoo, S., Okumura, K. and Patra, N. R., 2014. Active fault study along foothill zone of Kumaun Sub-Himalaya: influence on landscape shaping and drainage evolution. *Curr. Sci.*, 229-236.
- Malik, J. N., Naik, S. P., Sahoo, S., Okumura, K. and Mohanty, A., 2017. Paleoseismic evidence of the CE 1505 (?) and CE 1803 earthquakes from the foothill zone of the Kumaon Himalaya along the Himalayan Frontal Thrust (HFT), India. *Tectonophysics*, 714, 133-145.
- Molnar, P. and Tapponnier, P., 1975. Cenozoic Tectonics of Asia: Effects of a Continental Collision: Features of recent continental tectonics in Asia can be interpreted as results of the India-Eurasia collision. *Science*, 189(4201), 419-426.
- Mugnier, J. L., Huyghe, P., Chalaron, E. and Mascle, G., 1994. Recent movements along the Main Boundary Thrust of the Himalayas: normal faulting in an over-critical thrust wedge?. *Tectonophysics*, 238(1-4), 199-215.
- Murray, A., Arnold, L.J., Buylaert, J.P., Guérin, G., Qin, J., Singhvi, A.K., Smedley, R. and Thomsen, K.J., 2021. Optically stimulated luminescence dating using quartz. *Nature Reviews Methods Primers*, 1(1), p.72.
- Nakata, T., 1972. Geomorphic history and crustal movement of the foothills of the Himalayas. *Science Report Tohoku Univ. 7th series (Geography)*, 22, 39-177.
- Pandey, A.K., Pandey, P., Singh, G.D. and Juyal, N., 2014. Climate footprints in the Late Quaternary-Holocene landforms of Dun Valley, NW Himalaya, India. *Curr. Sci.*, 106(2), 245-253.
- Rajendran, C. P., John, B. and Rajendran, K., 2015. Medieval pulse of great earthquakes in the central Himalaya: Viewing past activities on the frontal thrust. *J. Geophys. Res., Solid Earth*, 120(3), 1623-1641.
- Rajendran, C. P., John, B., Anandasabari, K., Sanwal, J., Rajendran, K., Kumar, P. and Chopra, S., 2018. On the paleoseismic evidence of the 1803 earthquake rupture (or lack of it) along the frontal thrust of the Kumaun Himalaya. *Tectonophysics*, 722, 227-234.
- Reddy, D.V., Singaraju, V., Mishra, R., Kumar, D., Thomas, P.J., Rao, K.K. and Singhvi, A.K., 2013. Luminescence chronology of the inland sand dunes from SE India. *Quat. Res.*, 80, 265-273.
- Srivastava, P., Kumar, A., Mishra, A., Meena, N. K., Tripathi, J. K., Sundriyal, Y. P., Agnihotri, R. and Gupta, A. K., 2013. Early Holocene monsoonal fluctuations in the Garhwal higher Himalaya as inferred from multi-proxy data from the Malari paleolake. *Quat. Res.*, 80(3), 447-458.
- Thakur, V.C., Pandey, A.K. and Suresh, N., 2007. Late Quaternary-Holocene evolution of Dun structure and the Himalayan Frontal Fault zone of the Garhwal Sub-Himalaya, NW India. *J. Asian Earth Sci.*, 29(2), 305-319.
- Thomas, P.J., Reddy, D.V., Kumar, D., Nagabhushanam, P., Sukhija, B.S. and Sahoo, R.N., 2007. Optical dating of liquefaction features to constrain prehistoric earthquakes in upper Assam, NE India-some preliminary results. *Quat. Geochronology*, 2, 278-283.
- Valdiya, K.S., 1992. The Main Boundary Thrust zone of the Himalaya, India. *Annales Tectonicae (Special Issue Suppl.)* VI, 54-84.
- Wesnousky, S. G., Kumar, S., Mohindra, R. and Thakur, V. C., 1999. Uplift and convergence along the Himalayan Frontal Thrust of India. *Tectonics*, 18, 967-976.
- Yeats, R.S. and Lillie, R., 1991. Contemporary tectonics of the Himalayan frontal fault system: folds, blind thrusts and the 1905 Kangra earthquake. *J. structural Geol.*, 13 (2), 215-225.
- Yeats, R.S., Nakata, T., Farah, A., Fort, M., Mirza, M.A., Pandey, M.R. and Stein, R.S., 1992. The Himalayan Frontal Fault System. *Annales Tectonicae (Special Issue Suppl.)* VI, 85-98.

Received on: 28-07-2025; Revised on: 05-08-2025; Accepted on: 06-08-2025

Geospatial assessment of groundwater quality and its suitability for drinking and irrigation in semi-arid regions of Andhra Pradesh (India) using water quality index approach

Ravi Kumar Pappaka¹, Srinivasa Gowd Somagouni^{1*}, Krupavathi Chinthala¹, and Pradeep Kumar Badapalli²

¹Dept of Geology, Yogi Vemana University, YSR Kadapa- 516005, Andhra Pradesh (India)

²CSIR-National Geophysical Research Institute, Hyderabad-500007, Telangana (India)

*Corresponding author: ssgowd@gmail.com

ABSTRACT

Groundwater, a vital resource for drinking and irrigation in the semi-arid regions of Andhra Pradesh, is increasingly threatened by rapid depletion and quality deterioration due to growing demands from intensive agriculture and population expansion. In this study, a total of 92 groundwater samples were collected from boreholes during the pre-monsoon (PRM) and post-monsoon (POM) seasons, and their physicochemical properties were systematically analyzed. The major ion sequence in the groundwater was found to be $\text{Na}^+ > \text{Ca}^{2+} > \text{Mg}^{2+} > \text{K}^+$ for cations, and $\text{HCO}_3^- > \text{Cl}^- > \text{SO}_4^{2-} > \text{NO}_3^- > \text{F}^-$ for anions. During the PRM season, only 19% of the samples met drinking water standards, with Water Quality Index (WQI) values ranging from 59.18 to 172.21. In the POM season, 22% of the samples were deemed safe for drinking, with WQI values ranging from 70.07 to 229.46. The majority of the samples were unsafe due to contamination from human activities, including improper sewage disposal and agricultural runoff. To assess the suitability of groundwater for agricultural and domestic use, Gibbs, USSL, and Wilcox diagrams were utilized. The Gibbs plot indicated that rock dominance governs the groundwater chemistry in the region. Most samples were highly suitable for irrigation, as evidenced by favorable Sodium Adsorption Ratio (SAR), %Na, Soluble Sodium Percentage (SSP), Kelly's Ratio (KR), Residual Sodium Carbonate (RSC), and Permeability Index (PI) values. The Piper diagram revealed a prevalence of $\text{Ca}^{2+}\text{-HCO}_3^-$ and $\text{Ca}^{2+}\text{-Mg}^{2+}\text{-Cl}^-$ water types. Using Geographic Information System (GIS) techniques, the spatial distribution of groundwater quality was mapped, showing that the majority of samples failed to meet drinking water quality standards, thus necessitating treatment before consumption. Groundwater with elevated concentrations of fluoride and nitrate is unsuitable for drinking purposes and should be avoided. The findings underscore the urgent need for sustainable aquifer management strategies to ensure the continued availability of safe groundwater for both domestic and agricultural use.

Keywords: Hydrogeochemistry, Water Quality Index (WQI), Drinking water and irrigation, Remote sensing and GIS, Spatial distribution maps, Semi-arid region, Pandameru River Basin

INTRODUCTION

Water is an essential resource that sustains life across ecosystems, supporting both plant and animal life. However, the quality of groundwater, an important source for drinking and irrigation, is deteriorating due to a combination of natural processes and anthropogenic activities. Factors such as rising temperatures, industrial discharge, and intensified agricultural practices are exacerbating water quality degradation, posing significant health risks to both aquatic and terrestrial ecosystems (Badapalli et al., 2024). These concerns highlight the need for comprehensive groundwater quality monitoring to protect ecological integrity and anticipate future environmental changes (Khatri et al., 2020; Parveen et al., 2025).

The purity of groundwater is influenced by both geogenic and anthropogenic factors. With increasing industrialization and the expansion of modern agricultural practices, untreated waste and surface runoff often enter the groundwater system, disrupting ecological balance (Gugulothu et al., 2022; Molagamudi et al., 2023). Groundwater quality is governed by multiple factors, including the chemical composition of surrounding rocks and soils, seasonal rainfall patterns, aquifer dynamics, and human activities such as the improper disposal of waste into poorly constructed wells. As groundwater percolates through weathered rock layers, its chemistry is altered by regional geology, flow patterns, and mineral interactions, all of which collectively shape its quality.

Understanding hydrogeochemical processes is essential for identifying and managing contamination sources in groundwater. Small amounts of metal ions are essential for health, yet excess exposure can be toxic or even carcinogenic. The rise of newly developed chemicals further threatens water resources, underscoring the urgent need to mitigate these contaminants (Asadi et al., 2019; Anusha et al., 2022). Innovative solutions, such as the use of nano-adsorbents, are under investigation to remove pollutants; however, local geochemical processes play a substantial role in defining groundwater chemistry and require careful analysis.

In India, the quality of groundwater, especially in hard rock terrains like Anantapur, Andhra Pradesh, is declining due to population growth, intensive groundwater extraction, and excessive fertilizer use. Numerous studies have analyzed the impact of human activities such as wastewater discharge, agricultural chemicals, and water-rock interactions on groundwater, highlighting the need for strategies to improve groundwater suitability for drinking, agricultural, and industrial use (Subba Rao et al., 2019; Nayak et al., 2023). In the semi-arid Pandameru River basin, Andhra Pradesh, groundwater accounts for 80-90% of water needs, necessitating immediate action to safeguard this essential resource (Pappaka et al., 2024).

Water Quality Index (WQI) is a widely recognized tool for assessing groundwater suitability. Unlike traditional evaluation

methods that may lack a comprehensive view of spatial and temporal water quality trends, the WQI provides a single metric representing overall water quality, making it an effective resource for policymakers (Dutta et al., 2022; Golla and Badapalli, 2022). This study underscores the significance of WQI as a reliable method for assessing groundwater quality for drinking, agricultural, and hydrochemical purposes in semi-arid regions of Andhra Pradesh, India.

This study aims to evaluate groundwater quality in the semi-arid Pandameru River Basin, Andhra Pradesh, India, with a focus on its suitability for drinking, agricultural, and industrial use. By integrating the Water Quality Index (WQI) with detailed hydrogeochemical analyses, the research identifies key contaminants and geochemical processes influencing groundwater quality. The novelty of this study lies in the combined application of WQI and localized hydrogeochemical data to offer a nuanced understanding of groundwater quality dynamics in a region critically reliant on this resource. The findings are intended to aid local communities and policymakers by providing actionable insights for sustainable groundwater management, protecting public health, and optimizing agricultural practices in an environment susceptible to contamination and resource depletion. These insights can further inform water quality monitoring initiatives, support the development of pollution mitigation strategies, and contribute to policy frameworks aimed at long-term groundwater conservation in arid and semi-arid regions.

STUDY AREA

The study area is situated in the central part of Anantapur district, Andhra Pradesh, South India, bounded by $14^{\circ}16'N$ to $14^{\circ}40'N$ and $77^{\circ}20'E$ to $77^{\circ}44'E$. It is covered by Survey of India toposheets Nos. 56 F/6, F/7, F/10, and F/11. Geologically, the region falls within the Peninsular Gneissic Complex and comprises lithological units such as hornblende-biotite gneiss (HBN), Closepet granites, and schist formations (Reddy, 1998). This semi-arid region experiences moderate rainfall and significant evapotranspiration, with considerable seasonal temperature variation. The average annual rainfall is approximately 517.8 mm, which plays a crucial role in recharging the aquifers. Groundwater occurs at depths ranging from 10 to 30 meters below ground level (bgl), with the weathered zone extending to 5–15 meters and the fractured zone reaching to depths of 20–50 meters. Groundwater movement generally follows the natural topography, flowing from higher elevations toward lower-lying areas, predominantly in a southerly to south-easterly direction. The region is highly dependent on groundwater resources for both drinking and agricultural needs. However, declining groundwater levels due to seasonal variability and excessive extraction have raised serious concerns about long-term water resource sustainability. Figure 1 presents a detailed map of the study area, illustrating the sampling locations and key hydrogeological features.

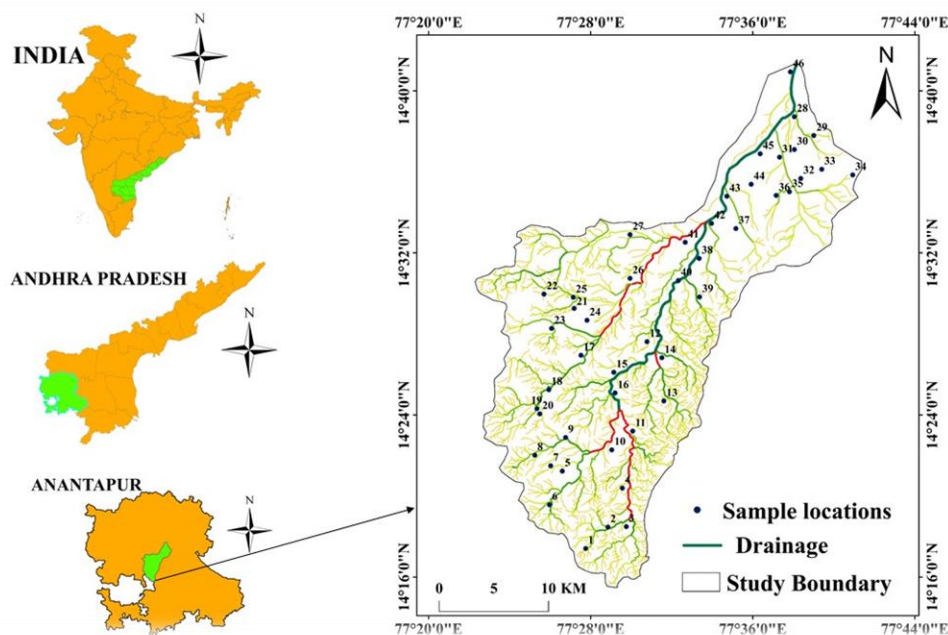


Figure 1. Sample site map of the investigated region in Anantapur district of Andhra Pradesh.

METHODOLOGY

Groundwater quality for drinking and irrigation

To assess the groundwater chemistry, 46 groundwater samples were collected from open wells and bore wells during the both pre-monsoon (March) and post-monsoon (December) seasons in 2023. The study area of the Pandameru River Basin is characterized by diverse lithological variations, and the availability of groundwater varies significantly across different locations. The entire study area is underlain by hard rock aquifers, which influences groundwater distribution and quality. The samples were collected in one-liter plastic bottles, which were pre-cleaned in the laboratory with diluted HNO₃ acid and distilled water to prevent contamination. Additionally, the sampling locations' latitude and longitude were recorded using a GPS device to ensure precise geo-referencing.

Key parameters such as pH, EC, TDS, total hardness (TH), Ca²⁺, Mg²⁺, HCO₃⁻, Cl⁻, Na⁺, K⁺, SO₄²⁻, NO₃⁻, and F⁻ were determined using various analytical methods, including pH and conductivity meters, titration, flame photometry, and spectrophotometry. Sample compatibility with WHO, 2011 drinking water guidelines was assessed. The major cations and anions were graphed on a Piper Trilinear diagram, projecting to a shared diamond-shaped area to classify water types. The Gibbs diagram (Gibbs, 1970) was used to interpret the variables affecting groundwater chemistry quality criteria in the research region. Table 1 shows the irrigations parameters along with formulas.

Precision and Reliability Check

Using standard procedures, we analyzed the acquired samples for major and minor dissolved ions. The total cations and total anion balances were used to calculate the ionic charge balance error percentage, as outlined by Freeze and Cherry (1979). The error percentage in the samples is approximately $\pm 5\%$, with a few outliers attributed to certain ions exhibiting significantly higher levels during different seasons. Errors in groundwater chemical analysis may arise from factors such as the use of reagents, limitations of the techniques and instruments employed the presence of pollutants in distilled water, and other potential sources.

$$\text{IBE (Ionic Balance Error)} = \frac{\sum \text{Cations} - \sum \text{Anions}}{\sum \text{Cations} + \sum \text{Anions}} \times 100 \quad (1)$$

Water Quality Index (WQI)

WQI is an essential statistic for assessing groundwater quality and evaluating whether it is fit for human consumption. WQI is a classification system that evaluates the broad acceptance of water for human consumption using a combination of various water quality parameters (Sharma and Bora, 2020; Kumar et al., 2022; Chinthala et al., 2023). WQI is determined using

WHO (2011) drinking standards. The WQI is calculated in three steps. The constraints (pH, EC, TDS, HCO₃⁻, Cl⁻, F⁻, SO₄²⁻, NO₃⁻, Ca²⁺, Mg²⁺, Na⁺, and K⁺) were each assigned a weight (wi) in the first phase depending on how important they were to the overall quality.

The parameters NO₃⁻, TDS, Cl⁻, F⁻, and SO₄²⁻ have been assigned an extreme weight of 5, owing to their important character in influencing water quality (Table 2). Bicarbonate is assigned a weight of 1 since it has minimal effect on water quality assessment. The remaining variables, such as Ca²⁺, Mg²⁺, Na⁺, and K⁺, were weighted from 1 to 5 to indicate their respective relevance in defining water quality. The relative weight (Wi) is calculated in the initial stage using the formula 2,

$$Wi = \frac{wi}{\sum_{i=1}^n (wi)} \quad (2)$$

The "quality rating (qi)" for the third stage is calculated using Equation 3

$$qi = \left(\frac{ci}{si} \right) \times 100 \quad (3)$$

If Ci represents the attentiveness of each characteristic in each water sample, then Si represents the recommended WHO, (2011) value for each characteristic. The subsequent equations will calculate WQI because Wi and qi were combined to estimate the Sli for each characteristic independently following equations 4 and 5.

$$Sli = wi \times qi \quad (4)$$

$$WQI = \sum_{i=1}^n Sli(5)$$

The sub-index of each parameter is here designated as Sli.

RESULTS AND DISCUSSION

Tables 3 and 4 provide the values of physicochemical parameters measured in mg/L, except EC ($\mu\text{S}/\text{cm}$) for different seasons. The pH of groundwater is a vital hydrologic indicator, with values across both the PRM (7.4–8.3) and POM (7.1–8.3) seasons averaging within WHO's recommended 6.5–8.5 range for human consumption. Electrical Conductivity (EC), which indicates dissolved substances in water, recorded seasonal variations between 1473 and 3254 $\mu\text{S}/\text{cm}$, categorizing the water as moderate to poor quality (WHO threshold: 1500 $\mu\text{S}/\text{cm}$). Total Dissolved Solids (TDS), responsible for hardness and taste, ranged from 1030.8 to 2279 mg/L, classifying all groundwater samples as brackish per Freeze and Cherry standards (Freeze and Cherry, 1979).

Calcium (Ca²⁺) concentrations, crucial for health, fluctuated between 107 and 277 mg/L, with most samples falling within WHO's acceptable range (85% PRM, 78% POM). Magnesium (Mg²⁺), another essential mineral, showed pre- and post-monsoon concentrations from 20 to 142 mg/L, staying well

within the WHO standard. Sodium (Na^+) content, critical for individuals with health conditions, varied from 92 to 348 mg/L; only 74% (PRM) and 48% (POM) of samples were suitable per WHO's 200 mg/L limit, with elevated levels attributed to feldspar weathering.

Potassium (K^+), typically low due to its bond strength in minerals, ranged from 1.0 to 16.6 mg/L, with 74% (PRM) and 69% (POM) samples considered safe. Chloride (Cl^-) levels

varied seasonally, with high concentrations suggesting potential pollution from anthropogenic sources and posing health risks for specific conditions. Sulfate (SO_4^{2-}) levels, driven by industrial emissions and mineral oxidation, remained acceptable in 78% (PRM) and 80% (POM) of samples (Table 5). Bicarbonate (HCO_3^-), indicating alkalinity, surpassed the WHO limit of 600 mg/L in around 40% of samples, likely due to organic matter decomposition (Table 5).

Table 1. Studied irrigational parameters .

Parameters	Formulae	References
Sodium adsorption ratio	$\text{SAR} = \frac{\text{Na}^+}{\frac{\sqrt{\text{Ca}^{2+} + \text{Mg}^{2+}}}{2}}$	Richards (1954)
Percentage sodium	$\% \text{Na} = \frac{\text{Na}^+ + \text{K}^+}{\text{Ca}^{2+} + \text{Mg}^{2+} + \text{Na}^+ + \text{K}^+} \times 100$	Wilcox (1955)
Sodium soluble percentage	$\text{SSP} = \frac{\text{Na}^+}{\text{Ca}^{2+} + \text{Mg}^{2+} + \text{Na}^+ + \text{K}^+} \times 100$	Richards (1954)
Residual sodium carbonate	$\text{RSC} = (\text{HCO}_3^- + \text{CO}_3^{2-}) - (\text{Ca}^{2+} + \text{Mg}^{2+})$	Eaton (1950)
Magnesium adsorption ratio	$\text{MAR} = \frac{\text{Mg}^{2+}}{\text{Ca}^{2+} + \text{Mg}^{2+}} \times 100$	Szabolcs (1964)
Permeability index	$\text{PI} = \frac{\text{Na}^+ + \sqrt{\text{HCO}_3^-}}{\text{Ca}^{2+} + \text{Mg}^{2+} + \text{Na}^+} \times 100$	Doneen (1964)
Kelley's Ratio	$\text{KR} = \frac{\text{Na}^+}{\text{Ca}^{2+} + \text{Mg}^{2+}}$	Kelley (1940)

Table 2. The physiochemical parameters with their allotted and relative weights.

Chemical parameters	Standards (WHO, 2011)	Weight (wi)	Relative weight (Wi)
pH	8.5	4	0.10
TDS	500	5	0.12
Ca^{2+}	75	3	0.07
Mg^{2+}	30	3	0.07
Na^+	200	4	0.10
HCO_3^-	300	1	0.02
F^-	1.5	5	0.12
Cl^-	250	5	0.12
SO_4^{2-}	200	5	0.12
NO_3^-	45	5	0.12
TH	300	2	0.05
		$\Sigma \text{wi} = 42$	$\Sigma \text{Wi} = 1.0$

All parameters are in Mg/L except for pH

Table 3. Physico-chemical analysis of groundwater sample for pre-monsoon season.

S. No	Sample locations	pH	EC ($\mu\text{S/cm}$)	TDS (Mg/L)	Ca ²⁺ (Mg/L)	Mg ²⁺ (Mg/L)	Na ⁺ (Mg/L)	K ⁺ (Mg/L)	HCO ₃ ⁻ (Mg/L)	F ⁻ (Mg/L)	Cl ⁻ (Mg/L)	SO ₄ ²⁻ (Mg/L)	NO ₃ ⁻ (Mg/L)	TH (Mg/L)
1	Kangalakunta	7.9	2028.4	1420	197	24	207	7.2	584	1.27	254	121	34.6	590.9
2	Kanchikunta	7.9	2070.4	1449	216	20	231	10.3	610	1.06	235	112	22.2	622
3	Ramagiri	7.8	2210.5	1547	184	88	192	5.6	564	0.93	198	311	14.4	820.8
4	R. Kothapalli	8	1884.5	1319	136	64	184	6	422	1.96	189	271	45.2	602.4
5	Nasanakota	7.7	1979.7	1386	175	54	196	8	541	1.62	252	93	65.2	658.9
6	Muthyalanpalli	7.9	1540	1078	127	48	138	3	428	1.82	175	129	28.2	514.3
7	Venkatapuram	7.6	1849.3	1294	148	32	188	14	548	0.98	185	157	22.5	501.2
8	K G Kunta	8	1747.4	1223	165	66	102	10	540	1.71	213	87	38.5	683.1
9	Madapuram	8.2	1573.5	1101	129	76	104	8	427	1.98	238	89	28.5	634.1
10	Muthavakuntla	8	1644.2	1151	123	79	106	10	549	1.76	148	116	21.2	631.4
11	Thallimadugula	8	1472.7	1031	118	43	112	1	488	1.98	142	98.9	27	471.3
12	Balepalem	8	1788.9	1252	185	63	92	11	549	2.02	213	87	51.2	720.8
13	Konapuram	7.9	1861.3	1303	131	99	108	12	549	1.92	266	107	29	733.4
14	Kanaganapalli	7.9	1965.4	1376	166	97	102	7	671	1.78	190	107	34	812.7
15	Elakuntla	7.6	1799.8	1260	152	105	116	16.6	549	1.43	162	73.8	84	810.5
16	Nemalivaram	7.7	2032.5	1423	151	112	127	11	610	1.57	240	89	65.2	836.7
17	Bhadhalapuram	7.62	3094	2103	218	135	264	12.3	748	1.38	380	262	82.8	1099
18	Narasampalli	7.8	1773.7	1242	124	91	122	4	598	1.48	167	102	32.1	683.1
19	Somaravandlapalli	7.8	2250.9	1576	175	108	192	6	648	1.82	243	164	85.8	880.3
20	Gudivandlapalli	7.8	2195.3	1537	193	88	132	4	732	1.51	213	128	45.2	843.3
21	Thagarakunta	8	2044.5	1431	184	78	129	5	650	1.62	218	127	38.5	779.8
22	Gunthapalli	8	1624.5	1137	128	76	142	4	419	1.62	239	79	48.5	631.6
23	Patapalyam	8	2108.1	1476	158	82	197	8	629	1.74	208	126	65.9	731.2
24	Pullaiiahkunta	7.6	1565.6	1096	124	57	138	2	428	0.72	213	98	35.2	543.7
25	Bhoginepalli	7.8	1516.1	1061	117	74	97	4	488	1.48	180	80	19.8	595.9
26	Palacherla	8.2	2595	1817	195	125	258	12	629	2.02	312	185	98.5	1000
27	Thopudurthi	8.3	3141	2096	212	142	311	9	784	1.96	328	214	94.2	1112
28	Upparapalle	7.7	2053.9	1438	185	101	94	4	640	1.56	228	134	50.2	876.6
29	Chinnakunta	8	1528.8	1070	132	65	112	10	478	2.14	146	73	52.2	596.5
30	Akuthotapalli	8	3102	2115	221	115	302	11	736	1.88	338	296	93.4	1024
31	Gangulakunta	8.1	2113.4	1479	174	67	191	7	529	2.01	242	192	75.4	709.7
32	Kandukur	7.86	2909.6	2037	227	104	328	9.6	718	1.78	318	240	90.7	993.9
33	Itikalapalli	8.1	3129	2116	268	96	310	8.8	740	1.9	322	311	58.2	1064
34	Krishnama reddy palli	7.7	1960.5	1372	198	70	134	10.4	589	1.44	186	145	38.5	782
35	Jangalapalle	8.2	1639.6	1148	163	69	103	10	448	2.93	203	87	62.5	690.4
36	Ramanepalli	8.1	2087.6	1461	159	127	126	5	549	1.73	249	106	98.6	918.2
37	Gondireddipalli	7.9	1494.3	1046	132	65	108	9	428	1.78	193	72	37.2	596.5
38	yerragunta	7.6	1704.3	1193	154	32	174	9	524	1.54	172	88	38.5	516.2
39	Bandameedapalle	7.4	1573.9	1102	112	85	122	6	419	1.75	182	96	78.5	628.5
40	Varimadugu	7.9	1562.5	1094	139	39	128	3	469	1.78	175	107	75.2	507.4
41	Gandlaparthy	7.5	1886.4	1321	163	77	118	10	489	1.01	155	250	58.2	723.2
42	Pullalarevu	7.4	1857.9	1301	193	70	138	8	589	1.05	186	68.2	68.5	769.5
43	Bommeparthy	7.8	2000.6	1400	185	59	202	12	529	1.44	258	102	72.5	704.4
44	Linganapalli	7.7	2308.6	1616	197	67	216	10	649	1.75	248	162	85.8	767.2
45	Rapthadu	8.09	2761	1822	196	110	244	9.3	632	1.89	320	206	59.1	941
46	Anantapur tank	7.8	3064	2104	218	129	268	12	672	1.79	287	284	103	1074

Table 4. Physico-chemical analysis of groundwater sample for post-monsoon season

S. No	Sample locations	pH	EC (µS/cm)	TDS (Mg/L)	Ca ²⁺ (Mg/L)	Mg ²⁺ (Mg/L)	Na ⁺ (Mg/L)	K ⁺ (Mg/L)	HCO ₃ ⁻ (Mg/L)	F ⁻ (Mg/L)	Cl ⁻ (Mg/L)	SO ₄ ²⁻ (Mg/L)	NO ₃ ⁻ (Mg/L)	TH (Mg/L)
1	Kangalakunta	7.62	1840.6	1164.4	168	47	192	3.7	524	1.45	185	121	46.9	610.6
2	Kanchikunta	7.48	2380.1	1666.1	229	78	262	9.1	592	1.03	282	186.8	76.1	892.0
3	Ramagiri	8.07	2760.0	1932.0	194	95	293	9.4	672	2.72	222	212.5	95.4	874.4
4	R. Kothapalli	8.11	2189.4	1532.6	185	78	227	5.6	576	2.11	242	184.6	52.4	782.4
5	Nasanakota	7.61	2301.5	1483.1	197	86	186	6.6	648	1.93	262	155	70.2	846.6
6	Muthyalanpalli	7.59	1735.8	1215.1	153	75	188	3.2	440	1.06	212	162	30.9	689.5
7	Venkatapuram	7.34	1962.3	1373.6	196	69	207	7	489	0.78	244	187	28.9	775.7
8	K G Kunta	7.91	2045.1	1431.5	185	67	167	12	624	1.67	206	122	47.1	736.1
9	Madapuram	7.55	1846.5	1292.5	157	57	181	14	496	1.46	244	108	33.6	627.9
10	Muthavakuntla	7.32	1721.3	1204.9	149	62	184	10.8	448	1.45	194	162	50.8	626.3
11	Thallimadugula	7.48	1625.1	1137.6	127	76	126	1.5	498	1.34	184	106	28	628.6
12	Balepalem	8.2	1927.1	1349.0	198	73	128	12	529	3.12	242	118	45.7	794.5
13	Konapuram	7.99	2334.6	1634.2	169	125	186	12.8	660	1.89	324	148	51.3	935.7
14	Kanaganapalli	7.83	1873.6	1311.5	193	55	204	8.3	528	1.82	220	127	46.9	709.8
15	Elakuntla	7.99	1998.8	1345.2	159	78	194	13.4	596	2.02	188	104.4	94.2	717.3
16	Nemalivaram	7.77	3189.0	2233.0	198	96	264	9.3	724	2.14	254	216	89.1	890.0
17	Bhadhalapuram	7.62	2355.0	1728.5	168	105	184	8.3	748	0.88	240	142	62.8	849.3
18	Narasampalli	7.49	3106.0	2174.5	167	59	227	12.2	756	1.42	200	98.2	51.2	660.9
19	Somaravandlapalli	7.83	2449.0	1786.3	202	89	232	10.7	648	1.76	288	186	76.6	870.6
20	Gudivandlapalli	7.37	2748.0	1923.6	277	55	287	7.9	818	1.01	242	157	77.9	920.5
21	Thagarakunta	7.52	2312.1	1618.4	187	89	227	6.8	640	1.24	278	174	48.3	832.2
22	Gunthapalli	7.65	1953.5	1367.4	173	75	189	6.1	512	1.44	252	106	52.9	739.7
23	Patapalyam	7.05	2189.7	1602.8	189	78	242	7.8	620	1.18	306	122	67.5	790.3
24	Pullaiahkunta	7.59	1895.1	1326.6	162	67	161	4.1	514	1.67	246	127	43.8	679.8
25	Bhoginepalli	7.94	1738.8	1115.2	146	43	188	6	480	1.6	218	108	26.8	540.4
26	Palacherla	8.01	2078.2	1408.8	178	87	199	9.6	486	2.24	262	194	46.1	804.5
27	Thopudurthi	8.21	3126.6	2188.6	202	128	282	8.8	728	2.03	268	286	93.8	1030.3
28	Upparapalle	8.3	2061.6	1443.1	177	66	196.5	7.1	544	2.42	278	144	55.7	713.8
29	Chinnakunta	7.83	2848.7	1994.0	224	125	268	11.7	742	2.43	296	240	85.4	1070.8
30	Akuthotapalli	7.79	1792.1	1254.5	141	65	152	11	536	1.68	188	96	63.4	620.1
31	Gangulakunta	8.11	2271.7	1421.2	225	82	238	11.6	546	3.11	254	218	73.7	898.0
32	Kandukur	7.86	2079.6	1415.7	167	74	198	8.6	588	1.78	248	90	80.7	719.7
33	Itikalapalli	8.12	2053.9	1397.7	198	66	214	6.8	580	1.9	222	131	78.2	765.3
34	Krishnama reddy palli	7.6	2212.1	1508.5	203	68	247	7.7	552	1.57	226	196	87.1	786.6
35	Jangalapalle	7.69	3144.0	2108.0	219	131	260	10.7	792	1.56	356	248	90.1	1084.6
36	Ramanepalli	7.79	2015.1	1410.5	199	70	214.5	7.7	588	1.53	240	143	46.8	783.2
37	Gondireddipalli	7.86	3067.0	1993.6	255	132	328	9.7	748	1.87	345	220	62	1178.7
38	yerragunta	7.86	2333.0	1634.0	196	84	248	6.1	658	1.98	242	162	85.4	834.4
39	Bandameedapalle	7.69	3254.0	2278.8	119	131	190	10.7	712	1.56	226	148	90.1	834.6
40	Varimadugu	7.45	1826.3	1218.4	178	39	192	6.1	516	1.48	198	138	85.6	605.1
41	Gandlaparthy	7.49	1937.4	1356.2	189	80	217.2	9.8	425	0.91	201	208	95.4	799.3
42	Pullalarevu	7.65	1874.9	1312.4	194	55	158	7.8	580	1.73	212	86	105.4	712.1
43	Bommeparthy	7.82	3025.0	2118.0	187	103	222	9.4	690	1.79	246	128.8	97.9	888.5
44	Linganapalli	7.83	1647.8	1153.5	107	66	151	8.8	496	2.76	184	82	98.4	539.5
45	Rapthadu	7.49	2275.2	1466.6	156	90	214	7.3	628	0.89	232	126	102.5	757.1
46	Anantapur tank	7.83	3118.6	2183.0	245	122	348	10.2	724	1.79	368	246	118.5	1110.7

Table 5. Classification based on physicochemical parameters considering WHO (2011) limiting values.

Parameter	Range	Class	No. of Samples (PRM)	%	No. of Samples (POM)	%
pH	<6.5	Not potable	—	—	—	—
	6.5 - 8.5	Potable	46	100	46	100
	>8.5	Not potable	—	—	—	—
EC	<250	Excellent	-	-	-	-
	250-750	Good	-	-	-	-
	750-2250	Moderate	37	80	26	57
	2250-4000	Bad	9	20	20	43
	>4000	Very bad	-	-	-	-
TDS	0-1000	Fresh water	—	—	—	—
	1000-10000	Brackish water	46	100	46	100
	10000-100000	Saline water	—	—	—	—
	>100000	Brine water	—	—	—	—
Ca ²⁺	<75	Acceptable	—	—	—	—
	75 - 200	Allowable	38	85	36	78
	>200	Not potable	8	15	10	22
Mg ²⁺	<30	Acceptable	2	4	—	—
	30 - 150	Allowable	44	96	46	100
	>150	Not potable	—	—	—	—
Na ⁺	<50	Acceptable	—	—	—	—
	50 - 200	Allowable	34	74	22	48
	>200	Not potable	12	26	24	52
K ⁺	< 10	Acceptable	32	74	32	69
	10-Dec	Allowable	11	20	10	22
	> 12	Not potable	3	6	4	9
Cl ⁻	<250	Acceptable	34	74	30	65
	250 - 300	Allowable	5	11	11	24
	>300	Not potable	7	15	5	11
SO ₄ ²⁻	<200	Acceptable	36	78	37	80
	200 - 400	Allowable	10	22	9	20
	>400	Not potable	—	—	—	—
TH	< 75	Safe	—	—	—	—
	75 - 150	Moderate safe	—	—	—	—
	150- 300	Hard	—	—	—	—
	> 300	Very hard	46	100	46	100
F ⁻	< 0.5	Dental caries	-	-	-	-
	0.6-1.5	Required level for human	15	33	17	37
	1.6-2	Dental fluorosis	26	56	20	43
	2.1-3	Dental and skeletal fluorosis	5	11	7	16
	> 3	leads to skeletal fluorosis	-	-	2	4
NO ₃ ⁻	< 45	Low risk	6	13	4	8
	45 - 100	High risk	37	80	39	85
	> 100	Very high risk	3	7	3	7

Fluoride and Nitrate hotspots

Fluoride concentrations in the investigation region ranges from 0.72 mg/L and 0.8 mg/L to 2.93 mg/L and 3.1 mg/L during the PRM and POM season. Based on the WHO (2011) recommended limit of fluoride levels is 0.6 to 1.5 mg/L for human consumption. Levels below 0.6 mg/L may lead to dental

caries, while levels exceeding 1.2 mg/L can result in fluorosis, which promotes proper bone growth and prevents tooth decay. In the pre-and post-monsoon seasons, 33% and 37% of groundwater samples were below the allowed limits (0.6 to 1.5 mg/L), while 56% and 43% were above the suggested limit of 1.5 mg/L, potentially causing dental fluorosis. Additionally,

11% and 16% of samples had concentrations between 2.1 to 3 mg/L, posing dental and skeletal fluorosis risks in both seasons. Furthermore, 4% of samples had concentrations exceeding 3 mg/L, which could lead to skeletal fluorosis, particularly during the POM season (Table 5, Figure 2).

Nitrate contamination in groundwater stems from various sources and origins. Human activities, such as home sewage leaks, poultry waste dumping, the application of animal manure, and nitrate displacement from garbage, municipal use, and commercial trash, are chiefly responsible for elevated

nitrate levels in groundwater (Singh et al., 2022). Nitrate can enter groundwater through two pathways: geogenic and human-caused processes. During the pre-monsoon season, nitrate levels ranged from 14.4 to 103 mg/L, with an average of 55.50 mg/L, while during the post-monsoon season, it ranged from 26.8 to 119 mg/L, with an average of 68.20 mg/L. In the pre- and post-monsoon seasons, 13% and 8% of groundwater samples are inside the acceptable nitrate limit, 80% and 85% of samples belong to the danger zone, while the remaining 7% and 7% of samples fell in the extremely high-risk zone, as shown in Table 5 and Figure 3.

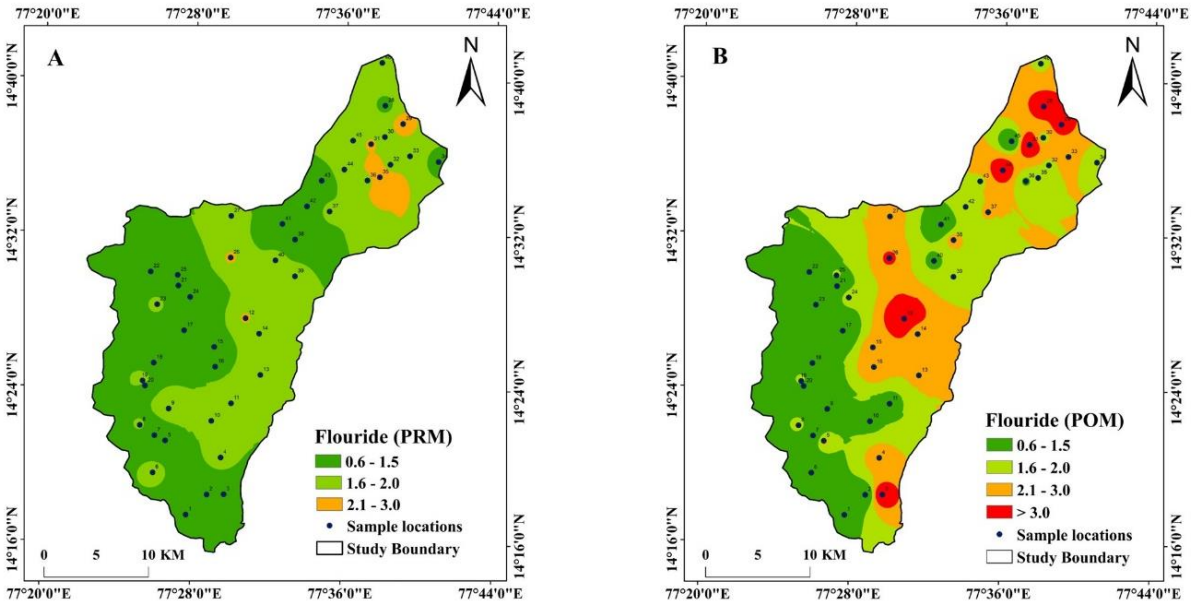


Figure 2. Spatial distribution map of F in the study area (A) Pre-monsoon, and (B) Post-monsoon.

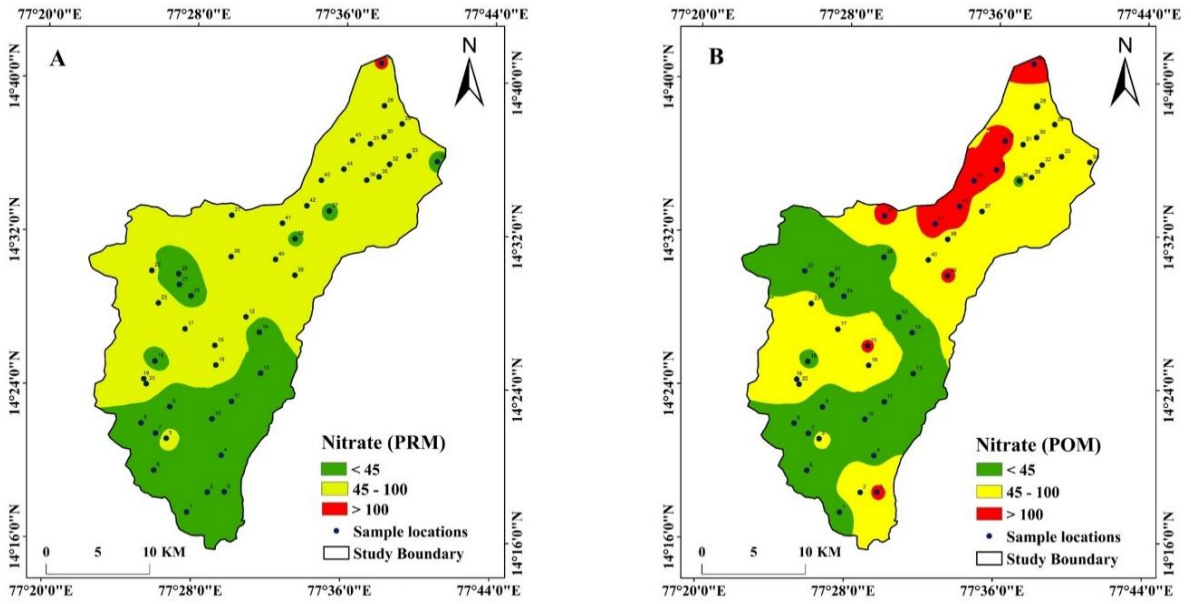


Figure 3. Spatial distribution map of NO₃⁻ in the study area (A) Pre-monsoon, and (B) Post-monsoon.

Total hardness (TH) of water is influenced by the presence of dissolved cations, predominantly calcium (Ca^{2+}) and magnesium (Mg^{2+}) ions, as well as certain anions that cause either temporary or permanent hardness (Sawyer and McCarthy, 1967). Carbonates and bicarbonates produce temporary hardness that can be removed by boiling, while sulphate and chloride ions lead to permanent hardness. According to WHO standards, the maximum acceptable limit for total hardness in drinking water is 500 mg/L. In the PRM season, TH ranged from 214 mg/L to 658 mg/L (Table 3). During the POM season, it varied between 241 mg/L to 681 mg/L (Table 4). Based on these measurements, 57% and 61% of samples exceeded the recommended limit during the PRM and POM seasons, respectively (Table 5), indicating the prevalence of hard water in the region. Excessive hardness in water can lead to issues such as scaling in pipelines, reduced efficiency in soap usage, and potential health concerns when ingested over prolonged periods.

Correlation analysis

Correlation analysis helped in understanding the strength and direction of relationships between various groundwater quality parameters and their combined influence on the hydrochemical characteristics of the study area. Pearson correlation coefficients for both PRM and POM seasons are presented in Table 6 and Table 7, respectively.

EC shows a very strong positive correlation with TDS in both PRM ($r = 0.998$) and POM ($r = 0.988$) seasons, indicating a common source and mutual dependence. This suggests that an

increase in ion concentration (as reflected in TDS), directly increases the EC of groundwater. EC also shows significant positive correlations with other major ions such as Na^+ , Cl^- , and HCO_3^- in both seasons, implying their likely origin from the same lithological sources, mainly due to water-rock interactions (Wagh et al., 2020). TH shows strong positive correlations with Mg^{2+} ($r = 0.871$), HCO_3^- ($r = 0.814$), and Cl^- ($r = 0.771$) during the PRM season, and with Mg^{2+} ($r = 0.835$), Cl^- ($r = 0.809$), and SO_4^{2-} ($r = 0.784$) during the POM season. These results suggest that Mg^{2+} , Cl^- , and SO_4^{2-} are the key contributors to water hardness, particularly in the post-monsoon period. Calcium (Ca^{2+}) exhibits moderate to strong positive correlations with Mg^{2+} ($r = 0.331$ in PRM; $r = 0.262$ in POM), Na^+ ($r = 0.749$ in PRM; $r = 0.750$ in POM), and HCO_3^- ($r = 0.802$ in PRM; $r = 0.503$ in POM), indicating that these ions likely originate from the dissolution of carbonate and silicate minerals within the host rocks. Interestingly, Ca^{2+} also shows a weak negative correlation with fluoride (F^-) during the PRM season ($r = -0.033$), suggesting potential geochemical competition or different geochemical behaviour in fluoride mobilization. Magnesium (Mg^{2+}) shows significant positive correlations with NO_3^- ($r = 0.594$ in PRM; $r = 0.389$ in POM), HCO_3^- ($r = 0.568$ in PRM; $r = 0.632$ in POM), and F^- ($r = 0.225$ in PRM; $r = 0.147$ in POM), highlighting possible anthropogenic contributions and its role in groundwater buffering. These correlations emphasize that groundwater chemistry in the region is primarily controlled by natural geogenic processes with minor anthropogenic influences, especially during the post-monsoon season.

Table 6. Pearson correlation matrix of groundwater parameters for PRM season.

	pH	EC	TDS	TH	Ca2+	Mg2+	Na+	K+	HCO3-	F-	Cl-	SO42-	NO3-
pH	1.000												
EC	0.197	1.000											
TDS	0.184	0.998	1.000										
TH	0.182	0.898	0.899	1.000									
Ca2+	0.114	0.849	0.856	0.752	1.000								
Mg2+	0.176	0.652	0.648	0.871	0.331	1.000							
Na+	0.183	0.876	0.876	0.622	0.749	0.332	1.000						
K+	-0.067	0.343	0.347	0.345	0.366	0.220	0.299	1.000					
HCO3-	0.089	0.849	0.854	0.814	0.802	0.568	0.639	0.277	1.000				
F-	0.672	0.066	0.057	0.140	0.033	0.225	0.002	0.053	-0.035	1.000			
Cl-	0.300	0.861	0.856	0.771	0.710	0.574	0.784	0.302	0.645	0.145	1.000		
SO42-	0.117	0.778	0.778	0.619	0.611	0.430	0.728	0.163	0.502	0.032	0.549	1.000	
NO3-	0.039	0.590	0.597	0.645	0.442	0.594	0.512	0.306	0.401	0.289	0.547	0.312	1.000

Table 7. Pearson correlation matrix of groundwater parameters for POM season.

	<i>pH</i>	<i>EC</i>	<i>TDS</i>	<i>TH</i>	<i>Ca</i> ²⁺	<i>Mg</i> ²⁺	<i>Na</i> ⁺	<i>K</i> ⁺	<i>HCO</i> ₃ ⁻	<i>F</i> ⁻	<i>Cl</i> ⁻	<i>SO</i> ₄ ²⁻	<i>NO</i> ₃ ⁻
<i>pH</i>	1.000												
<i>EC</i>	0.123	1.000											
<i>TDS</i>	0.096	0.988	1.000										
<i>TH</i>	0.203	0.785	0.765	1.000									
<i>Ca</i> ²⁺	0.071	0.486	0.459	0.749	1.000								
<i>Mg</i> ²⁺	0.236	0.740	0.733	0.835	0.262	1.000							
<i>Na</i> ⁺	0.050	0.735	0.709	0.772	0.750	0.503	1.000						
<i>K</i> ⁺	0.232	0.353	0.360	0.308	0.155	0.318	0.165	1.000					
<i>HCO</i> ₃ ⁻	0.072	0.878	0.877	0.721	0.503	0.632	0.618	0.308	1.000				
<i>F</i> ⁻	0.772	0.094	0.064	0.138	0.063	0.147	0.013	0.311	0.027	1.000			
<i>Cl</i> ⁻	0.117	0.568	0.556	0.809	0.602	0.679	0.621	0.228	0.524	0.083	1.000		
<i>SO</i> ₄ ²⁻	0.183	0.598	0.575	0.784	0.609	0.637	0.751	0.146	0.382	0.137	0.581	1.000	
<i>NO</i> ₃ ⁻	0.100	0.497	0.484	0.420	0.270	0.389	0.463	0.265	0.457	0.182	0.176	0.303	1.000

Water Quality index (WQI)

The WQI values are categorized as follows: if the WQI is less than 50, the groundwater is considered excellent; between 50.1 and 100, good quality water; from 100.1 to 200, it is classified as poor; between 200.1 and 300, very poor; and if the values exceed 300, the water is deemed unfit for drinking. This information is summarised in Table 8. Based on the WQI classification, 9 groundwater samples are of good quality, while 37 samples are of poor quality, indicating that 19% of the study area has good-quality water, and 81% suffers from poor-quality water. In the post-monsoon season, 12 groundwater samples show good quality, whereas 34 samples demonstrate poor quality. This reveals that 26% of the study area has good-quality water, and 74% experiences poor-quality water. The elevated WQI values may be linked to higher levels of Total Dissolved Solids (TDS), Electrical Conductivity (EC), and Total Hardness (TH), suggesting that the groundwater is unsuitable for drinking purposes.

The IDW interpolation method was employed using ArcGIS software to create a spatial distribution map based on the WQI values of each sample. This study strongly advocates for using GIS to assess water quality and explore regional variations. The spatial distribution maps of the WQI in the research area, as depicted in Figure 4, provide valuable information to the public regarding water quality in specific areas and serve as a tool to raise awareness among local residents about the importance of safeguarding water quality in the region. A comprehensive classification of WQI for both the pre- and post-monsoon seasons is presented in Table 8, with higher WQI values observed in the post-monsoon season compared to the pre-monsoon season.

Irrigation Water Quality

To assess the suitability of groundwater quality for irrigation, several fundamental ratios such as SAR, RSC, Na%, MAR, SSP, KR, and PI were used for the interpretation.

Sodium Adsorption Ratio (SAR)

The Sodium Adsorption Ratio (SAR) is a measure that evaluates the relative and absolute concentration of sodium ions in comparison to calcium and magnesium ions. SAR values are directly correlated with the soil's sodium absorption capacity (Ahmed et al., 2020). During the pre-monsoon season, SAR values range from 1.38 to 4.53 meq/L (Table 9). In the post-monsoon season, 1.97 to 4.55 (Table 9). Based on Richards (1954) classification, all groundwater samples in this study area (100%) fall into the "excellent" category for irrigation during both seasons Table 10).

Residual sodium carbonate (RSC)

The RSC content in water reflects a notably high concentration of bicarbonate ions (HCO_3^-) relative to other negative ions, as observed in Table 9. Consequently, carbonate ions (HCO_3^- and CO_3^{2-}) influence water quality by precipitating alkaline earth ions (Ca^{2+} and Mg^{2+}) in areas where water concentration is higher. During the pre-monsoon (PRM) season, RSC values ranged from -10.50 meq/L to 2.91 meq/L (Table 9). In the post-monsoon (POM) season, it ranged from -11.38 meq/L to 3.20 meq/L (Table 9). According to Eaton (1950) classification, 96% and 94% of samples are classified as appropriate for farming, 2% and 2% are dubious, and 2% and 4% are unsuitable for irrigation in the PRM and POM seasons, respectively (Table 10).

Percent sodium (%Na)

Soil permeability is lowered when sodium replaces calcium. The %Na is significant for classifying irrigation water. Wilcox (1955) percentage Na values are used to classify the purity of water used for farming. Sodium mixes with carbonates and chlorides to form alkaline and saline soils. Plants develop poorly in alkaline or salty soils. A sodium level of 60% is allowed in groundwater for purposes of agriculture (Mukherjee et al., 2022). In the PRM, the %Na levels fluctuated between 19.29 meq/L and 46.67 meq/L (Table 9) and in POM, between

27.00 and 43.55 (Table 9). As per Wilcox (1955) categorization, 87% and 80% of samples are good, while 13% and 20% are permitted for irrigation during both seasons (Table 10).

Sodium Soluble Percentage (SSP)

The Sodium Soluble Percentage (SSP) ratio, proposed by

Richards (1954), helps assess sodium-related hazards by comparing the concentration of sodium ions to total cations. During the PRM season, SSP values ranged from 18.82% to 45.48% at Thopudurthi and Kanchikunta (Table 9). In the POM season, SSP values ranged from 25.59% to 42.75% in Balepalem and Pullaiahkunta (Table 9).

Table 8. Classification of water quality types based on WQI (Karunanidhi et al., 2021)

WQI range	Water quality status	% of water samples (PRM)	% of water samples (POM)
< 50	Excellent	–	–
50.1-100	Good	19 (9 samples)	22 (10 Samples)
100.1-200	Poor	81 (37 samples)	74 (34 samples)
200.1-300	very poor	–	4(2 samples)
>300	Unsuitable for drinking	–	–

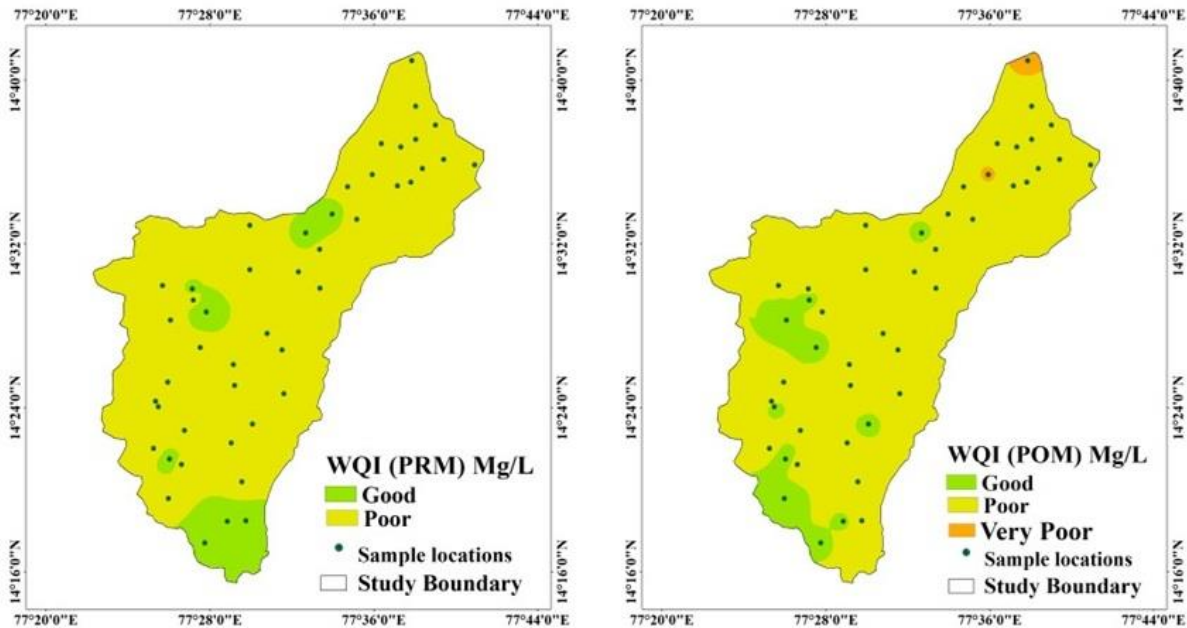


Figure 4. Spatial distribution map of Water quality index (WQI) in the study area during pre-monsoon and post-monsoon.

Table 9. Groundwater quality parameters for irrigation purposes for the pre-monsoon (PRM) and post-monsoon (POM) seasons.

Parameters	PRM				POM			
	Minimum	Maximum	Average	Std.Dev	Minimum	Maximum	Average	Std.Dev
SAR (meq/L)	1.38	4.53	2.66	0.88	1.97	4.55	3.3	0.53
RSC (meq/L)	-10.5	2.91	-4.9	2.9	-11.38	3.2	-5.6	2.99
%Na (meq/L)	19.29	46.67	32.86	6.98	27	43.55	37.44	3.41
SSP (meq/L)	18.82	45.48	31.91	7.02	25.59	42.75	36.56	3.46
MAR (meq/L)	12.77	56.82	42.92	9.74	39.66	57.97	49.52	3.55
KR (meq/L)	0.23	0.85	0.49	0.16	0.35	0.76	0.59	0.08
PI (meq/L)	33.85	61.44	46.43	6.68	24.76	64.56	41.61	7.37

Table 10. Classification of groundwater based on irrigational water quality parameters during pre-monsoon (PRM) and post-monsoon (POM) seasons

Parameter	Water quality	Ranges	% of groundwater samples (PRM)	% of groundwater samples (POM)
SAR (Richards, 1954)	Excellent	0 – 10	100%	100%
	Good	10–18	Nil	Nil
	Doubtful	18-26	Nil	Nil
	Unsuitable	> 26	Nil	Nil
RSC (Eaton,1950)	Good	< 1.25	96%	96%
	Doubtful	1.25 – 2.50	2%	2%
	Unsuitable	> 2.50	2%	2%
%Na (Wilcox, 1955)	Excellent	< 20	Nil	Nil
	Good	20 – 40	87%	87%
	Permissible	40–60	13%	13%
	Doubtful	60–80	Nil	Nil
SSP (Richards, 1954)	Good	< 50	100%	100%
	Unsuitable	> 50	Nil	Nil
MAR (Szabolcs, 1964)	Suitable	< 50	74%	74%
	Unsuitable	> 50	26%	26%
KR (Kelley, 1940)	Suitable	<1	100%	100%
	Unsuitable	>1	Nil	Nil
PI (Doneen, 1964)	unsuitable	< 25 Class-III	Nil	Nil
	Good	25 – 75 class-II	100%	100%
	Excellent	>75 class- I	Nil	Nil

Based on Richards (1954) assessment, 100% of groundwater samples in both seasons fall within the "superior" range for farming suitability (Table 10).

Wilcox Diagram

Wilcox (1955) developed a diagram to determine the suitability of groundwater for irrigation by combining electrical conductivity (EC) and sodium percentage (%Na). This model divides the diagram into five distinct zones: excellent to good, good to permissible, permissible to doubtful, doubtful to unsuitable, and unsuitable, with increasing salinity and sodium content posing potential threats to agriculture. According to this categorization, 56% and 37% of groundwater samples fall within the good to permissible zone, while 33% and 46% are categorized as doubtful to unsuitable, and 11% and 17% are classified as unsuitable for irrigation during the PRM and POM seasons, respectively (Figure 5). These results highlight variations in the suitability of groundwater resources for agricultural use between the pre- and post-monsoon seasons.

USSL Diagram

The interpretations of the USSL (1954) for rating irrigation

water are shown in Figure 6, where Sodium Adsorption Ratio (SAR) data is plotted against specific conductance (EC). In the pre-monsoon (PRM) season, the majority of samples (78%, 36 samples) fall within the C3S1 category, indicating moderate salinity and low sodium hazard. A smaller proportion (9%, 4 samples) falls within the C4S1 category, which represents high salinity and low sodium hazard, while 13% (6 samples) belong to the C4S2 category, indicating high salinity and moderate sodium hazard, according to the USSSL (1954) classification.

In the post-monsoon (POM) season, the distribution shifts slightly: 58% (27 samples) are categorized as C3S1, 20% (9 samples) fall in the C4S1 category, and 22% (10 samples) are in the C4S2 category. These findings suggest that high saline and alkali levels in some areas may reduce the suitability of groundwater for agricultural use, especially in locations with poor drainage. Overall, the groundwater chemistry in the study area reflects moderate water quality, which is significantly influenced by the underlying host rock. This influence is evident in both the water type and chemical composition, with implications for its use in agriculture and human activities.

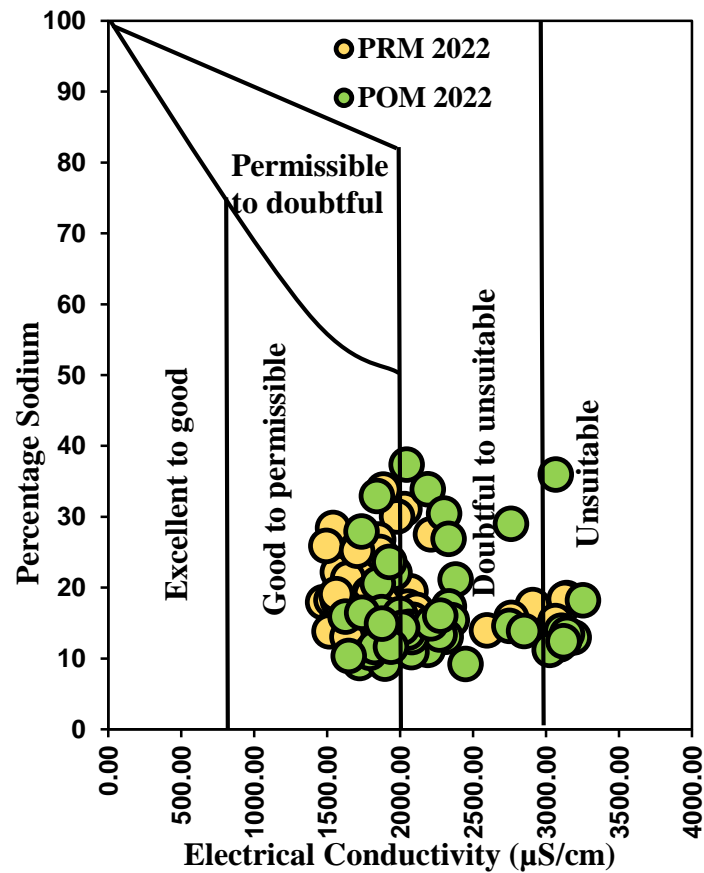


Figure 5. Wilcox diagram of the study area (Pre Monsoon and Post Monsoon)

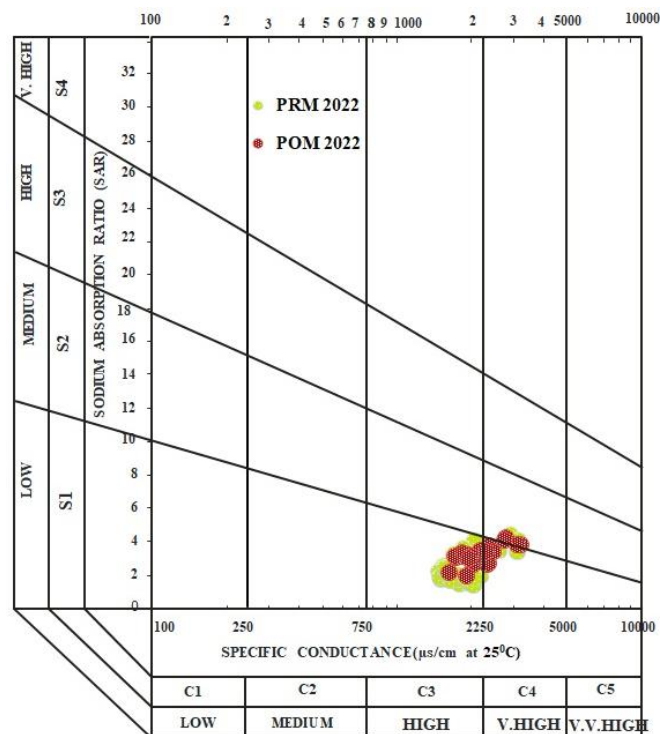


Figure 6. USSL (1954) diagram of the investigation region in PRM and POM seasons

Magnesium Absorption Ratio (MAR)

Magnesium concentration is a critical factor in evaluating the suitability of water for irrigation. The balance between calcium and magnesium in water is important, and increasing magnesium levels can harm crop yields, especially in saline soils (Szabolcs, 1964; Zhang et al., 2020). In the pre-monsoon (PRM) season, the MAR values ranged from 12.77 meq/L to 56.82 meq/L (Table 9). In the post-monsoon (POM) season, MAR values ranged from 39.66 meq/L to 57.97 meq/L (Table 9). Based on Szabolcs (1964) classification, 74% and 92% of the samples fall under the "suitable" category for irrigation, while 26% and 8% are categorized as "unsuitable" during the two seasons, respectively (Table 10).

Kelley's ratio (KR)

The Kelley Ratio (KR), introduced by Kelley (1940) evaluates the sodium concentration in water relative to calcium (Ca^{2+}) and magnesium (Mg^{2+}). A KR value exceeding 1 indicates high sodium levels, rendering the water unsuitable for irrigation. For acceptable irrigation standards, the KR value should be less than 1. In the pre-monsoon season, KR values ranged from 0.23 meq/L to 0.85 meq/L, while in post monsoon season KR values ranged from 0.35 meq/L to 0.6 meq/L (Table 9). According to this classification, all groundwater samples (100%) are categorized as "suitable" for irrigation during both the seasons (Table 10).

Permeability Index (PI)

The permeability of soil is an important factor for assessing the suitability of water for irrigation. The permeability index (PI) helps classify water into three categories: Class I and Class II waters are suitable for irrigation with high permeability (above 75%), while Class III waters are less suitable with lower permeability (below 25%) (Doneen, 1964). In the pre-monsoon season, PI ranged from 33.85 meq/L to 61.44 meq/L (Table 9) and in the post-monsoon season, 24.76 meq/L to 64.56 meq/L (Table 9). According to Doneen (1964) classification, all groundwater samples (100%) fall under the "good" category for irrigation during both seasons (Table 10).

Hydrogeochemical facies -Piper Trilinear Diagram Interpretation

Piper's classification, introduced in 1944 and refined in 1953, is a widely used method for characterizing the chemical composition of groundwater (Piper 1944, 1953). It utilizes a trilinear diagram to classify ion dominance and provides a more accurate assessment of groundwater chemistry compared to other methods. The diagram consists of a central diamond-shaped field with six distinct subfields that represent different ion pairings viz.,

- (i) Ca^{2+} - HCO_3^-
- (ii) Na^+ - Cl^-
- (iii) Mixed Ca^{2+} - Na^+ - HCO_3^-
- (iv) Mixed Ca^{2+} - Mg^{2+} - Cl^-
- (v) Ca^{2+} - Cl^-
- (vi) Na^+ - HCO_3^-

Based on the results from this study (Figure.7a, b) the majority of groundwater samples from both the pre-monsoon (PRM) and post-monsoon (POM) seasons fall into the Ca^{2+} - HCO_3^- and Ca^{2+} - Mg^{2+} - Cl^- facies. These findings suggest that groundwater chemistry is predominantly influenced by ion exchange processes and the weathering of silicate rocks, particularly granite gneisses. The water chemistry typically results from the interaction between rainwater or groundwater and carbonate rocks.

The presence of high concentrations of Ca^{2+} contributes to water hardness, which, while not a health hazard, can reduce palatability. Elevated HCO_3^- levels increase water alkalinity, thereby enhancing its capacity to neutralize acids, which can impact the pH of the water. Furthermore, high alkalinity can affect the effectiveness of chlorine disinfection and lead to the precipitation of calcium carbonate in soils. This can reduce soil permeability and aeration, ultimately affecting plant growth by altering nutrient availability and increasing soil pH. High chloride (Cl^-) concentrations elevate the salinity of groundwater, which can impair water palatability and, if excessive, pose health risks for individuals with hypertension or kidney issues. Additionally, high salinity can inhibit plant growth, reduce crop yields, and be toxic to sensitive plant species. Elevated levels of calcium and magnesium can also alter soil structure, contributing to soil salinization, which makes the land unsuitable for agriculture.

The study suggests that high-salinity water, basically from surface contaminated sources such as irrigation return flow, domestic wastewater, and septic tank effluents, do mix with existing groundwater, which modifies the water chemistry, further influencing the observed facies in the Piper diagram. Understanding these interactions between surface contamination and groundwater is crucial for gaining insights into the regional hydrogeochemical profile (Ayyandurai and Venkateswaran, 2022).

Gibbs Diagram

In 1970, Gibbs introduced a diagram to explore the factors influencing the chemical composition of water, emphasizing the interaction between geological formations and water chemistry.

The Gibbs plot serves as a tool for identifying the primary mechanisms affecting groundwater composition, such as evaporation, precipitation, and rock-water interaction. Based on the analysis of the Gibbs diagram for both cations and anions, the results show that 100% of the water samples fall under the rock dominance category during both the pre-monsoon and post-monsoon seasons (Figure 8a,b). This indicates that the chemical composition of groundwater is primarily influenced by the weathering of rocks, such as

silicate minerals, rather than by processes like evaporation or precipitation. The dominance of hornblende biotite gneiss rock during water interaction in this study, highlights the significant role of geological formations in shaping the groundwater's chemical profile, a pattern that remains consistent across both seasons. This finding reinforces the importance of understanding the geological context in hydrogeochemical studies, as the interaction between water and rock formations plays a key role in determining water quality in the region.

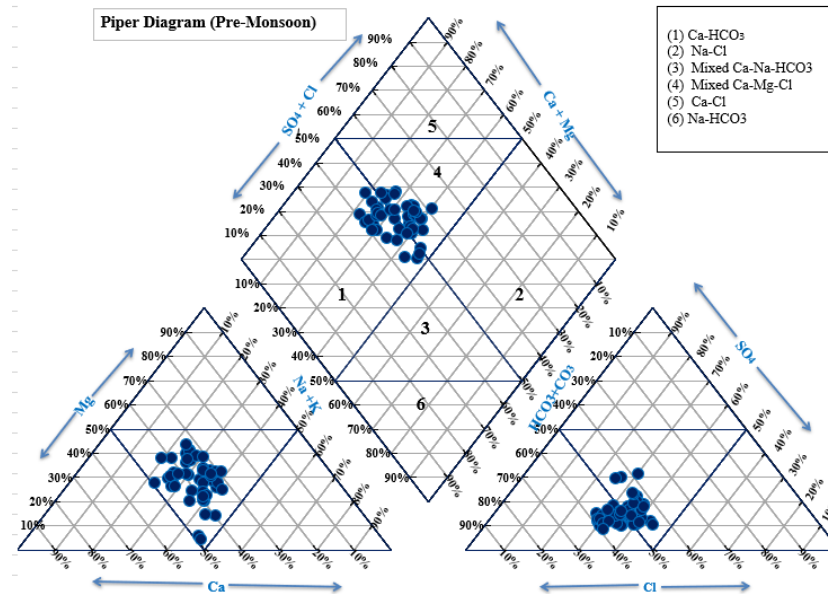


Figure 7a. Piper plot displaying water type in the investigation region during pre-monsoon (PRM) period.

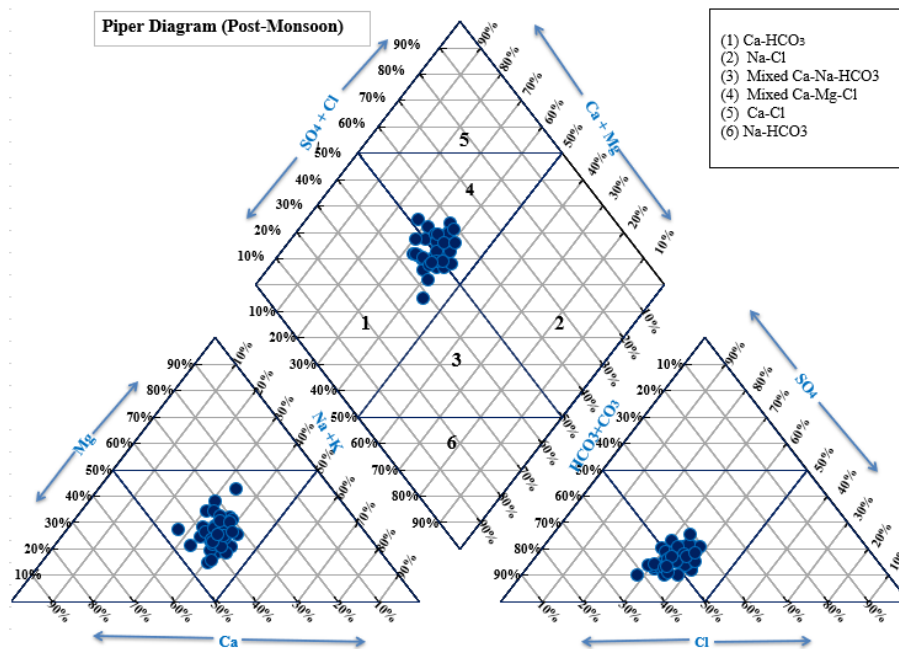


Figure 7b. Piper plot displaying water type in the investigation region during post-monsoon (POM) periods

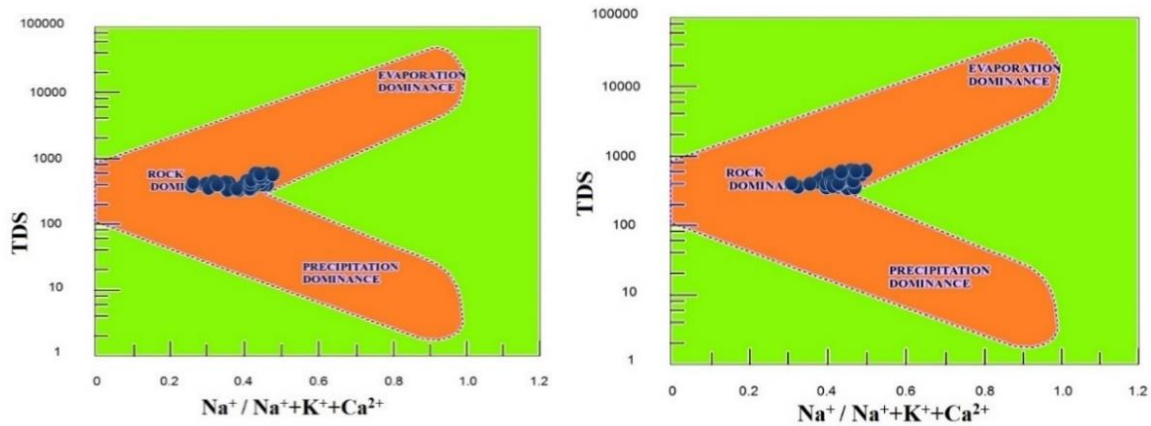


Figure 8a. Gibbs Plots for Cation. PRM season (left panel) and POM season (right panel)

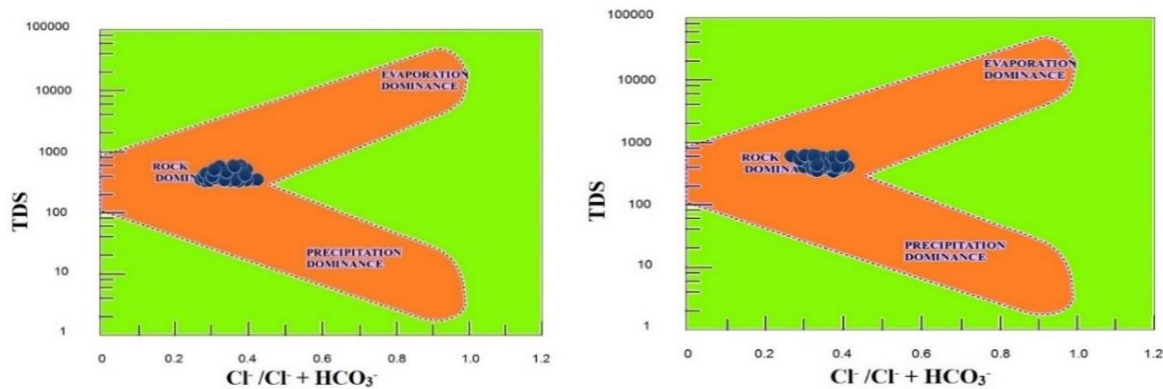


Figure 8b. Gibbs Plots for Anion. PRM season (left panel) and POM season (right panel)

CONCLUSIONS

This study assess the quality of groundwater for drinking and agricultural purposes in the semi-arid regions of Andhra Pradesh, India, based on samples collected during the Pre Monsoon (PRM) and Post Monsoon (POM) seasons of 2023. Geochemical analyses revealed that the predominant cation and anion composition of the groundwater samples was Na^+ , Ca^{2+} , and Mg^{2+} , along with HCO_3^- , Cl^- , and SO_4^{2-} . Despite the samples remaining within the potable pH limits, 87% and 92% of the samples during the PRM and POM seasons, respectively, exceeded the desirable nitrate levels, and fluoride concentrations exceeded the permissible limit in 67% and 59% of samples, mainly due to agricultural and geogenic sources. The WQI indicated that only a small proportion of samples were safe for drinking, with the remaining samples deemed unsafe due to contamination from sewage, agricultural runoff, and poor groundwater management. The elevated WQI values in the POM season, compared to the PRM season, reflected deterioration in water quality over time, driven by rising TDS, EC, and TH. Piper's diagram showed the predominance of $\text{Ca}^{2+}\text{-HCO}_3^-$ and $\text{Ca}^{2+}\text{-Mg}^{2+}\text{-Cl}^-$ facies, highlighting the influence of high-salinity water due to surface contamination

and interaction with silicate rocks, such as granite gneisses. Gibbs diagram analysis confirmed that groundwater chemistry is largely influenced by the weathering of geological formations. According to the US Salinity Laboratory and Wilcox's classification, most samples were suitable for irrigation purposes.

GIS-based spatial analysis also confirmed the partial suitability of groundwater for domestic use, with significant variations in quality across the study area. Groundwater quality issues persisted despite high rainfall during the NE monsoon season, suggesting that improper groundwater management and inadequate artificial recharge are key factors. The predominant lithology, particularly granitic rocks, contributes to high concentrations of calcium and magnesium, while basaltic formations may influence other ion concentrations. These variations in rock types play a critical role in groundwater quality concerns. To improve water quality and ensure sustainability, effective management strategies such as constructing artificial recharge structures, implementing rainwater harvesting systems, and improving groundwater management practices are essential, especially tailored to the region's lithological conditions.

Acknowledgement

The authors are thankful to the Department of Geology, Yogi Vemana University, for providing necessary facilities to carry out the research work. P. Ravi Kumar received financial support from the Department of Science and Technology (DST), Government of India, through the Inspire Program (Sanction Order No. DST/INSPIRE Fellowship/2018/IF180877).

Author Credit Statement

Ravi Kumar Pappaka: Manuscript preparation, sample collection, and methodology; Srinivasa Gowd Somagouni: Manuscript preparation and corrections; Krupavathi Chinthala: Sample collection, methodology; Pradeep Kumar Badapalli: Manuscript Corrections, revisions, and GIS mapping

Data Availability

Data will be made available on reasonable request from the corresponding author.

Compliance with Ethical Standards

The authors declare that they have no conflict of interest and adhere to copyright norms.

References

- Ahmed, S., Khurshid, S., Sultan, W. and Shadab, M. B., 2020. Statistical analysis and water quality index development using GIS of Mathura City, Uttar Pradesh, India. *Desalination and Water Treatment*, 177(12), 152-166.
- Anusha, B. N., Babu, K. R., Kumar, B. P., Kumar, P. R. and Rajasekhar, M., 2022. Geospatial approaches for monitoring and mapping of water resources in semi-arid regions of Southern India. *Environmental Challenges*, 8 (8), 1-13.
- Asadi, E., Isazadeh, M., Samadianfard, S., Ramli, M. F., Mosavi, A., Nabipour, N. and Chau, K. W., 2019. Groundwater quality assessment for sustainable drinking and irrigation. *Sustainability*, 12(1), 1-13.
- Ayyandurai, R., and Venkateswaran, S., 2022. An Investigation of Groundwater Hydrochemistry in the Shallow Aquifers of the Cuddalore Coast, South India. In: *Climate Change Impact on Groundwater Resources: Human Health Risk Assessment in Arid and Semi-arid Regions*. Cham: Springer International Publishing. pp.117-138
- Badapalli, P. K., Nakkala, A. B., Kottala, R. B. and Gugulothu, S., 2024. Geo environmental green growth towards sustainable development in semi-arid regions using physicochemical and geospatial approaches. *Environmental Sci. Pollution Res.*, 31(41), 54089-54106.
- Chinthala, K., Somagouni, S. G., Pappaka, R. K. and Gudala, H. V., 2023. Ground Water Quality Assessment Using Water Quality Index and Geographical Information System of Mogamururu River Basin, YSR Kadapa District, Andhra Pradesh, India. In: *Emerging Technologies for Water Supply, Conservation and Management*, Cham: Springer International Publishing. pp 291-313
- Doneen, L. D., 1964. Notes on water quality in agriculture. Department of Water Science and Engineering, University of California, Davis.
- Dutta, N., Thakur, B. K., Nurujjaman, M., Debnath, K. and Bal, D. P., 2022. An assessment of the water quality index (WQI) of drinking water in the Eastern Himalayas of South Sikkim, India. *Groundwater for Sustainable Development*, 17, 100735.
- Eaton, F. M., 1950. Significance of carbonates in irrigation waters. *Soil science*, 69(2), 123-134.
- Freeze, R. A. and Cherry, J. A., 1979. *Groundwater*. Prentice hall Inc. Englewood cliffs. New Jersey, 604.
- Gibbs, R. J., 1970. Mechanisms controlling world water chemistry. *Science*, 170(3962), 1088-1090.
- Golla, V. S. and Badapalli, P. K., 2022. Evaluation of water quality for drinking and irrigation purposes and Fluoride Health Hazard Risk Assessment (HHRA) in parts of semi-arid regions in the south-eastern part of India. *Int. J. Energy and Water Resources*, 6(4), 521-529.
- Gugulothu, S., Subbarao, N., Das, R. and Dhakate, R., 2022. Geochemical evaluation of groundwater and suitability of groundwater quality for irrigation purpose in an agricultural region of South India. *Applied Water Sci*, 12(6), 1-13.
- Karunanidhi, D., Aravinthasamy, P., Subramani, T. and Muthusankar, G., 2021. Revealing drinking water quality issues and possible health risks based on water quality index (WQI) method in the Shanmuganadhi River basin of South India. *Environmental Geoch. and Health*, 43, 931-948.
- Kelley, W. P., 1940. Permissible composition and concentration of irrigation water. *Proc. Am. Soc. Civil Engineers*, 66, 607-613.
- Khatri, N., Tyagi, S., Rawtani, D., Tharmavaram, M. and Kamboj, R. D., 2020. Analysis and assessment of ground water quality in Satlasana Taluka, Mehsana district, Gujarat, India through application of water quality indices. *Groundwater for Sustainable Development*, 10(4), 1-8.
- Kumar, P.R., Gowd, S. S., Krupavathi, C. and Kumar, B.P., 2022. Groundwater quality assessment using Water Quality Index (WQI) in parts of Anantapur, A.P. (India). *J. Ind. Geophys. Union*, 26(2), 155-164.
- Molagamudi, S. R., Uravakonda, S., Badapalli, P. K. and Golla, V. S., 2023. Evaluation of groundwater chemistry and its impact on drinking, irrigation, and human health hazard risk assessment (HHRA) in Pincha river basin, semi-arid region of Andhra Pradesh, India. *Int. J. Energy and Water Res.*, 7(3), 347-353.
- Mukherjee, I., Singh, U. K. and Chakma, S., 2022. Evaluation of groundwater quality for irrigation water supply using multi-criteria decision-making techniques and GIS in an agro-economic tract of Lower Ganga basin, India. *J. Environmental Manag.*, 309, 114691.
- Nayak, A., Matta, G. and Uniyal, D. P., 2023. Hydrochemical characterization of groundwater quality using chemometric analysis and water quality indices in the

- foothills of the Himalayas. *Environ. Development and Sustainability*, 25(12), 14229-14260.
- Pappaka, R. K., Somagouni, S. G., Chinthala, K. and Nakkala, A. B., 2024. Appraisal of groundwater quality for suitability of drinking and irrigation purposes of Pandameru river basin, Anantapur district, AP, India. *Arabian J. Geosci.*, 17(1), 1-16.
- Parveen, N., Giri, S., Singh, A. K. and Tripathi, J. K., 2025. Fluoride and nitrate contamination in groundwater of Naini Industrial Area, Uttar Pradesh: Assessing non-carcinogenic human health risk. *Groundwater for Sustainable Development*, 28, 101388.
- Piper, A. M., 1944. A graphic procedure in the geochemical interpretation of water-analyses. *EOS, Trans. Am. Geophys. Union*, 25(6), 914-928.
- Piper, A. M., 1953. A graphic procedure in the geo-chemical interpretation of water analysis. *USGS groundwater note*, pp. 12
- Reddy, K. V. S., 1998. Compilation of STM geological maps of the Peninsular gneissic complex, Anantapur district, A.P. *Rec. Geol. Surv. India*, 132(pt 5), 5-7.
- Richards, L. A. (Ed.), 1954. *Diagnosis and improvement of saline and alkali soils* (No. 60). US Government Printing Office.
- Sawyer, C. N. and McCarty, P. L., 1967. *Chemistry for sanitary engineers* (Vol. 518). New York: McGraw-Hill.
- Sharma, P. and Bora, P. J., 2020. Water quality assessment using water quality index and principal component analysis: A case study of historically important lakes of Guwahati City, North-East India. *Appl. Ecology and Environmental Sci.*, 8(5), 207-217.
- Singh, S., Anil, A. G., Kumar, V., Kapoor, D., Subramanian, S., Singh, J. and Ramamurthy, P. C., 2022. Nitrates in the environment: A critical review of their distribution, sensing techniques, ecological effects and remediation. *Chemosphere*, 287 (8), 1-18.
- Subba Rao, N., Srihari, C., Deepthi Spandana, B., Sravanthi, M., Kamalesh, T. and Abraham Jayadeep, V., 2019. Comprehensive understanding of groundwater quality and hydrogeochemistry for the sustainable development of suburban area of Visakhapatnam, Andhra Pradesh, India. *Human and Ecological Risk Assessment: An International Journal*, 25(1-2), 52-80.
- Szabolcs, I., 1964. The influence of irrigation water of high sodium-carbonate content on soils.
- USSL., 1954. *Diagnosis and improvement of salinity and alkaline soil*. USDA Hand Book no. 60, Washington
- Wagh, V. M., Panaskar, D. B., Mukate, S. V., Aamalawar, M. L. and Laxman Sahu, U., 2020. Nitrate associated health risks from groundwater of Kadava river basin Nashik, Maharashtra, India. *Human and Ecological Risk Assessment: an international journal*, 26(3), 654-672.
- WHO, 2011. *World Health Organization., Guidelines for drinking-water quality*. World Health Organization.
- Wilcox, L., 1955. *Classification and use of irrigation waters*. US Department of Agriculture, No. 969.
- Zhang, Q., Xu, P. and Qian, H., 2020. Groundwater quality assessment using improved water quality index (WQI) and human health risk (HHR) evaluation in a semi-arid region of northwest China. *Exposure and Health*, 12(3), 4

Received on: 02-12-2024; Revised on: 24-06-2025 ; Accepted on: 29-06-2025

A geochemical study on the Lansdowne granite and granite gneiss, Garhwal Lesser Himalaya, Uttarakhand (India)

Deepa Arya¹, Gunjan Arya^{1,2}, R.B. Ananth³

¹Department of Geology, CAS, Kumaun University, Nainital, Uttarakhand-263001, India.

²Department of Geology, B.D. Govt. P.G. College Jaiharikhal, Pauri Garhwal, Uttarakhand- 246193, India.

³Department of Geology, Institute of Science, Banaras Hindu University, Varanasi- 221005, India

*Corresponding author: arya.earth11@gmail.com

ABSTRACT

The Lansdowne klippe in the Lesser Himalaya is a thrust-plunging syncline comprising Precambrian granite and granite gneiss, prominently exposed around Jaiharikhal-Lansdowne in Garhwal region. The study area consists of metasedimentary rocks, quartzose-phyllite, mylonite/phyllonite, granitic and augen gneisses. Granites exhibit medium-coarse, hypidiomorphic, and porphyritic textures with minerals Pl-Kfs-Qtz-Bt-Mus-Tour-Mag-Ap-Zr-Ep. Granite gneisses exhibit a mineral composition similar to that of granite, but with a well-developed foliation plane. Near fault zones, mylonitic textures with quartz ribbons and sericite occurrences, indicate NW-SE shearing. Textural features (porphyritic, perthitic) and geochemical characteristics (alkalic-ferroan, peraluminous), suggest slow cooling from a direct magmatic origin within syn-collisional to post-orogenic settings.

Keywords: Garhwal Himalaya, Lansdowne-Jaiharikhal granite and granite gneiss, Lansdowne klippe, Mineral chemistry, Geochemistry, Syn-collisional.

INTRODUCTION

Since ~55 Ma, intense Cenozoic crustal thickening of the crust created the Himalayas due to continental collision between India and Eurasia. Since the Proterozoic era, various granitoids have been emplaced until recent times. The intense pressure and temperature, generated during this process, caused the partial melting of the continental crust leading to the formation of large volumes of granitic magma (Rai and Kumar, 2015). Five significant belts of granite plutons in the Himalaya based on geographical distribution are, Karakoram axial batholith, Trans-Himalayan batholith, Northern Himalayan Granite belt, granitoids of the Higher Himalayan Crystalline belt, and Lesser Himalayan Granite belt (Le Fort, 1988). The occurrences of granites from the Lesser Himalayan sequence, are well exposed in the Himachal and Garhwal-Kumaon regions of the Himalayas (Bhatnagar and Sharma, 1989; Tandon and Bhatt, 1995; Santosh et al., 2003; Islam et al., 2005). These granites were formed by the partial melting of a metasedimentary source rock, possibly a pelitic rock, in a continental crustal setting (Chakraborty et al., 1994; Dasgupta et al., 1996; Upadhyay and Singh, 2000).

The earlier works in the Lansdowne region (Auden, 1937; Shanker and Ganesan 1973) proposed that the granite gneiss intruded into underlying metamorphites (chandpurs/ chails) before the formation of the Garhwal thrust (pre-Miocene). Vishnoi (1971) provided detailed information about the geology of the area. Eldson and Gupta (1981) determined petrochemical properties and suggested magmatic origin of granite gneisses, with pronounced gneissosity due to later deformation. This paper focuses on the analysis of geochemical and mineral chemistry data of the area in order to enhance our

knowledge to understand the origin, crustal evolution and tectonic setting.

GEOLOGY AND FIELD RELATIONSHIP

The proposed study area lies in the Lansdowne Pauri Garhwal, Lesser Himalaya, Uttarakhand. It lies between latitudes 29°49'0" N and 29°51'30" N and longitudes 78°39'0" E and 78°41'30" E in Geological Survey of India toposheet no. 53K/9. Lesser Himalaya meta-sedimentary rocks and the crystalline nappe/klippe are well exposed (Figure 1) with dominating litho-units Lansdowne granite and granite gneiss. The proximity with thrust, resulted into deformation and transformation of Lansdowne granite to granite gneiss, further followed by augen gneiss and mylonite (Gupta, 1976a,b). The Bijni member rests over sedimentary rock of the Krol nappe and Garhwal thrust consisting quartz, schist and phyllite sequence (Auden, 1937). This phyllite is considered as Amri phyllite, correlated with Chandpur phyllite belonging to Chail nappe (Saklani, 1993). The Lansdowne formation tectonically overlies it and the Amri thrust marks the contact (Valdiya, 1980). Moreover, it has also been described as Lansdowne metamorphic (Gupta, 1976a, b) and Lansdowne crystallines (Valdiya, 1980). The Garhwal nappe comprises deformed phyllite and schist, capped by a small outcrop of Lansdowne granite and granite gneiss (Figure 2). The granite gneiss in the sequence changes from mylonitic gneiss at the base to granite gneiss in the upper sections (Gupta, 1976b). Additionally, there is evidence of granite intrusion above the metasediments in the Lansdowne area (Kumar and Daundhiyal, 1980). The Garhwal thrust is tectonically significant as it delineates major structural units in the lesser Himalaya that facilitated the emplacement of older Precambrian rocks over younger sedimentary sequences.

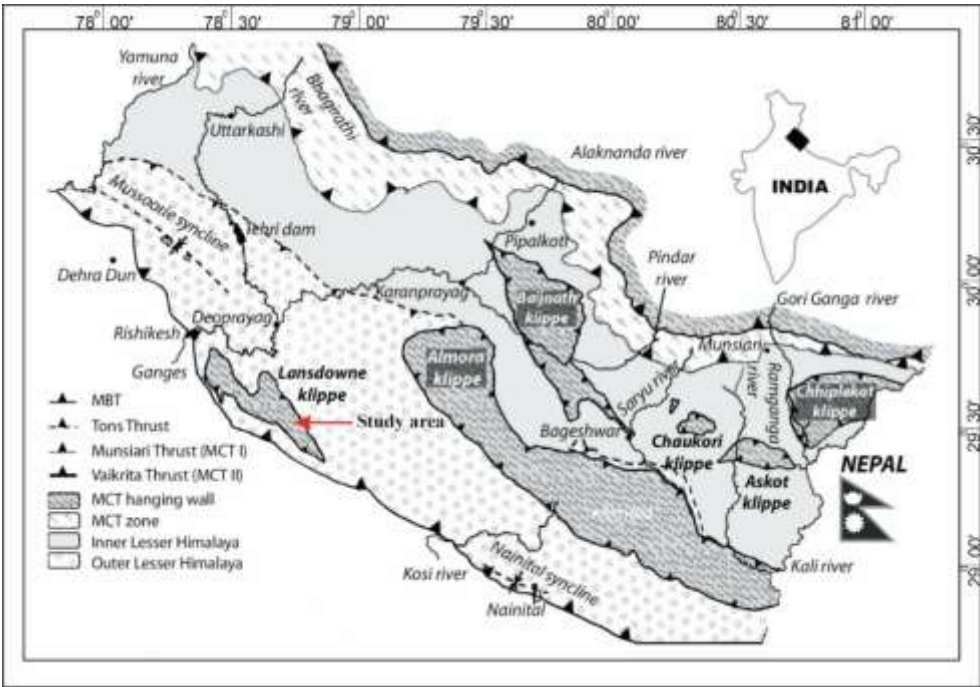


Figure 1. Geological and structural map of the Garhwal-Kumaun Lesser Himalaya (After Fuchs and Sinha, 1978).

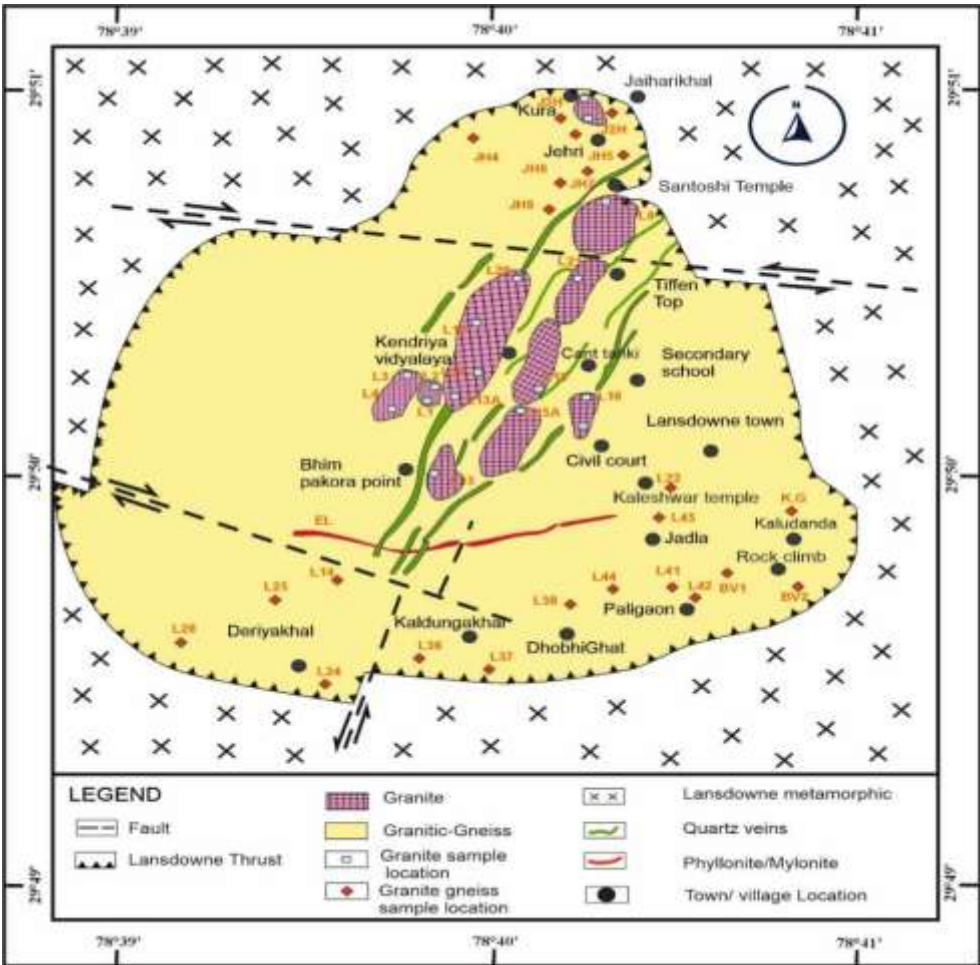


Figure 2. Geological map of the Lansdowne granite (LG) and Lansdowne granite gneiss (LGGn).



Figure 3. (A) Medium to coarse grained leucocratic granite pluton. (B) Melanocratic enclave within granite. (C) Granite gneiss showing minerals aligned parallel to the foliation plane. (D) Porphyroblast of feldspar showing augen structure.

The granite forms massive and small plutons. It is medium to coarse-grained, leucocratic, composed of K-feldspar, plagioclase, quartz, muscovite, and biotite, with accessory minerals such as tourmaline, apatite, epidote and zircon. It exhibits hypidiomorphic and porphyritic texture (Figure 3A). It also consists of microgranular enclaves of more or less elliptical shape (Figure 3B). The granitic gneiss exhibits tabular and euhedral feldspar phenocrysts that are aligned parallel to the foliation plane, exhibiting gneissose structure (Figure 3C). Phenocrysts of quartz and feldspars in granitic gneiss are surrounded by a thin mica layer that preserves their original characteristics (Figure 3D).

PETROGRAPHY

Petrographical study of granite and granite gneisses exhibits perthitic and porphyritic texture. Microcline exhibits crosshatch twinning. Sericitization is evident in plagioclase and quartz that show undulose extinction (Figure 4A). Plagioclase feldspar with inclusions of muscovite exhibits albitic twinning (Figure 4B). A single plagioclase crystal displays normal zoning with concentric zones of a calcic core and sodic rims (Figure 4C). Muscovite and biotite demonstrate perfect basal cleavage. Undulose quartz consists of tiny zircon inclusions (Figure 4D). Euhedral to subhedral

tourmaline exhibits two sets of cleavage (Figure 4E). K-feldspar with microcline exhibits cross-hatched or tartan twinning. Plagioclase and orthoclase exhibit carlsbad and albite twinning (Figure 4F)

Granite gneisses reveal that quartz and muscovite are aligned as parallel forming gneissic bands due to proximation along the compressional regime. Orthoclase feldspar with Carlsbad twinning exhibits inclusions of muscovite (Figure 5A). Quartz, muscovite, biotite, and K-feldspar crystals show preferred orientation along the foliation plane, exhibiting gneissose structure (Figure 5B). Deformed plagioclase porphyroblasts are aligned parallel to quartz and mica (Figure 5C). In post-deformational structures muscovite is surrounded by biotite, showing preferred orientation (Figure 5D). Deformed quartz wrapped in foliated mica ribbons display augen structure in gneisses (Figure 5E). Feldspar grains show a sigma structure with tails aligned parallel to the foliation plane, indicating shearing in NE-SW direction (Figure 5F). In the modal composition of the QAP diagram (Le Maitre, 2002), the proportions of quartz, alkali feldspar, and plagioclase feldspar falls within the granite field, specifically syeno-granite and monzo-granite (Figure 6)

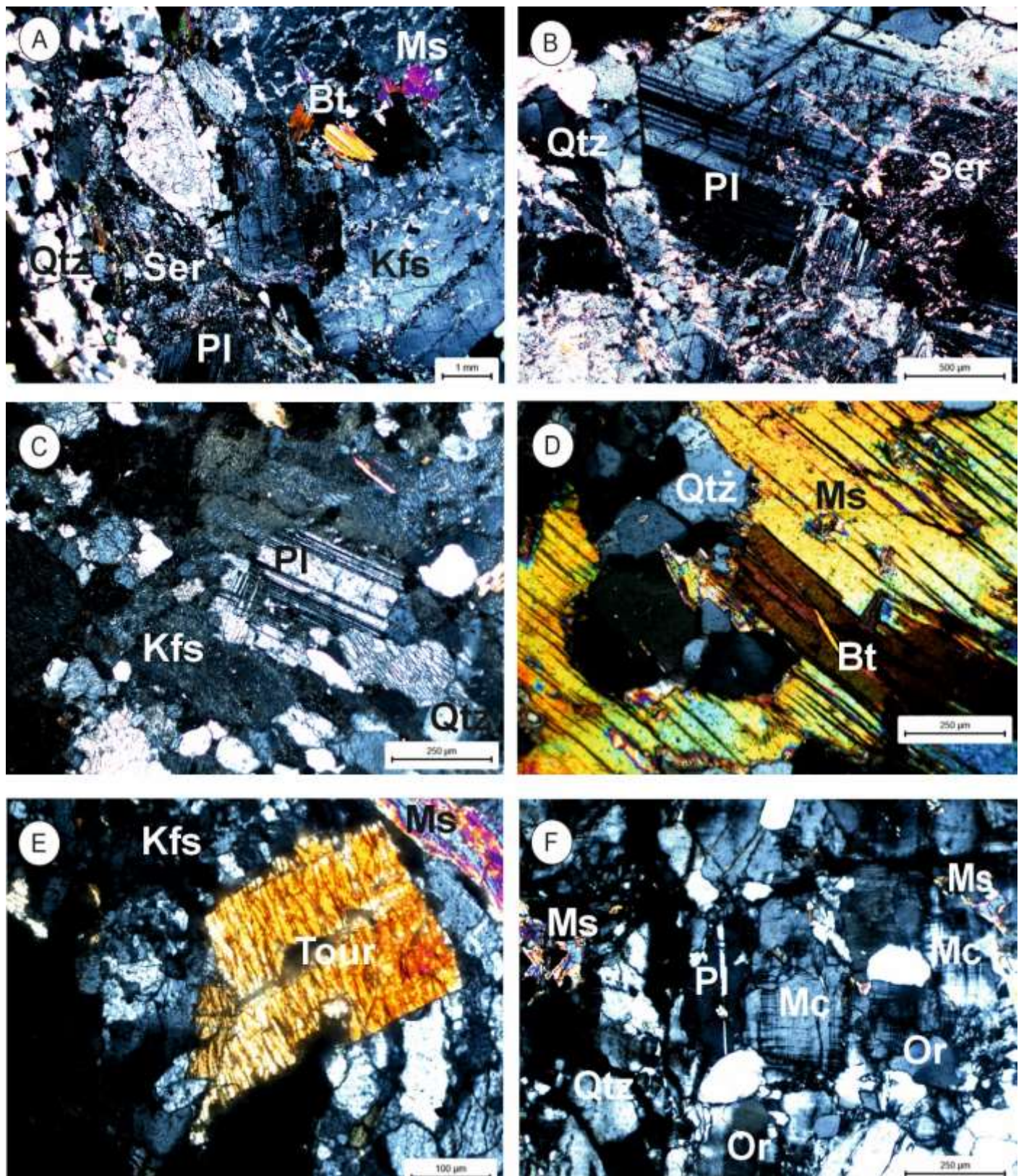


Figure 4. (A) Plagioclase and two mica inclusion in perthite. (B) Plagioclase phenocryst with sericitized muscovite inclusion. (C) Plagioclase normal zoning with sericitization. (D) Basal cleavage in two micas. (E) Euhedral tourmaline in K- feldspar. (F) Ovoid vacuoles in between feldspars. Qtz, Kfs, Pl, Bt, Ms, Mc, Tour, Ser and Or refer to quartz, K-feldspar, plagioclase, biotite, muscovite, microcline, tourmaline, sericitization and orthoclase respectively.

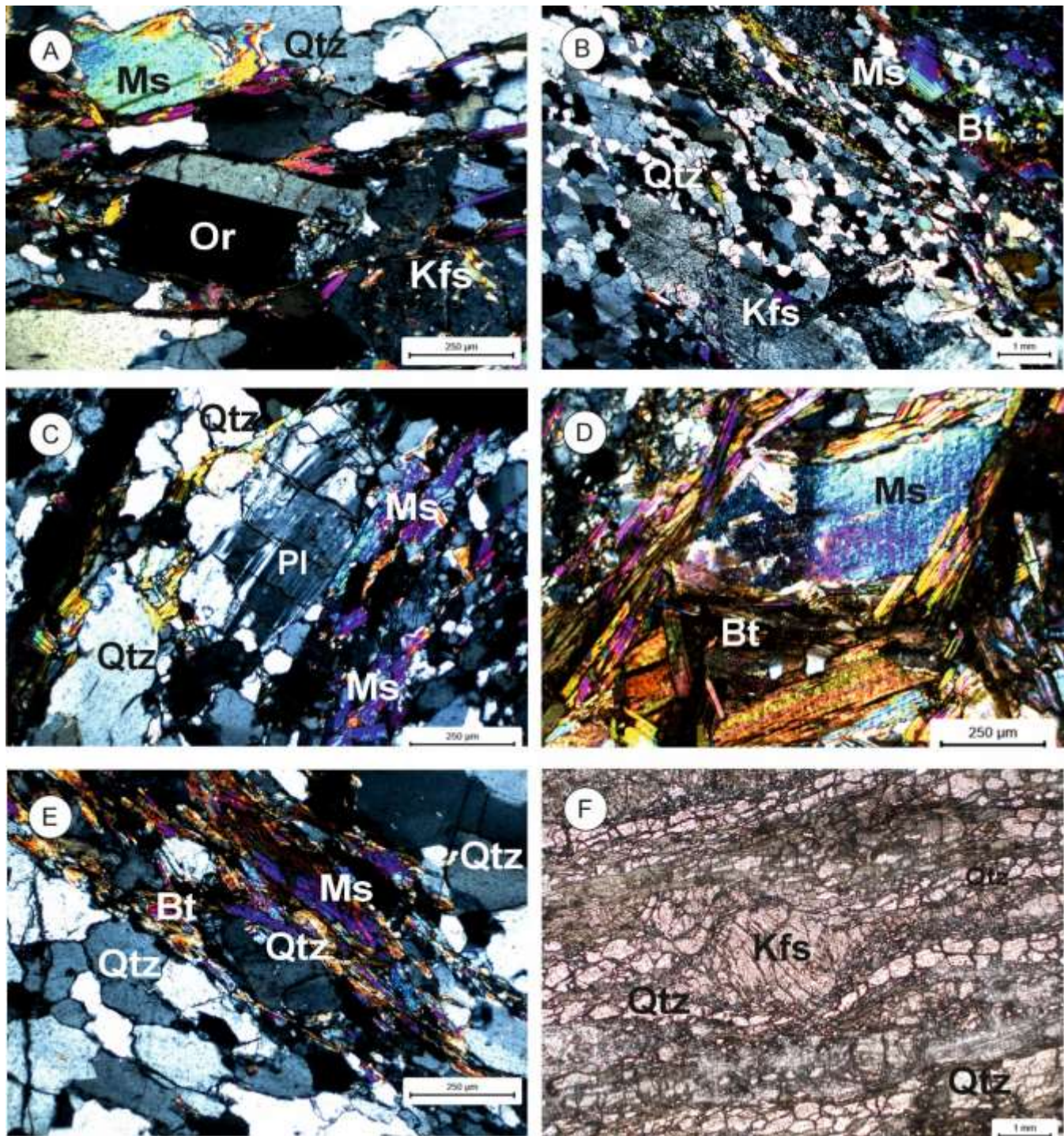


Figure 5. (A) Orthoclase, K-feldspar, and muscovite aligned along the foliation plane. (B) Alignment of minerals in parallel bands. (C) Plagioclase parallel to the foliation plane. (D) Biotite muscovite mica in deformed phase. (E) Quartz wrapped with mica foliation. (F) K-feldspar porphyroblast depicts sigma structure indicating shear sense. Qtz, Kfs, Pl, Bt, Ms, and Or refer to quartz, K-feldspar, plagioclase, biotite, muscovite, and orthoclase respectively.

RESULTS AND DISCUSSION

Whole rock geochemistry

Whole rock geochemical data (major and trace elements) on granite (N = 05) and granite gneiss (N = 05), as obtained from

XRF, is given in Table 1. Apparently, there is no major geochemical variation in the granite and granite gneisses. The granite shows limited variation in SiO₂ (69.47-70.19 wt.%), Al₂O₃ (16.76-17.18 wt.%) and K₂O (4.93-5.38 wt.%), and

substantially low range in Fe_2O_3 , CaO , MgO , P_2O_5 , MnO and TiO_2 (0.99-1.48 wt.%, 0.63-0.69 wt.%, 0.14-0.21 wt.%, 0.28-0.33 wt., 0.03-0.08 wt.% and 0.10-0.14 wt.% respectively). Similarly, the granite exhibits high variations in trace elements Ba, Rb, Cr (147-183 ppm, 364-395 ppm and 59-135 ppm respectively) and moderate variations in Sr, Zr, Pb, Zn, Ni, Ga, Y and Nb (54-69 ppm, 38-54 ppm, 38-59 ppm, 42-61 ppm, 13-16 ppm, 20-24 ppm, 34-37 ppm and 10-16 ppm) apart from considerably low contents in Co, Sc, V, Th, U and Cu (3-5 ppm, 1-3 ppm, 7-10 ppm, 4-7 ppm, 2.0-2.6 ppm and 8-12 ppm) contents

In comparison, the granite gneiss are characterised by SiO_2 (69.00-70.04 wt.%), Al_2O_3 (16.92-17.45 wt.%), moderately high values of Na_2O (3.94-4.47 wt.%) and K_2O (4.71-5.42 wt.%) and substantially lower values of Fe_2O_3 , CaO , MgO , P_2O_5 , MnO and TiO_2 (1.21-1.41 wt.%, 0.57-0.64 wt.%, 0.16-0.21 wt.%, 0.29-0.38 wt.%, 0.03-0.08 wt.% and 0.11-0.13 wt.% respectively). They exhibit high variations in trace elements Ba, Rb, Cr (109-205 ppm, 379-463 ppm and 21-158 ppm respectively) and moderate variations in Sr, Zr, Pb, Zn, Ni, Ga, Y and Nb (46-67 ppm, 44-51 ppm, 36-53 ppm, 54-61 ppm, 15-

19 ppm, 24-27 ppm, 35-41 ppm and 14-17 ppm respectively). They further show low contents in Co, Sc, V, Th, U and Cu (3-7 ppm, 1-3 ppm, 4-9 ppm, 5-7 ppm, 2.0-2.5 ppm and 4-13 ppm respectively) (Arya, 2024).

Mineral chemistry, composition, and classification of feldspar

K-feldspar

The general formula of feldspar is XZ_4O_8 (where X = Ca, Na, K, and Z = Si, Al). The feldspar group of end members are $\text{NaAlSi}_3\text{O}_8$ (albite, Ab), KAlSi_3O_8 (orthoclase, Or), and $\text{CaAl}_2\text{Si}_2\text{O}_8$ (anorthite, An). Micro probe analysis data and calculated structural formulas for feldspar group of minerals are provided in Tables 2-9.

Compositions of K-feldspars in granite vary in a narrow range (Ab=2.57-7.15, Or=92.55-95.87, An=0.00-0.001), except few samples. The K-feldspar in granite gneiss reveals almost similar composition to granite (Ab=4.43-6.64, Or=92.86-99.60, An=0.00). The K-feldspar from both litho-units is equal to sanidine composition (Figure 7A).

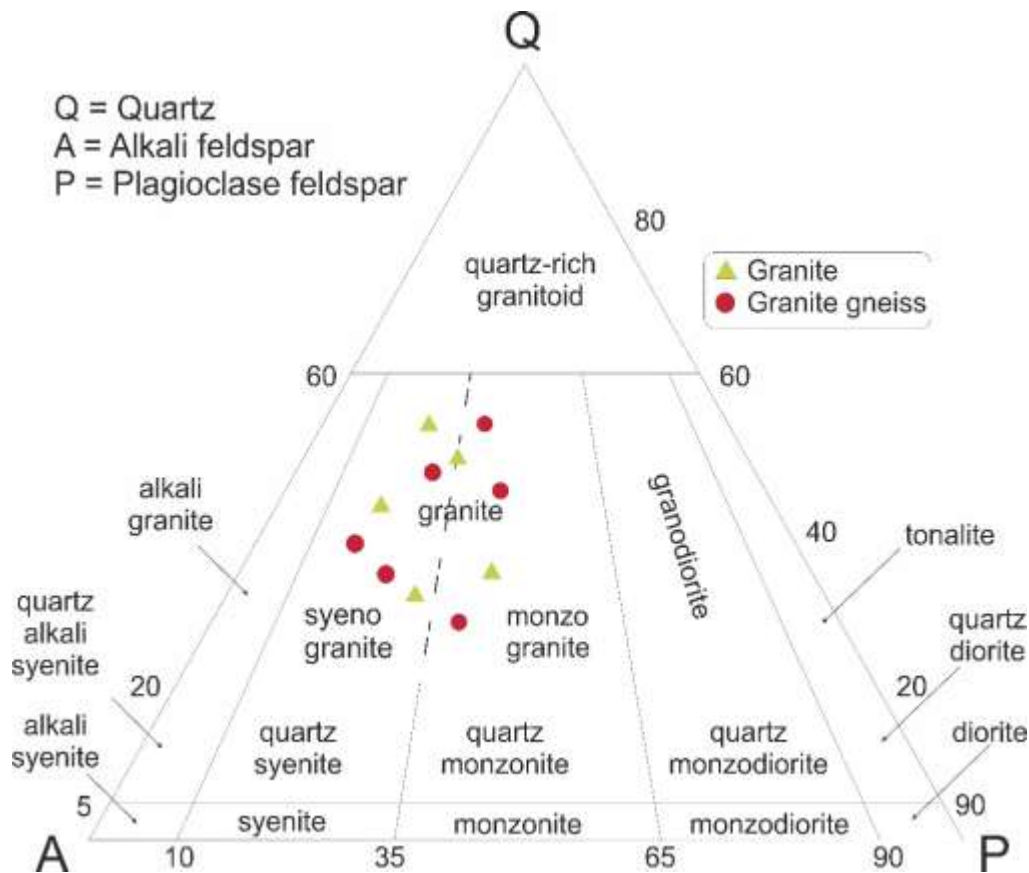


Figure 6. Modal composition of the Lansdowne granite and granite gneiss rocks plotted in the QAP diagram. Granite reveals two fields syenogranite and monzogranite (after Le Maitre, 2002).

Table 1. Major oxides (wt.%), trace, and rare earth elemental composition (in ppm) of Lansdowne granite (LG) and Lansdowne granite gneiss (LGGn) samples from Garhwal Lesser Himalaya.

Sample No.	L13 (LG)	L16 (LG)	L19 (LG)	L21 (LG)	L45 (LG)	JH1 (LGGn)	BV1 (LGGn)	L6 (LGGn)	L23 (LGGn)	L35 (LGGn)
SiO ₂	69.5	70.19	69.47	70.15	69.79	70.04	69.47	69	69.28	68.99
TiO ₂	0.12	0.1	0.13	0.14	0.12	0.11	0.13	0.12	0.12	0.12
Al ₂ O ₃	17.18	16.98	16.98	16.76	16.96	16.92	17.07	17.34	17.45	17.22
Fe ₂ O ₃	1.27	0.99	1.38	1.48	1.31	1.21	1.41	1.32	1.28	1.33
MnO	0.03	0.03	0.03	0.03	0.03	0.03	0.03	0.03	0.03	0.04
MgO	0.19	0.14	0.2	0.21	0.18	0.16	0.21	0.18	0.18	0.19
CaO	0.69	0.63	0.65	0.63	0.63	0.61	0.64	0.61	0.57	0.61
Na ₂ O	4.17	4.32	3.81	3.82	4.28	4.47	3.94	3.99	3.96	4.12
K ₂ O	5.15	5.38	5.02	5.18	4.93	4.71	4.96	4.94	5.42	4.8
P ₂ O ₅	0.33	0.28	0.33	0.33	0.32	0.38	0.32	0.34	0.29	0.34
LOI	1.48	1.46	1.6	1.65	1.35	1.49	1.65	1.92	2.05	1.66
TOTAL	98.63	99.04	98	98.73	98.55	98.64	98.18	97.87	98.58	97.76
Ba	167	171	178	183	147	109	160	159	205	140
Rb	365	364	368	377	395	463	388	401	379	393
Sr	69	68	61	63	54	46	59	55	67	50
Y	35	34	35	36	37	41	37	38	35	37
Zr	50	38	51	54	49	44	51	51	46	48
Nb	14	10	15	16	16	17	16	17	14	16
Cr	135	59	89	94	60	26	21	23	158	55
Ni	13	16	14	15	16	17	16	16	15	19
Co	5	3	5	3	4	6	3	3	7	7
Sc	2	2	3	1	2	2.3	1.4	1.2	3	2.7
V	9	7	8	10	7	7	9	8	4	8
Cu	8	12	9	8	8	4	10	9	10	13
Pb	48	59	42	42	38	36	44	41	53	36
Zn	52	42	57	61	60	59	61	58	54	59
Ga	23	20	22	22	24	27	26	26	24	25
Th	6	4	7	7	6	6	7	7	5	5
U	2.3	2	2.3	2.6	2.5	2.5	2	2.4	2.3	2.1
La	13.72	7.58	9.69	13.72	11.32	9.33	13.91	17.27	8	12.22
Ce	27.53	16.13	22.4	30.06	24.82	16.98	31.43	36.71	15.35	27.61
Pr	3.18	1.71	2.26	3.24	2.71	2.26	3.31	4.05	1.85	2.97
Nd	10.49	5.87	7.85	10.81	9.21	7.11	11.5	13.6	5.97	10.02
Sm	2.98	1.52	2.19	3.15	2.6	2.25	3.21	3.8	1.67	2.74
Eu	0.56	0.46	0.38	0.47	0.33	0.28	0.44	0.52	0.4	0.39
Gd	2.84	1.5	2.22	3.19	2.48	2.11	3.08	3.61	1.62	2.72
Tb	0.49	0.25	0.4	0.55	0.41	0.38	0.53	0.61	0.29	0.47
Dy	2.43	1.27	1.93	2.6	1.93	1.82	2.56	3.02	1.45	2.28
Ho	0.3	0.16	0.24	0.31	0.25	0.22	0.31	0.36	0.18	0.28
Er	0.7	0.35	0.58	0.71	0.53	0.5	0.73	0.83	0.46	0.64
Tm	0.08	0.04	0.07	0.08	0.07	0.07	0.08	0.1	0.05	0.08
Yb	0.5	0.26	0.4	0.52	0.42	0.38	0.52	0.57	0.32	0.5
Lu	0.07	0.04	0.05	0.07	0.05	0.05	0.07	0.08	0.04	0.07

Table 2. Microprobe analysis of K-feldspar (K-Fsp) from the Lansdowne granite sample L16, Garhwal Lesser Himalaya. Oxides are in wt%.

Lansdowne Granite																		
Sample No.	L16	L16	L16	L16	L16	L16	L16	L16	L16	L16	L16	L16	L16	L16	L16	L16	L16	L16
Mineral	K-Fsp	K-Fsp	K-Fsp	K-Fsp	K-Fsp	K-Fsp	K-Fsp	K-Fsp	K-Fsp	K-Fsp	K-Fsp	K-Fsp	K-Fsp	K-Fsp	K-Fsp	K-Fsp	K-Fsp	K-Fsp
SiO ₂	63.7	63.16	64.24	63.36	63.96	63.93	63.98	64.42	63.92	63.85	63.43	63.57	65.07	63.62	63.63	63.99	63.29	63.30
TiO ₂	0.035	0.011	0.03	0	0	0.03	0	0.021	0.009	0.015	0.017	0.004	0	0	0.003	0.006	0.032	0
Al ₂ O ₃	18.01	18.46	18.29	18.74	18.49	18.63	18.27	18.44	17.74	18.32	17.81	17.79	18.13	17.94	17.74	17.77	17.81	18.02
FeO	0.058	0.095	0	0	0.168	0	0.036	0	0	0	0.013	0.003	0.074	0.076	0.001	0.073	0	0
CaO	0.095	0	0	0.003	0	0	0	0.064	0.213	0	0	0.021	0.25	0.036	0.03	0.032	0.04	0.032
Na ₂ O	0.277	0.553	0.689	0.663	0.583	0.632	0.724	0.709	0.713	0.798	0.564	0.399	4.239	0.337	0.327	0.562	0.324	0.676
K ₂ O	15.89	16.05	16.03	15.96	16.61	16.07	15.91	16.11	15.68	15.82	16.34	16.77	11.35	16.26	16.72	16.31	16.72	16.02
P ₂ O ₅	0.319	0.526	0.26	0.744	0.247	0.331	0.336	0.336	0.433	0.255	0.345	0.165	0	0.164	0.014	0	0.223	0.283
TOTAL	98.39	98.87	99.55	99.48	100.0	99.64	99.27	100.1	98.73	99.07	98.54	98.73	99.12	98.44	98.48	98.76	98.45	98.34
Tot. oxy	8	8	8	8	8	8	8	8	8	8	8	8	8	8	8	8	8	8
Cation																		
Si	11.77	11.67	11.87	11.71	11.82	11.82	11.83	11.91	11.81	11.80	11.72	11.75	12.03	11.76	11.76	11.83	11.70	11.70
Ti	0.005	0.001	0.004	0	0	0.004	0	0.003	0.001	0.002	0.002	0	0	0	0	0.001	0.005	0
Al	3.925	4.023	3.986	4.085	4.03	4.061	3.983	4.018	3.867	3.993	3.882	3.878	3.951	3.91	3.867	3.873	3.882	3.927
Fe	0.009	0.015	0	0	0.026	0	0.006	0	0	0	0.002	0	0.011	0.012	0	0.011	0	0
Ca	0.019	0	0	0.001	0	0	0	0.013	0.042	0	0	0.004	0.049	0.007	0.006	0.006	0.008	0.006
Na	0.099	0.198	0.247	0.237	0.209	0.226	0.259	0.254	0.256	0.286	0.202	0.143	1.52	0.121	0.117	0.201	0.116	0.242
K	3.749	3.787	3.781	3.764	3.919	3.791	3.754	3.801	3.7	3.733	3.855	3.956	2.678	3.837	3.944	3.848	3.943	3.779
Ba	0.025	0.041	0.02	0.058	0.019	0.026	0.026	0.026	0.034	0.02	0.027	0.013	0	0.013	0.001	0	0.017	0.022
TOTAL	19.60	19.74	19.91	19.86	20.02	19.92	19.85	20.02	19.71	19.84	19.7	19.74	20.24	19.66	19.70	19.77	19.67	19.68
An	0	0	0	0	0	0	0	0	0	0	0	0	0	0	0	0	0	0
Ab	2.571	4.969	6.133	5.933	5.063	5.636	6.465	6.244	6.395	7.115	4.982	3.484	35.78	3.042	2.878	4.964	2.859	6.017
Or	96.94	95.03	93.86	94.05	94.93	94.36	93.53	93.44	92.55	92.88	95.01	96.41	63.05	96.77	96.97	94.87	96.94	93.82

Table 3. Microprobe analysis of K-feldspar (K-Fsp) from the Lansdowne granite sample L21, Garhwal Lesser Himalaya. Oxides are in wt%.

Lansdowne Granite														
Sample No.	L21	L21	L21	L21	L21	L21	L21	L21	L21	L21	L21	L21	L21	L21
Mineral	K-Fsp	K-Fsp	K-Fsp	K-Fsp	K-Fsp	K-Fsp	K-Fsp	K-Fsp	K-Fsp	K-Fsp	K-Fsp	K-Fsp	K-Fsp	K-Fsp
SiO ₂	63.066	64.286	63.62	63.639	63.304	63.066	63.57	65.077	64.628	65.016	63.924	63.397	63.711	64.037
TiO ₂	0	0.006	0	0.003	0	0	0.004	0	0	0.002	0.021	0.022	0	0.021
Al ₂ O ₃	17.945	17.946	17.945	17.748	18.025	17.945	17.797	18.132	17.946	18.065	17.918	17.889	18.072	17.817
FeO	0	0.031	0.076	0.001	0	0	0.003	0.074	0.017	0	0	0.015	0.043	0.058
CaO	0.036	0.02	0.036	0.03	0.032	0.036	0.021	0.25	1.537	0.027	0	0	0.1	0.005
Na ₂ O	0.313	0.658	0.337	0.327	0.676	0.313	0.399	4.239	7.539	0.318	0.318	0.581	0.076	0.099
K ₂ O	16.475	15.944	16.269	16.723	16.024	16.475	16.774	11.354	6.183	15.79	16.715	16.184	15.825	16.273
P ₂ O ₅	0.136	0.001	0.164	0.014	0.283	0.136	0.165	0	1.437	0.007	0	0.02	0.193	0.01
TOTAL	97.97	98.89	98.445	98.483	98.343	97.97	98.732	99.126	99.287	99.223	98.895	98.109	98.02	98.32
Tot. oxy	8	8	8	8	8	8	8	8	8	8	8	8	8	8
Cation														
Si	11.66	11.885	11.762	11.766	11.704	11.66	11.753	12.032	11.949	12.02	11.818	11.721	11.779	11.839
Ti	0	0.001	0	0	0	0	0	0	0	0	0.003	0.003	0	0.003
Al	3.91	3.91	3.91	3.867	3.927	3.91	3.878	3.951	3.91	3.936	3.904	3.898	3.938	3.882
Fe	0	0.005	0.012	0	0	0	0	0.011	0.003	0	0	0.002	0.007	0.009
Ca	0.007	0.004	0.007	0.006	0.006	0.007	0.004	0.049	0.304	0.005	0	0	0.02	0.001
Na	0.112	0.236	0.121	0.117	0.242	0.112	0.143	1.52	2.702	0.114	0.114	0.208	0.027	0.035
K	3.885	3.76	3.837	3.944	3.779	3.885	3.956	2.678	1.458	3.724	3.942	3.817	3.732	3.838
Ba	0.011	0	0.013	0.001	0.022	0.011	0.013	0	0.112	0.001	0	0.002	0.015	0.001
TOTAL	19.585	19.801	19.661	19.701	19.681	19.585	19.748	20.241	20.439	19.8	19.781	19.651	19.518	19.608
An	0	0	0	0	0	0	0	0	0.001	0	0	0	0	0
Ab	2.799	5.899	3.042	2.878	6.017	2.799	3.484	35.781	60.521	2.961	2.806	5.176	0.721	0.914
Or	97.024	94.004	96.777	96.978	93.826	97.024	96.416	63.054	32.659	96.901	97.194	94.824	98.755	99.059

Table 4. Microprobe analysis of K-feldspar (K-Fsp) from the Lansdowne granite gneiss samples L 42 and L44, Garhwal Lesser Himalaya. Oxides are in wt%.

Sample No.	Lansdowne Granite Gneiss									
	L42	L42	L42	L42	L42	L44	L44	L44	L44	L44
Mineral	K-Fsp	K-Fsp	K-Fsp	K-Fsp	K-Fsp	K-Fsp	K-Fsp	K-Fsp	K-Fsp	K-Fsp
SiO ₂	63.304	63.066	63.57	65.077	64.628	65.016	63.924	63.397	63.711	64.037
TiO ₂	0	0	0.004	0	0	0.002	0.021	0.022	0	0.021
Al ₂ O ₃	18.025	17.945	17.797	18.132	17.946	18.065	17.918	17.889	18.072	17.817
FeO	0	0	0.003	0.074	0.017	0	0	0.015	0.043	0.058
CaO	0.032	0.036	0.021	0.25	1.537	0.027	0	0	0.1	0.005
Na ₂ O	0.676	0.313	0.399	4.239	7.539	0.318	0.318	0.581	0.076	0.099
K ₂ O	16.024	16.475	16.774	11.354	6.183	15.79	16.715	16.184	15.825	16.273
P ₂ O ₅	0.283	0.136	0.165	0	1.437	0.007	0	0.02	0.193	0.01
TOTAL	98.343	97.97	98.732	99.126	99.287	99.223	98.895	98.109	98.02	98.32
Tot.oxy	8	8	8	8	8	8	8	8	8	8
Cation										
Si	11.704	11.66	11.753	12.032	11.949	12.02	11.818	11.721	11.779	11.839
Ti	0	0	0	0	0	0	0.003	0.003	0	0.003
Al	3.927	3.91	3.878	3.951	3.91	3.936	3.904	3.898	3.938	3.882
Fe	0	0	0	0.011	0.003	0	0	0.002	0.007	0.009
Ca	0.006	0.007	0.004	0.049	0.304	0.005	0	0	0.02	0.001
Na	0.242	0.112	0.143	1.52	2.702	0.114	0.114	0.208	0.027	0.035
K	3.779	3.885	3.956	2.678	1.458	3.724	3.942	3.817	3.732	3.838
Ba	0.022	0.011	0.013	0	0.112	0.001	0	0.002	0.015	0.001
TOTAL	19.681	19.585	19.748	20.241	20.439	19.8	19.781	19.651	19.518	19.608
An	0	0	0	0	0.001	0	0	0	0	0
Ab	6.017	2.799	3.484	35.781	60.521	2.961	2.806	5.176	0.721	0.914
Or	93.826	97.024	96.416	63.054	32.659	96.901	97.194	94.824	98.755	99.059

Table 5. Microprobe analysis of plagioclase (Plag) from the Lansdowne granite sample L27, Garhwal Lesser Himalaya. Oxides are in wt%.

Sample No.	Lansdowne Granite											
	L27	L27	L27	L27	L27	L27	L27	L27	L27	L27	L27	L27
Mineral	Plag	Plag	Plag	Plag	Plag	Plag	Plag	Plag	Plag	Plag	Plag	Plag
SiO ₂	66.65	66.35	64.16	63.53	63.96	67.25	68.18	66.22	63.87	63.94	65.71	64.48
TiO ₂	0.02	0	0	0	0	0	0	0	0	0	0	0
Al ₂ O ₃	19.47	20	21.18	21.18	21.79	19.37	19.65	19.77	19.73	20.11	20.07	18.34
FeO	0	0	0	0	0	0.04	0.03	0	0	0	0	0
CaO	0.65	1.36	2.69	2.88	3.21	0.79	0.3	1.36	1.55	1.79	1.43	2.62
Na ₂ O	10.95	11.26	10.44	10.51	10.34	11.43	11.64	11.33	11.28	10.95	11.31	11.38
K ₂ O	0.17	0	0.08	0.05	0.13	0.12	0.09	0.04	0.02	0.05	0.08	0.15
P ₂ O ₅	0.3	0.14	0.28	0.25	0.3	0.01	0.27	0.22	0.23	0.26	0	2.3
TOTAL	98.22	99.11	98.84	98.4	99.74	99.02	100.16	98.94	96.67	97.09	98.6	99.29
Tot.oxy	8	8	8	8	8	8	8	8	8	8	8	8
Cation												
Si	12.186	12.13	11.73	11.615	11.693	12.296	12.465	12.106	11.676	11.69	12.013	11.789
Ti	0.003	0	0	0	0	0	0.001	0	0	0	0	0
Al	4.196	4.309	4.563	4.563	4.696	4.172	4.234	4.259	4.25	4.334	4.324	3.952
Fe	0	0	0	0	0	0.007	0.004	0	0	0	0	0
Ca	0.127	0.266	0.527	0.564	0.629	0.155	0.058	0.267	0.303	0.35	0.281	0.514
Na	3.88	3.991	3.7	3.726	3.666	4.051	4.127	4.016	3.997	3.88	4.01	4.035
K	0.041	0	0.019	0.012	0.03	0.027	0.021	0.008	0.004	0.011	0.018	0.035
P	0.023	0.011	0.022	0.019	0.023	0.001	0.021	0.017	0.018	0.02	0	0.178
TOTAL	20.43	20.7	20.54	20.48	20.71	20.71	20.91	20.66	20.23	20.26	20.64	20.32
An	3.14	6.26	12.42	13.11	14.55	3.67	1.38	6.23	7.04	8.26	6.52	11.21
Ab	95.86	93.74	87.13	86.61	84.75	95.69	98.13	93.58	92.87	91.49	93.06	88.03
Or	1	0	0.45	0.29	0.7	0.64	0.49	0.19	0.1	0.25	0.42	0.75

Table 6. Microprobe analysis of plagioclase (Plag) from the Lansdowne granite sample L13, Garhwal Lesser Himalaya. Oxides are in wt%.

Sample No.	Lansdowne Granite											
	L13	L13	L13	L13	L13	L13	L13	L13	L13	L13	L13	L13
Mineral	Plag	Plag	Plag	Plag	Plag	Plag	Plag	Plag	Plag	Plag	Plag	Plag
SiO ₂	63.9	64.29	63.96	68.17	67.9	68.39	66.87	68.39	68.99	67.81	67.58	67.74
TiO ₂	0.03	0.05	0.03	0.05	0	0	0	0	0	0	0.01	0
Al ₂ O ₃	20.94	21.42	20.91	19.83	18.92	18.64	18.82	18.64	19.02	19.19	19.21	19.03
FeO	0.16	0.01	0.11	0	0.03	0.05	0.12	0.05	0.03	0.13	0.03	0
CaO	2.87	2.87	2.86	0.51	0.01	0.01	0.57	0.01	0.12	0	0.05	0.15
Na ₂ O	9.7	10.28	10.29	10.85	11.85	10.78	11.94	10.78	11.41	12.01	11.47	11.25
K ₂ O	0.24	0.28	0.19	0.08	0.14	1.62	0.09	1.62	0.14	0.11	0.18	0.08
P ₂ O ₅	0.3	0.25	0.32	0.57	0.01	0.09	0.13	0.09	0	0	0	0.02
TOTAL	98.14	99.45	98.68	100.06	98.85	99.58	98.54	99.58	99.71	99.25	98.51	98.27
Tot.oxy	8	8	8	8	8	8	8	8	8	8	8	8
Cation												
Si	11.683	11.754	11.693	12.463	12.414	12.504	12.225	12.504	12.613	12.397	12.354	12.385
Ti	0.004	0.007	0.005	0.007	0	0	0	0	0	0	0.001	0
Al	4.512	4.615	4.505	4.272	4.076	4.016	4.055	4.016	4.098	4.134	4.138	4.1
Fe	0.024	0.002	0.017	0	0.004	0.007	0.018	0.007	0.005	0.02	0.004	0
Ca	0.562	0.562	0.56	0.099	0.001	0.003	0.112	0.003	0.024	0	0.009	0.029
Na	3.438	3.643	3.647	3.844	4.199	3.82	4.232	3.82	4.043	4.256	4.064	3.986
K	0.055	0.064	0.045	0.02	0.032	0.377	0.021	0.377	0.033	0.026	0.042	0.019
P	0.023	0.019	0.025	0.044	0.001	0.007	0.01	0.007	0	0	0	0.002
TOTAL	20.28	20.65	20.47	20.71	20.73	20.73	20.66	20.73	20.82	20.83	20.61	20.52
An	13.85	13.17	13.17	2.51	0.02	0.06	2.57	0.06	0.58	0	0.23	0.73
Ab	84.79	85.32	85.76	97	99.21	90.95	96.95	90.95	98.61	99.4	98.76	98.81
Or	1.36	1.51	1.06	0.5	0.77	8.99	0.48	8.99	0.81	0.6	1.01	0.46

Table 7. Microprobe analysis of plagioclase (Plag) from the Lansdowne granite sample L20, Garhwal Lesser Himalaya. Oxides are in wt%.

Sample No.	Lansdowne Granite											
	L20	L20	L20	L20	L20	L20	L20	L20	L20	L20	L20	L20
Mineral	Plag	Plag	Plag	Plag	Plag	Plag	Plag	Plag	Plag	Plag	Plag	Plag
SiO ₂	68.07	67.54	68.01	68.43	68.73	67.37	67.96	68.08	68.14	66.96	67.75	68.99
TiO ₂	0	0	0	0	0	0	0	0	0	0	0	0
Al ₂ O ₃	19.19	19.24	19.03	19.31	19.53	19.47	18.86	18.86	18.85	18.97	18.76	19.02
FeO	0.18	0.07	0	0	0.07	0.07	0	0	0	0.07	0.06	0.03
CaO	0.07	0.19	0	0.12	0	0	0.1	0.09	0.15	0.23	0.14	0.12
Na ₂ O	11.77	11.35	11.79	10.99	11.65	11.83	11.42	11.62	11.4	11.57	11.71	11.41
K ₂ O	0.11	0.12	0.06	0.07	0.1	0.25	0.15	0.15	0.13	0.18	0.11	0.14
P ₂ O ₅	0.02	0.03	0	0	0	0	0.01	0	0	0.03	0.03	0
TOTAL	99.4	98.54	98.89	98.92	100.09	98.98	98.5	98.8	98.68	98.02	98.56	99.71
Tot.oxy	8	8	8	8	8	8	8	8	8	8	8	8
Cation												
Si	12.445	12.348	12.434	12.511	12.565	12.316	12.425	12.446	12.457	12.241	12.387	12.613
Ti	0	0	0	0	0	0	0	0	0	0	0	0
Al	4.134	4.146	4.099	4.16	4.209	4.195	4.064	4.063	4.061	4.088	4.043	4.098
Fe	0.027	0.011	0	0	0.011	0.011	0	0	0	0.011	0.009	0.005
Ca	0.013	0.037	0	0.024	0	0	0.019	0.018	0.03	0.045	0.027	0.024
Na	4.173	4.024	4.179	3.894	4.128	4.192	4.048	4.118	4.042	4.102	4.149	4.043
K	0.024	0.027	0.014	0.017	0.023	0.058	0.035	0.034	0.031	0.042	0.026	0.033
P	0.002	0.002	0	0	0	0	0.001	0	0	0.002	0.002	0
TOTAL	20.82	20.59	20.73	20.61	20.94	20.77	20.59	20.68	20.62	20.53	20.64	20.82
An	0.32	0.89	0	0.6	0	0	0.46	0.44	0.73	1.08	0.64	0.58
Ab	99.1	98.43	99.67	98.97	99.45	98.65	98.68	98.74	98.51	97.91	98.75	98.61
Or	0.58	0.67	0.33	0.42	0.55	1.35	0.86	0.82	0.76	1	0.61	0.81

Table 8. Microprobe analysis of plagioclase (Plag) from the Lansdowne granite gneiss sample BV1, Garhwal Lesser Himalaya. Oxides are in wt%.

Sample No.	Lansdowne Granite Gneiss																	
Mineral	Plag	Plag	Plag	Plag	Plag	Plag	Plag	Plag	Plag	Plag	Plag	Plag	Plag	Plag	Plag	Plag	Plag	Plag
SiO ₂	67.17	66.92	68.48	66.85	68.3	66.97	66.97	67.97	68.88	67.49	67.21	66.01	66.57	67.49	65.61	65.57	65.44	65.93
TiO ₂	0	0	0.01	0.04	0.01	0	0.01	0	0	0.01	0.01	0	0.01	0.01	0	0	0	0
Al ₂ O ₃	19.9	19.66	19.83	20.06	19.64	20.26	19.02	19.8	19.39	19.82	20.47	20.94	20.78	20.12	21.24	20.23	20.63	18.71
FeO	0	0	0	0	0	0	0	0	0	0	0	0	0.1	0	0	0	0.01	0
CaO	0.34	0.45	0.12	1.06	0.13	0.89	0.1	0.16	0.01	0.44	0.96	1.2	1.19	0.67	1.94	1.22	1.47	1.2
Na ₂ O	11.82	11.02	11.74	10.69	11.41	11.4	7.29	11.68	11.69	11.64	11.08	10.95	11.05	11.33	10.78	11.24	11.14	11.9
K ₂ O	0.11	1.4	0.11	0.09	0.13	0.05	6.34	0.08	0.13	0.13	0.12	0.19	0.13	0.09	0.1	0.14	0.08	0.01
P ₂ O ₅	0.14	0.16	0	0.5	0	0.39	0	0	0	0.02	0.29	0.53	0.6	0.18	0.2	0.5	0.54	1.24
TOTAL	99.49	99.62	100.2	99.29	99.61	99.96	99.74	99.68	100.1	99.56	100.1	99.83	100.4	99.9	99.87	98.9	99.32	98.99
Tot.ox	8	8	8	8	8	8	8	8	8	8	8	8	8	8	8	8	8	8
Cation																		
Si	12.28	12.23	12.52	12.22	12.48	12.24	12.24	12.42	12.59	12.33	12.28	12.06	12.17	12.33	11.99	11.98	11.96	12.05
Ti	1	5		1	6	4	4	6	3	9	7	9	1	9	6	7	4	3
Al	4.288	4.236	4.272	4.323	4.231	4.365	4.098	4.265	4.178	4.271	4.41	4.512	4.478	4.335	4.575	4.358	4.444	4.031
Fe	0	0	0	0	0	0	0	0	0	0	0	0	0.016	0	0	0	0.002	0
Ca	0.067	0.089	0.024	0.208	0.026	0.174	0.02	0.031	0.001	0.086	0.189	0.236	0.233	0.132	0.379	0.24	0.289	0.235
Na	4.191	3.907	4.16	3.788	4.043	4.04	2.583	4.139	4.144	4.126	3.926	3.881	3.918	4.015	3.822	3.984	3.949	4.217
K	0.025	0.325	0.025	0.02	0.03	0.012	1.48	0.018	0.03	0.031	0.028	0.043	0.031	0.022	0.023	0.033	0.019	0.002
Ba	0.011	0.012	0	0.039	0	0.03	0	0	0	0.002	0.023	0.041	0.046	0.014	0.016	0.039	0.042	0.096
TOTAL	20.85	20.79	21	20.57	20.82	20.84	20.43	20.88	20.95	20.85	20.84	20.74	20.85	20.84	20.8	20.6	20.67	20.54
An	1.57	2.06	0.57	5.19	0.64	4.13	0.5	0.75	0.02	2.03	4.55	5.67	5.57	3.16	8.98	5.63	6.78	5.28
Ab	97.84	90.41	98.84	94.31	98.62	95.59	63.26	98.81	99.26	97.24	94.77	93.29	93.68	96.32	90.48	93.58	92.78	94.67
Or	0.59	7.53	0.59	0.5	0.73	0.28	36.24	0.44	0.72	0.73	0.68	1.04	0.74	0.52	0.54	0.79	0.44	0.06

Table 9. Microprobe analysis of plagioclase (Plag) from the Lansdowne granite gneiss sample JH2, Garhwal Lesser Himalaya. Oxides are in wt%.

Sample No.	Lansdowne Granite Gneiss																	
Mineral	Plag	Plag	Plag	Plag	Plag	Plag	Plag	Plag	Plag	Plag	Plag	Plag	Plag	Plag	Plag	Plag	Plag	Plag
SiO ₂	66.43	66.78	66.55	66.09	65.83	68.67	66.5	66.56	66.32	63.73	65.3	67.18	63.48	64.77	63.93	66.64	65.44	65.71
TiO ₂	0	0	0	0	0	0	0	0	0	0	0	0	0	0	0	0.01	0.01	0
Al ₂ O ₃	19.21	19	19.09	19.38	19.5	19.37	19.4	19.36	19.47	21.56	20.2	19.39	21.55	20.86	21.79	19.91	19.8	19.96
FeO	0	0	0	0	0	0	0	0	0	0	0.09	0	0	0.12	0	0.09	0.24	0.18
CaO	1.26	0.72	0.88	1.23	1.48	0.42	0.94	0.57	0.82	2.87	1.73	0.78	2.93	1.92	3.03	1.11	0.5	0.52
Na ₂ O	11.26	11.59	11.65	11.79	11.42	11.2	11	11.7	11.38	9.78	10.9	11.09	10.23	10.74	10.33	11.17	11.41	10.79
K ₂ O	0.03	0.03	0.04	0.02	0.06	0.08	0.15	0.03	0.04	0.19	0.14	0.15	0.19	0.21	0.2	0.12	0.88	2.12
P ₂ O ₅	0	0.4	0.14	0.14	0.36	0.1	0.04	0	0	0.23	0	0	0.25	0.35	0.24	0	0.07	0
TOTAL	98.19	98.53	98.36	98.65	98.64	99.83	98.04	98.22	98.02	98.37	98.4	98.59	98.63	98.96	99.51	99.04	98.34	99.29
Tot.ox	8	8	8	8	8	8	8	8	8	8	8	8	8	8	8	8	8	8
Cation																		
Si	12.14	12.20	12.16	12.08	12.03	12.55	12.15	12.16	12.12	11.65	11.9	12.28	11.60	11.84	11.68	12.18	11.96	12.01
Ti	5	9	7	2	5	4	8	9	4	1	4	1	5	1	7	2	5	3
Al	4.139	4.093	4.113	4.176	4.202	4.172	4.18	4.172	4.195	4.646	4.35	4.177	4.643	4.494	4.695	4.289	4.265	4.301
Fe	0	0	0	0	0	0	0	0	0	0	0.01	0	0	0.018	0	0.014	0.037	0.028
Ca	0.246	0.142	0.172	0.242	0.29	0.082	0.185	0.112	0.16	0.562	0.34	0.153	0.574	0.376	0.593	0.218	0.098	0.103
Na	3.992	4.109	4.131	4.177	4.047	3.97	3.899	4.147	4.035	3.466	3.87	3.932	3.627	3.806	3.662	3.958	4.043	3.823
K	0.007	0.006	0.009	0.005	0.013	0.019	0.036	0.006	0.008	0.045	0.03	0.035	0.044	0.05	0.047	0.029	0.206	0.495
Ba	0	0.031	0.011	0.011	0.028	0.007	0.003	0	0	0.018	0	0	0.019	0.027	0.018	0	0.005	0
TOTAL	20.53	20.56	20.59	20.68	20.59	20.8	20.46	20.61	20.52	20.37	20.5	20.58	20.49	20.58	20.68	20.69	20.61	20.76
An	5.8	3.33	4	5.46	6.66	2	4.48	2.62	3.81	13.79	8	3.72	13.52	8.89	13.78	5.19	2.25	2.32
Ab	94.03	96.53	95.8	94.43	93.04	97.54	94.65	97.24	96	85.09	91.2	95.42	85.44	89.94	85.13	94.12	93.02	86.49
Or	0.17	0.14	0.2	0.11	0.3	0.46	0.87	0.14	0.2	1.12	0.76	0.86	1.04	1.17	1.08	0.68	4.73	11.19

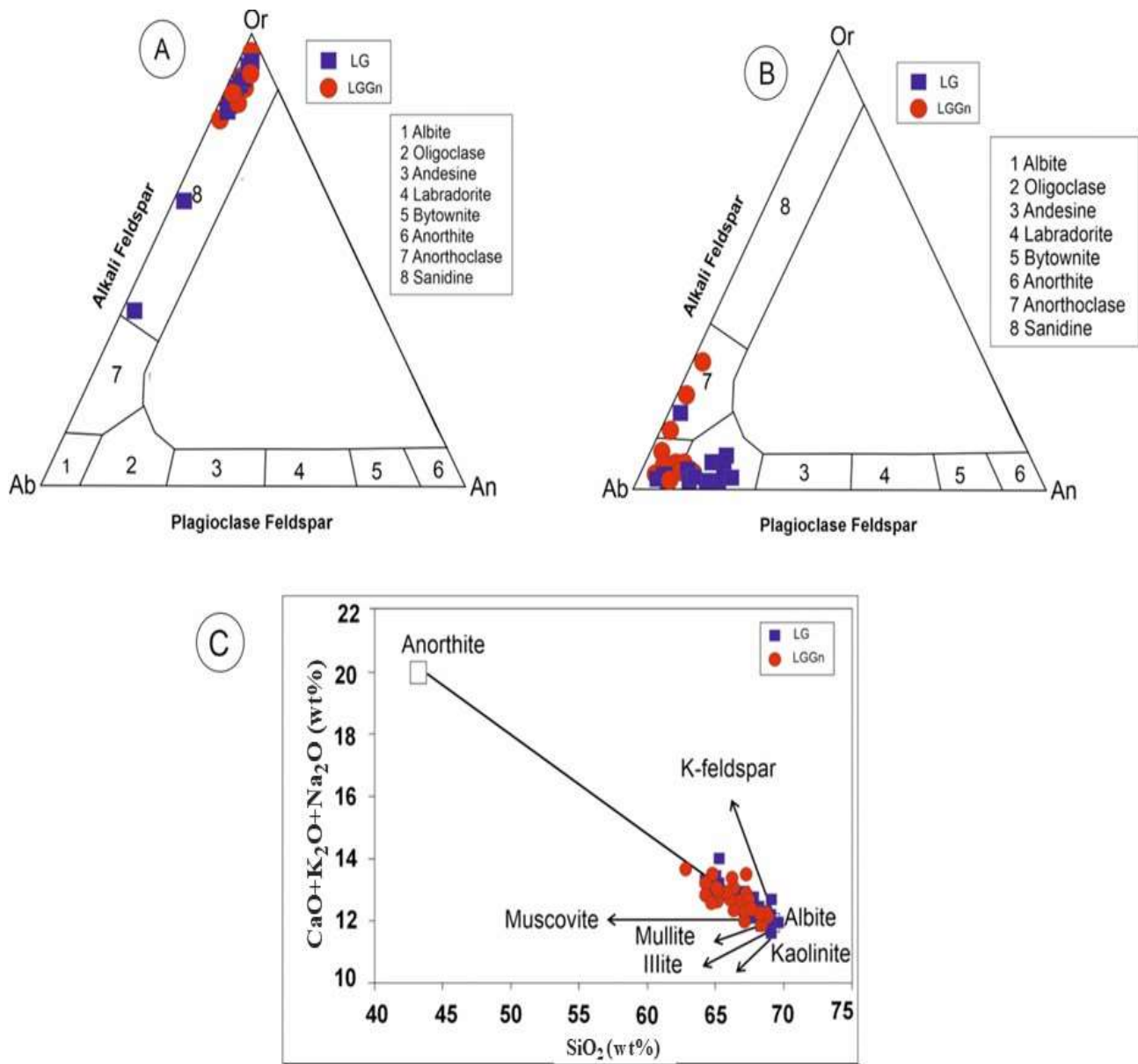


Figure 7. (A) Feldspars (Ab-Or-An) triangular diagram showing compositions of analysed granite and granite gneiss samples of Lansdowne Klippe. LG- Lansdowne Granite, LGGn- Lansdowne Granite gneiss. (B) Feldspars (Ab-Or-An) triangular diagram showing compositions of analyzed plagioclase from granite and granite gneiss samples of Lansdowne Klippe. LG- Lansdowne Granite, LGGn- Lansdowne Granite gneiss. (C) SiO₂ vs. CaO+Na₂O+K₂O (wt. %) binary diagram (after Williamson et al., 2016) for plagioclases from granite and granite gneiss. All samples follow the Ab-An tie line corresponding to unaltered composition. LG- Lansdowne Granite, LGGn- Lansdowne Granite gneiss.

Plagioclase

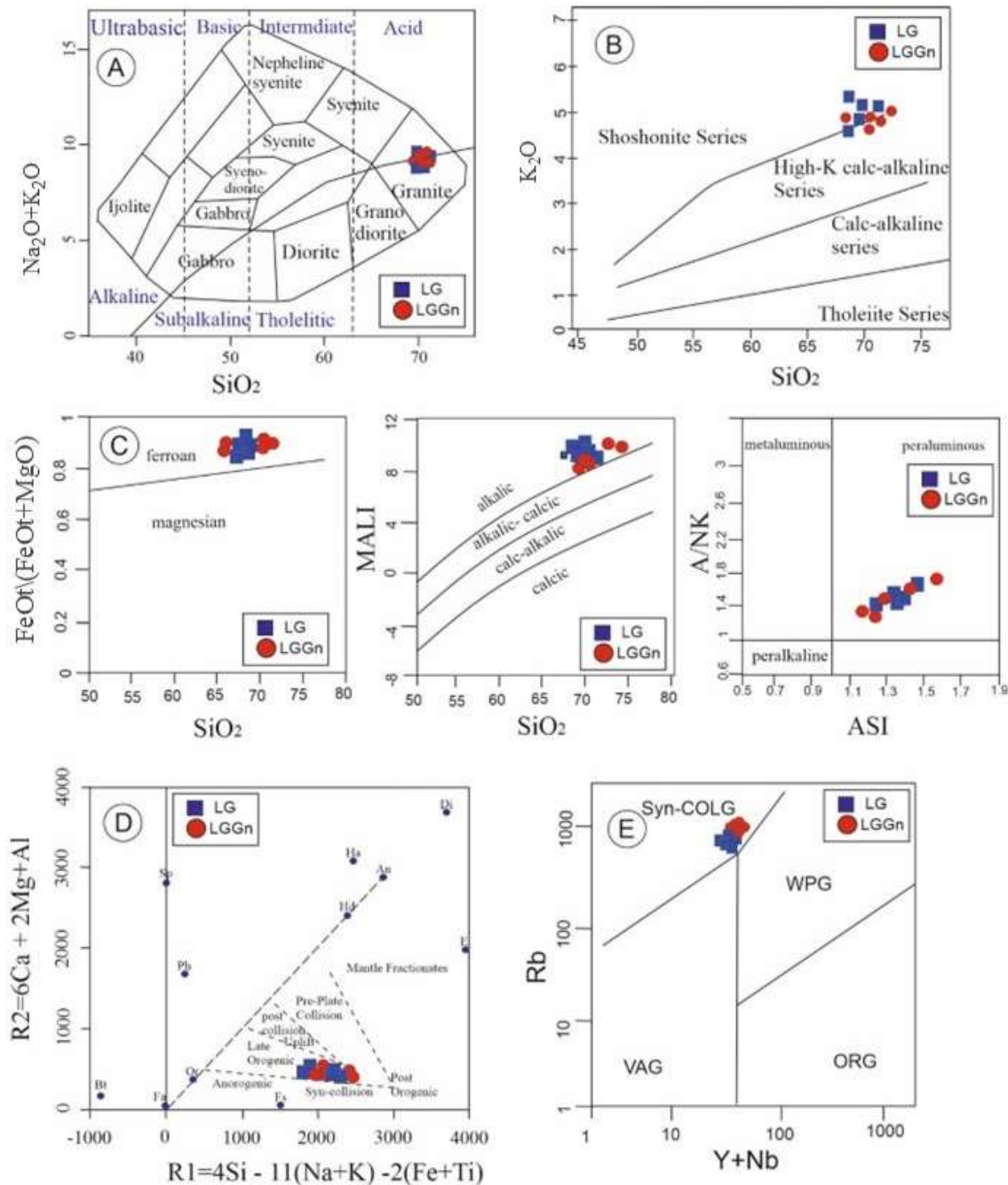
In granite, plagioclase show a high albitic composition with a limited variation (Ab=84.75-99.67, An=0.00-14.55) and very low K (K_{apfu} = 0.00-0.37), probably suggesting the source of host magma was continent crust. Most of the analyzed spots of plagioclase from LG, fall in albite to oligoclase field (Figure 7B). The LGGn plagioclase (Ab = 84.86-99.26, An = 0.02-13.79) is almost similar to LG plagioclase and clustering in albitic to oligoclase plagioclase field (Figure 7) with relatively low K (K_{apfu} =0.021-0.73). In SiO₂ vs. CaO+Na₂O+K₂O wt. %

plot, all the analysed plagioclases from LG and LGGn fall on the An, and Ab tie line indicating specifically the connection between An and Ab forming a compositional spectrum known as the plagioclase feldspar series (Figure 7C), their position on this tie-line help to classify feldspars according to their chemical compositions and crystallization conditions suggesting their magmatic origin which is petrographically explained by textures such as zoning, twining and inclusion patterns. However, the observed more albitic nature and high SiO₂ contents for LG and LGGn plagioclase, may have been

caused by post-magmatic albitization (Williamson et al., 2016), or evolved nature of host melt.

In the $\text{Na}_2\text{O} + \text{K}_2\text{O}$ versus SiO_2 binary diagram the granite and granite gneiss are categorized in the granite field (Figure 8A). The K_2O versus SiO_2 binary plot, defines that granite and granite gneisses belong to shoshonite magma series. It follows distinct ferroan trend, displaying an alkalic-alkali-calcic composition, illustrating its peraluminous nature (Figure 8B, C). R_1 - R_2 [$R_1 = 4\text{Si}^{4+} - 11(\text{Na}^{++}\text{K}^{+}) - 2(\text{Fe}^{3++}\text{Ti}^{4+})$, molar; $R_2 = 6\text{Ca}^{2++}2\text{Mg}^{2++}\text{Al}^{3+}$, molar] tectonic discrimination diagram

displays, syn-collisional tectonic setting of granite and granite gneiss reflecting their crustal source, peraluminous nature and enrichment in Al, Ca, and Mg due to partial melting of meta sedimentary rocks during continental collision (Figure 8D). Rb vs. (Y + Nb) diagram suggests their syn-collisional tectonic setting (Figure 8E). Based on geochemical analysis, they are enriched in LREE and relatively depleted in HREE, with prominent negative Eu anomalies and high Rb, K, Th and Y content, showing positive anomaly as well as negative Ba, Zr, Ti, and Nb anomalies (Figure 8F).



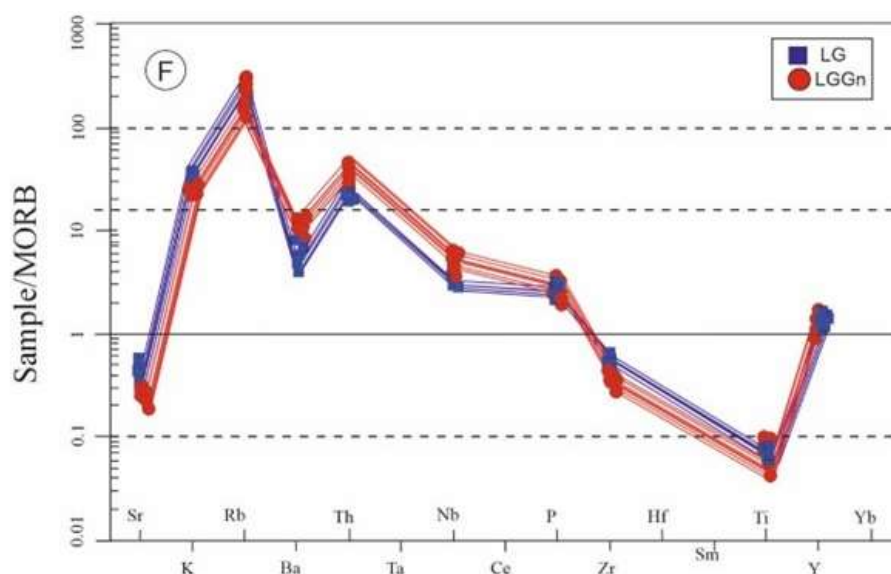


Fig 8. (A) Binary Plot ($\text{Na}_2\text{O} + \text{K}_2\text{O}$) versus SiO_2 (B) Binary plot (K_2O versus SiO_2) granite and granite gneiss belonging to the high K calc-alkaline to shoshonite magma series after (Le Maitre et al., 1989). (C) $\text{FeO}t/\text{FeO}t+\text{MgO}$ vs SiO_2 , modified alkali lime index (MALI) vs SiO_2 and Alumina saturation index (ASI) vs SiO_2 plots are after Frost et al. (2001). (D) The $\text{R1} - \text{R2}$ [$\text{R1} = 4\text{Si}_4+11(\text{Na}++\text{K}+)2(\text{Fe}_3++\text{Ti}_4+)$, molar; $\text{R2} = 6\text{Ca}_2++2\text{Mg}_2++\text{Al}_3+$, molar] (after Batchelor and Bowden, 1985) tectonic discrimination diagram showing syn-collision type of tectonic setting. (E) $(\text{Yb} + \text{Nb})$ vs Rb discrimination diagram of granite and granite gneiss (after Pearce et al., 1984). (F) Spider diagram of the granite and granite gneiss. LG- Lansdowne Granite, LGGn- Lansdowne Granite gneiss.

Mineral chemistry data reveals feldspar formation by fractional differentiation of the granitic magma. Its component suggest the crystallization at high temperature, with magmatic origin.

CONCLUSIONS

Following conclusions can be drawn from the present study

(i) Field observations reveal that the studied granite is a small pluton consisting quartz and feldspar phenocrysts, exhibiting porphyritic texture. Granites are transformed into granitic gneiss due to metamorphism and deformation.

(ii) Petrography of granite and granite gneiss reveals porphyritic, porphyroblastic, perthitic, and equigranular textures, exhibiting Carlsbad and albite twinning. These features indicate slow magma cooling, dual crystallization, and differential mineral growth suggesting the rock was emplaced at a specific depth.

(iii) The geochemical data indicate their affinity to S-type granite, showing syn-collisional tectonic settings, and its evolution is related to partial melting of continental crust derived from metasedimentary source.

(iv) Mineral chemistry of K-feldspar suggests that the crystallization occurred above the solidus at high temperature, illustrating its evolved nature of host magmatic melt.

ACKNOWLEDGEMENTS

The authors are highly thankful to Prof. N V Chalapathi Rao for providing permission to use electron probe microanalytical facility at Banaras Hindu University, Varanasi (U.P.) India. Dr.

Rohit Pandey and Mohd. Anas rendered the analytical help. The authors express their gratitude to Dr. O. P. Pandey, the Chief editor, for his insightful feedback and for editing the final manuscript. The authors are also thankful to anonymous reviewers for their comments and suggestions.

Author Credit Statement

Deepa Arya and Gunjan Arya are responsible for inception and preparation of the manuscript and R.B. Ananth have contributions in data generation.

Data Availability

The data supporting this study's findings are available from the corresponding author upon reasonable request.

Compliance with Ethical Standards

The authors declare no conflict of interest and adhere to copyright norms.

REFERENCES

- Arya. G., 2024. Petrogenesis of granites and granite gneiss from Lansdowne klippe, Garhwal Lesser Himalaya, Uttarakhand. (Unpublished)
- Auden, J.B., 1937. Structure of the Himalaya in Garhwal. Rec. Geol. Survey India, 71, 407-433.
- Batchelor, R.A. and Bowden. P., 1985. Petrogenetic interpretation of granitoid rock series using multi cationic parameters. Chem. Geol., 48, 43-55.
- Bhatnagar, S. P. and Sharma, V. K., 1989. Geology of the Higher Himalaya in the Kinnaur-Spiti region, northwest Himalaya, India. J. Geol. Soc. India, 33(1), 23-46.

- Chakraborty, S., Dasgupta, S. and Bhattacharya, A., 1994. Origin of the granites of the Lesser Himalayas, India, geochemical and isotopic constraints. *Precamb. Res.*, 67(3-4), 321-340.
- Dasgupta, S., Chakraborty, S. and Bhattacharya, A., 1996. Geochemical constraints on the origin of the granites of the Lesser Himalayas, India. *J. Petrol.*, 37(6), 1521-1540.
- Eldson, R. and Gupta, L.N., 1981. Petrochemical studies of the Lansdowne Granite Gneiss, Lesser Himalaya, India. *J. Geol. Soc. India*, 22, 503-516.
- Frost, B.R., Barnes, C.G., Collins, W.J., Arculus, R.J., Ellis, D.J. and Frost, C.D., 2001. Geochemical Classification for Granitic Rocks. *J. Petrol.*, 42, 2033-2048.
- Fuchs, G. and Sinha, A.K., 1978. The Tectonics of the Garhwal-Kumaun Lesser Himalaya. *Jahrb. Geol. Bundesanst.*, 121, 219-241.
- Gupta, L. N., 1976a. A contribution to the geology of the Lansdowne area, Garhwal Himalayas, India. *J. Geol. Soc. India*, 17, 449-460.
- Gupta, L. N., 1976b. Abnormal tectonics of the allochthonous Lansdowne granite and the tectonic history of Garhwal nappe. *Indian Mineral*, 17, 73-85.
- Islam, R., Ahmad, T. and Khanna, P. P., 2005. An overview on the granitoids of the NW Himalaya. *Himalayan Geol.*, 26 (1), 49-60.
- Kumar, G. and Daundhiyal, J. N., 1980. On the stratigraphic position of the Tal formation, Garhwal synform, Garhwal, and Tehri Garhwal districts, Uttar Pradesh. *J. Paleontol. Soc. India*, 23-24, 58-66.
- Le Fort, P., 1988. Granites in the tectonic evolution of Himalaya, Karakoram, and southern Tibet. In: *Tectonic evolution of the Himalayas and Tibet*. *Phil. Trans. R. Soc. London.*, 326, 281-299.
- Le Maitre, R.W., 2002. Igneous rocks: a classification and glossary of terms. Recommendations of International Union of Geological Science. Subcommission on the systematics of Igneous Rocks. 2nd Edition Cambridge University Press, Cambridge, 236p.
- Le Maitre, R.W., Bateman, P., Dudek, A., Keller, J. and Lameyre, J. 1989. A Classification of Igneous Rocks and Glossary of Terms: Recommendations of the International Union of Geological Sciences Sub-Commission on the Systematics of Igneous Rocks. New York: Cambridge University Press.
- Pearce, J. A., Harris, N. B. W. and Tindle, A. G., 1984. Trace element discrimination diagrams for the tectonic interpretation of granitic rocks. *J. Petrol.*, 25, 956-983.
- Rai, S. S. and Kumar, S., 2015. Tectonic evolution and granite genesis of the Himalayan orogen: an appraisal. *J. Asian Earth Sci.*, 102, 185-215.
- Saklani, P.S., 1993. Geology of the Lower Himalaya (Garhwal). International Books and Periodicals Supply Service, New Delhi, 14, 246.
- Santosh, M., Tandon, S. K. and Bhatt, S. C., 2003. Himalayan granitoids: constraints on the crustal evolution of the Himalayan orogen. *J. Virtual Explorer*, 11, 59-78.
- Shanker, R. and Ganesan, T.M., 1973. A note on the Garhwal nappe. *Himalayan Geology*, 3, 72-82.
- Tandon, S. K. and Bhatt, S. C., 1995. Structural analysis of the Lesser Himalayan sequence in the Garhwal Himalaya, India. *Geol. Soc. Am. Bull.*, 107(6), 643-652.
- Upadhyay, R. and Singh, V. P., 2000. Petrogenesis of the granitoids of the Lesser Himalaya, India: a study based on Sr-Nd isotopes and trace element geochemistry. *Geol. Mag.*, 137(6), 649-665.
- Valdiya, K.S., 1980. Geology of Kumaun Lesser Himalaya. Wadia Institute of Himalayan Geology, Dehradun, pp. 291.
- Vishnoi, R.K., 1971. Geology of the Area Around Lansdowne (District Pauri, U.P.) with Special reference to the Study of Granite Gneiss. Master's Thesis (Earth Sci.). Indian Institute of Technology, Roorkee, pp. 87.
- Williamson, B. J., Herrington, R. J. and Morris, A., 2016. Porphyry copper enrichment linked to excess aluminium in plagioclase. *Nat. Geosci.*, 9, 237-241.

Received on: 17-04-2025; Revised on: 23-06-2025 ; Accepted on: 29-06-2025

Impact of triangular irregularity on the dispersion of SH-waves in a monoclinic crustal layer overlying a dry sandy medium

Tanishqa Shivaji Veer, A. Akilbasha and Vijay Kumar Kalyani*

Department of Mathematics and Statistics

Dr. Vishwanath Karad MIT World Peace University, Pune-411038, Maharashtra, India

*Corresponding author: vijaykumar.kalyani@mitwpu.edu.in

ABSTRACT

In the present paper, a comprehensive study of dispersion characteristics of SH-waves in a monoclinic crustal layer lying over a dry-sandy half-space, with special emphasis on the effect of a triangular irregularity at the interface, has been conducted. We have considered both isotropic and monoclinic layer for the analysis of SH-wave propagation with or without sandiness in the half-space. The governing equations representing equation of motion of SH-waves in a monoclinic medium, is formulated to develop dispersion relation. Further, the results are analyzed and discussed for the variation in various physical parameters such as depth of triangular irregularity, sandiness and the directional dependencies in the monoclinic medium. Moreover, a comparative study has been conducted to assess the extent to which these parameters affect SH-wave propagation differently in monoclinic and isotropic layers. These results are illustrated graphically to highlight the importance of considering interfacial irregularity in seismic wave studies.

Keywords: SH-waves, dispersion, triangular irregularity, monoclinic medium, dry-sandy half-space.

INTRODUCTION

As is well known, SH-waves are seismic waves that move horizontally through the Earth's surface. These waves are particularly useful for studying underground structures as they travel within layered boundaries. It is essential for geophysicists to understand the behavior of such waves in the solids beneath Earth's surface. These solids in the Earth's interior are commonly referred to as minerals or mineral rocks. Minerals with distinct geometric structures are known as crystals. Although crystals can take various forms namely, hexagonal, triclinic, monoclinic, orthorhombic, cubic, tetragonal, and trigonal, nearly one-third of the minerals in the Earth's interior belong to the monoclinic crystalline form. Hence, there is a need to study SH-wave behavior in such media. Several authors have analyzed the dispersion of seismic waves through the monoclinic medium in their studies (Chattopadhyay and Saha, 1996; Kaur and Tomar, 2004). In a related work, Kalyani et al. (2008) presented a model for seismic wave propagation in monoclinic media using the finite difference method. It demonstrated that the anisotropy in the monoclinic medium, hinders the phase velocity of the medium. Sethi and Sharma (2016) discussed the dispersion of SH-waves in a non-homogeneous monoclinic layer over a semi-infinite isotropic medium. Recently, Khan et al. (2021) examined the influence of initial stress on the propagation of SH-waves over a heterogeneous monoclinic half-space. In their work, they studied the variation in the depth of irregularity and non-homogeneity on the phase velocity of the waves. Pradhan et al. (2023) investigated the SH-wave propagation due to a point source at the interface between monoclinic and heterogenous media. They showed that the heterogeneity hinders the phase velocity. Further, Pradhan et al. (2025) extended their study to a two layered structure of functionally graded viscoelastic and monoclinic media, demonstrating the impact of various

gradient parameters on dispersion curves, phase velocity, group velocity, and wave number of SH-waves.

The study of seismic waves in the half-space beneath the Earth's crust provides valuable information about the structure of Earth, which plays an important role in the propagation of SH-waves. Although these half-spaces are primarily composed of solid rocks, some may also contain unconsolidated dry sand. Generally, it is observed that SH-waves propagate more slowly through dry sandy media due to energy absorption by the sand grains. Several researchers have considered dry sandy media to study the propagation of seismic waves. For example, Tomar and Kaur (2007) investigated the reflection and transmission of SH-waves at the interface between a dry sandy and an anisotropic half-space. Pal et al. (2016) analyzed the effects of the sandiness parameter and material inhomogeneity on the dispersion of SH-waves propagating through a dry sandy layer, sandwiched between an inhomogeneous isotropic and a homogeneous isotropic half-space. More recently, Madan et al. (2023a) analyzed SH-wave propagation in an orthotropic elastic layer confined between a dry sandy layer and a half-space, highlighting the effect of various parameters on dispersion. Further, in the same year, Madan et al. (2023b) examined Rayleigh waves in an isotropic sandy layer overlying a semi-infinite sandy medium, showing the influence of sandiness on phase velocity.

In earlier studies, different authors in their work assumed interfaces to be perfectly uniform. However, in actual scenarios, geological interfaces are rarely smooth. The Earth's subsurface consists of layered materials with irregularities at the interfaces between different media. The propagation of SH-waves in such layered geological structures is significantly influenced by these geometric irregularities. Numerous studies have examined such irregularities, which affect dispersion of waves with varying layer properties and shapes of the

irregularities. Early investigations (Chattopadhyay, 1975; Chattopadhyay and De, 1983) analyzed SH-wave propagation in different media with interfacial irregularities. Kar et al. (1986) studied Love wave propagation in a dry sandy layer having a parabolic irregularity and reported a decrease in phase velocity due to both the sandy medium and the irregular interface. Kalyani and Kar (1986) extended this investigation to anisotropic porous layers sandwiched between two homogeneous half-spaces. They showed that the irregularity at the interface reduces the phase velocity. Further, Chattopadhyay et al. (2008) studied SH-wave propagation in a monoclinic crustal layer lying over an isotropic half-space having a rectangular irregularity at the interface, and found that the depth of the irregularity has a substantial impact on phase velocity of the wave. In a comparative study, Acharya and Roy (2009) analyzed the effects of both parabolic and rectangular irregularities on SH-wave propagation in a magneto-elastic crustal layer. Recently, the effect of rectangular irregularities at the interface on the dispersion of seismic waves has been investigated in different media by several authors, namely Kumar et al. (2015), Gupta et al. (2021), and Kumar and Madan (2022). In a related work, Madan et al. (2024) analyzed Love wave dispersion in a viscoelastic sandy layer over an anisotropic half-space with a parabolic irregularity at the interface, showing the effects of irregularity, sandiness, and dissipation.

Practically, in all these studies, the authors have assumed either parabolic or rectangular irregularities in their models to study SH-wave propagation in different media. However, the present research focuses on triangular irregularity which has significant effect on SH-wave dispersion in such a layered structure. The key focus areas of this study, when the layer is monoclinic, include variations in phase velocity due to the change in (i) the directional dependencies in a monoclinic layer, (ii) depth of triangular irregularities, (iii) the degree of sandiness in the half-space, and (iv) their combined effects. The results of these studies in monoclinic layer have also been compared with the results obtained by assuming the layer to be isotropic and which are also illustrated graphically.

CONCEPT OF CRYSTALLINE MATERIAL

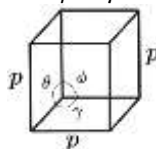
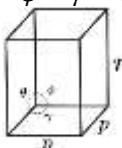
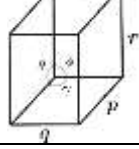
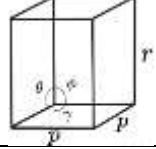
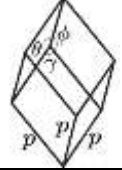
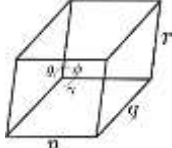
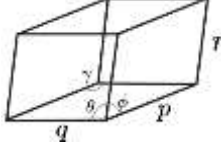
It is a well-known fact that the Earth's crust consists of different minerals having various crystallographic symmetries. Based on their structural arrangements, these crystalline materials are classified into seven crystal systems. Due to their anisotropic nature, these systems influence the seismic wave propagation causing waves to travel at different velocities depending on the crystallographic orientation as a result of their elastic stiffness variations. The stiffness tensors C_{ijkl} capture the anisotropic behavior of these systems with its components constrained by material symmetries. Higher the symmetry of the systems leads to less independent constants resulting in low anisotropy of the material, and lower the symmetry of systems leads to more independent constants resulting in high directional dependency of the material e.g., in cubic system, there are only three independent constants and hence it is isotropic in nature, however, there are twenty-one independent constants in triclinic system and hence it is highly anisotropic. The geometrical properties of the seven crystal systems, along with their stiffness matrices, are presented in Table-1 (Nye, 1985).

Each of these crystal systems, due to their anisotropic characteristics, influence the seismic waves traveling in the Earth's interior. In the present study, a monoclinic medium is considered, where the reduced symmetry with thirteen independent elastic constants results in more complex wave behavior. This model is used to examine the effect of anisotropy on the propagation of SH-waves.

DEVELOPMENT OF THE MODEL

Let us assume a monoclinic crustal layer (M_1) with a triangular irregularity of width $2a$ and depth $h \ll a$ at the interface between the layer and a dry sandy half-space (M_2). The coordinate system is considered with z-axis oriented vertically downwards and x-axis along the interface as illustrated in Figure 1. Let H be the thickness of the monoclinic layer. Additionally, the source generating SH-waves is taken at the depth $d \gg h$ along the z-axis.

Table 1. Geometrical properties of crystals

Crystal system	Edge lengths and angles	Stiffness Matrix
Cubic	$p = q = r,$ $\theta = \phi = \gamma = 90^\circ$ 	Independent Constants: 3 $\begin{bmatrix} C_{11} & C_{12} & C_{12} & 0 & 0 & 0 \\ C_{12} & C_{11} & C_{12} & 0 & 0 & 0 \\ C_{12} & C_{12} & C_{11} & 0 & 0 & 0 \\ 0 & 0 & 0 & C_{44} & 0 & 0 \\ 0 & 0 & 0 & 0 & C_{44} & 0 \\ 0 & 0 & 0 & 0 & 0 & C_{44} \end{bmatrix}$
Tetragonal	$p = q \neq r,$ $\theta = \phi = \gamma = 90^\circ$ 	Independent Constants: 6 $\begin{bmatrix} C_{11} & C_{12} & C_{13} & 0 & 0 & 0 \\ C_{12} & C_{11} & C_{13} & 0 & 0 & 0 \\ C_{13} & C_{13} & C_{33} & 0 & 0 & 0 \\ 0 & 0 & 0 & C_{44} & 0 & 0 \\ 0 & 0 & 0 & 0 & C_{44} & 0 \\ 0 & 0 & 0 & 0 & 0 & C_{66} \end{bmatrix}$
Orthorhombic	$p \neq q \neq r,$ $\theta = \phi = \gamma = 90^\circ$ 	Independent Constants: 9 $\begin{bmatrix} C_{11} & C_{12} & C_{13} & 0 & 0 & 0 \\ C_{12} & C_{22} & C_{23} & 0 & 0 & 0 \\ C_{13} & C_{23} & C_{33} & 0 & 0 & 0 \\ 0 & 0 & 0 & C_{44} & 0 & 0 \\ 0 & 0 & 0 & 0 & C_{55} & 0 \\ 0 & 0 & 0 & 0 & 0 & C_{66} \end{bmatrix}$
Hexagonal	$p = q \neq r,$ $\theta = \phi = 90^\circ, \gamma = 120^\circ$ 	Independent Constants: 5 $\begin{bmatrix} C_{11} & C_{12} & C_{13} & 0 & 0 & 0 \\ C_{12} & C_{11} & C_{13} & 0 & 0 & 0 \\ C_{13} & C_{13} & C_{33} & 0 & 0 & 0 \\ 0 & 0 & 0 & C_{44} & 0 & 0 \\ 0 & 0 & 0 & 0 & C_{44} & 0 \\ 0 & 0 & 0 & 0 & 0 & \frac{C_{11}-C_{12}}{2} \end{bmatrix}$
Trigonal	$p = q = r,$ $\theta = \phi = \gamma \neq 90^\circ$ 	Independent Constants: 7 $\begin{bmatrix} C_{11} & C_{12} & C_{13} & C_{14} & 0 & 0 \\ C_{12} & C_{11} & C_{13} & -C_{14} & 0 & 0 \\ C_{13} & C_{13} & C_{33} & 0 & 0 & 0 \\ C_{14} & -C_{14} & 0 & C_{44} & 0 & 0 \\ 0 & 0 & 0 & 0 & C_{44} & C_{14} \\ 0 & 0 & 0 & 0 & C_{14} & \frac{C_{11}-C_{12}}{2} \end{bmatrix}$
Monoclinic	$p \neq q \neq r,$ $\theta = \gamma = 90^\circ, \phi \neq 90^\circ$ 	Independent Constants: 13 $\begin{bmatrix} C_{11} & C_{12} & C_{13} & 0 & C_{15} & 0 \\ C_{12} & C_{22} & C_{23} & 0 & C_{25} & 0 \\ C_{13} & C_{23} & C_{33} & 0 & C_{35} & 0 \\ 0 & 0 & 0 & C_{44} & 0 & C_{46} \\ C_{15} & C_{25} & C_{35} & 0 & C_{55} & 0 \\ 0 & 0 & 0 & C_{46} & 0 & C_{66} \end{bmatrix}$
Triclinic	$p \neq q \neq r,$ $\theta \neq \phi \neq \gamma \neq 90^\circ$ 	Independent Constants: 21 $\begin{bmatrix} C_{11} & C_{12} & C_{13} & C_{14} & C_{15} & C_{16} \\ C_{12} & C_{22} & C_{23} & C_{24} & C_{25} & C_{26} \\ C_{13} & C_{23} & C_{33} & C_{34} & C_{35} & C_{36} \\ C_{14} & C_{24} & C_{34} & C_{44} & C_{45} & C_{46} \\ C_{15} & C_{25} & C_{35} & C_{45} & C_{55} & C_{56} \\ C_{16} & C_{26} & C_{36} & C_{46} & C_{56} & C_{66} \end{bmatrix}$

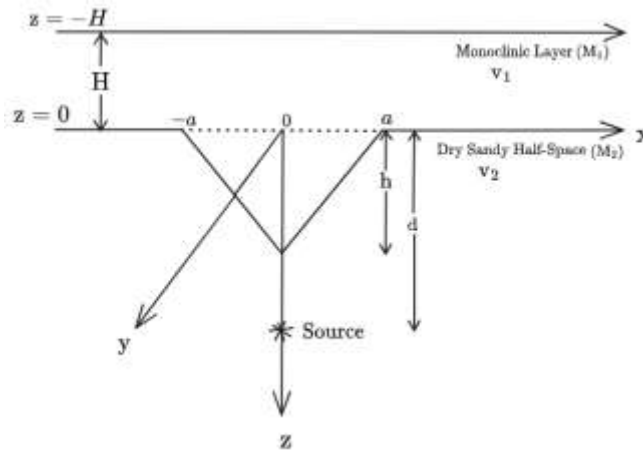


Figure 1. Geometrical description of the model

The geometry of the interface is mathematically represented by:

$$z = \epsilon f(x)$$

Where

$$f(x) = \begin{cases} h \left(1 - \frac{|x|}{a} \right), & \text{for } |x| \leq a \\ 0, & \text{for } |x| > a \end{cases} \quad (1)$$

in which, $\epsilon = \frac{h}{2a} \ll 1$ serves as the small perturbation parameter.

SH-waves in monoclinic layer

The stress-strain relations for a monoclinic elastic medium with its plane of symmetry normal to the y-axis are expressed as (Pradhan et al., 2023)

$$\begin{bmatrix} T_{xx}^{(1)} \\ T_{yy}^{(1)} \\ T_{zz}^{(1)} \\ T_{yz}^{(1)} \\ T_{xz}^{(1)} \\ T_{xy}^{(1)} \end{bmatrix} = \begin{bmatrix} C_{11} & C_{12} & C_{13} & 0 & C_{15} & 0 \\ C_{12} & C_{22} & C_{23} & 0 & C_{25} & 0 \\ C_{13} & C_{23} & C_{33} & 0 & C_{35} & 0 \\ 0 & 0 & 0 & C_{44} & 0 & C_{46} \\ C_{15} & C_{25} & C_{35} & 0 & C_{55} & 0 \\ 0 & 0 & 0 & C_{46} & 0 & C_{66} \end{bmatrix} \begin{bmatrix} S_1 \\ S_2 \\ S_3 \\ S_4 \\ S_5 \\ S_6 \end{bmatrix} \quad (2)$$

where, $T_{xx}^{(1)}, T_{yy}^{(1)}, T_{zz}^{(1)}, \dots$ denote the stress components of stress tensor, $C_{kj} (k, j = 1, 2, \dots, 6)$ are the elastic coefficients and $S_k (k = 1, 2, \dots, 6)$ are the strain-displacement relations defined as

$$S_1 = \frac{\partial u_1}{\partial x}, S_2 = \frac{\partial v_1}{\partial y}, S_3 = \frac{\partial w_1}{\partial z}, S_4 = \frac{\partial w_1}{\partial y} + \frac{\partial v_1}{\partial z}, S_5 = \frac{\partial u_1}{\partial z} + \frac{\partial w_1}{\partial x}, S_6 = \frac{\partial v_1}{\partial x} + \frac{\partial u_1}{\partial y}. \quad (3)$$

In the absence of body forces, the equations of motion are given by

$$\left. \begin{aligned} \frac{\partial T_{xx}^{(1)}}{\partial x} + \frac{\partial T_{xy}^{(1)}}{\partial y} + \frac{\partial T_{xz}^{(1)}}{\partial z} &= \rho_1 \frac{\partial^2 u_1}{\partial t^2}, \\ \frac{\partial T_{yx}^{(1)}}{\partial x} + \frac{\partial T_{yy}^{(1)}}{\partial y} + \frac{\partial T_{yz}^{(1)}}{\partial z} &= \rho_1 \frac{\partial^2 v_1}{\partial t^2}, \\ \frac{\partial T_{zx}^{(1)}}{\partial x} + \frac{\partial T_{zy}^{(1)}}{\partial y} + \frac{\partial T_{zz}^{(1)}}{\partial z} &= \rho_1 \frac{\partial^2 w_1}{\partial t^2}, \end{aligned} \right\} \quad (4)$$

where ρ_1 is the density of the monoclinic layer M_1 . Here, the subscript and superscript '1' indicate monoclinic layer M_1 .

Considering SH-waves traveling in the positive direction of x-axis and polarised in y-direction, we have

$$u = 0, \quad v = v(x, z, t), \quad w = 0. \quad (5)$$

Substituting Eqs. (3) and (5) in Eq. (2), the stress-strain relations reduce to

$$\begin{aligned} T_{xx}^{(1)} = T_{yy}^{(1)} = T_{zz}^{(1)} = T_{xz}^{(1)} = 0, \quad T_{yz}^{(1)} &= C_{44} \frac{\partial v_1}{\partial z} + C_{46} \frac{\partial v_1}{\partial x}, \quad T_{xy}^{(1)} \\ &= C_{46} \frac{\partial v_1}{\partial z} + C_{66} \frac{\partial v_1}{\partial x}. \end{aligned} \quad (6)$$

Substituting Eq. (6) into Eq. (4), the propagation of SH-waves in the monoclinic layer obtained as

$$C_{66} \frac{\partial^2 v_1}{\partial x^2} + 2C_{46} \frac{\partial^2 v_1}{\partial x \partial z} + C_{44} \frac{\partial^2 v_1}{\partial z^2} = \rho_1 \frac{\partial^2 v_1}{\partial t^2}. \quad (7)$$

Using the time harmonic solution,

$$v_1 = V_1(x, z) e^{i\omega t},$$

in Eq. (7), we get

$$C_{66} \frac{\partial^2 V_1}{\partial x^2} + 2C_{46} \frac{\partial^2 V_1}{\partial x \partial z} + C_{44} \frac{\partial^2 V_1}{\partial z^2} + \omega^2 \rho_1 V_1 = 0, \quad (8)$$

where ω represents the angular frequency.

The Fourier and inverse Fourier transform of $V_1(x, z)$ is given by (Kreyszig, 2006):

$$\left. \begin{aligned} \bar{V}_1(\zeta, z) &= \int_{-\infty}^{\infty} V_1(x, z) e^{i\zeta x} dx, \\ V_1(x, z) &= \frac{1}{2\pi} \int_{-\infty}^{\infty} \bar{V}_1(\zeta, z) e^{-i\zeta x} d\zeta. \end{aligned} \right\} \quad (9)$$

Applying the above defined Fourier transform to Eq. (8), we have

$$C_{44} \frac{d^2 \bar{V}_1}{dz^2} - 2i\zeta C_{46} \frac{\bar{V}_1}{dz} + (\omega^2 \rho_1 - \zeta^2 C_{66}) \bar{V}_1 = 0. \quad (10)$$

Therefore, the solution of Eq. (10) is

$$\bar{V}_1 = e^{-\frac{s}{2}z} (A \cos p_1 z + B \sin p_1 z), \quad (11)$$

where A and B are arbitrary constants, and

$$s = -\frac{2i\zeta C_{46}}{C_{44}}, \quad p_1 = \sqrt{\frac{\omega^2}{\beta_1^2} - \zeta^2 \frac{C_{66}}{C_{44}} + \zeta^2 \frac{C_{46}^2}{C_{44}^2}}, \quad \beta_1 = \sqrt{\frac{C_{44}}{\rho_1}}. \quad (12)$$

By taking the inverse Fourier transform of Eq. (11), the displacement of SH-wave propagation in the monoclinic medium is given by

$$V_1(x, z) = \frac{1}{2\pi} \int_{-\infty}^{\infty} e^{-\frac{s}{2}z} (A \cos p_1 z + B \sin p_1 z) e^{-i\zeta x} d\zeta. \quad (13)$$

SH-waves in dry sandy half-space

The stress-strain relations for a dry sandy half-space are expressed as (Pal, 1985)

$$\left. \begin{aligned} T_{xx}^{(2)} &= (\lambda + 2\mu_2)u_2 + \lambda v_2 + \lambda w_2, \\ T_{yy}^{(2)} &= \lambda u_2 + (\lambda + 2\mu_2)v_2 + \lambda w_2, \\ T_{zz}^{(2)} &= \lambda u_2 + \lambda v_2 + (\lambda + 2\mu_2)w_2, \\ T_{yz}^{(2)} &= \mu_2(w_2 + v_2), \\ T_{zx}^{(2)} &= \mu_2(u_2 + w_2), \\ T_{xy}^{(2)} &= \mu_2(u_2 + v_2), \end{aligned} \right\} \quad (14)$$

where, λ is the Lamé parameter and μ_2 is the rigidity of the dry sandy half-space given by

$$\mu_2 = \frac{\mu_0}{\eta},$$

where η represents the sandiness parameter and μ_0 denotes the rigidity of the classical elastic medium. The superscript and subscript '2' indicate dry sandy half-space M_2 .

Similarly, the equation of motion for propagation of SH-waves in the lower dry sandy half-space is given by (Kar et al., 1986)

$$\frac{\partial^2 v_2}{\partial x^2} + \frac{\partial^2 v_2}{\partial z^2} = \frac{1}{\beta_2^2} \frac{\partial^2 v_2}{\partial t^2}, \quad (15)$$

where, β_2 represents the speed of the SH-waves in the dry sandy semi-infinite medium, defined by:

$$\beta_2 = \frac{1}{\sqrt{\eta}} \beta'_2$$

in which,

$$\beta'_2 = \sqrt{\frac{\mu_0}{\rho_2}}$$

where ρ_2 denotes the density of the dry sandy half-space.

Using the time harmonic solution,

$$v_2 = V_2(x, z) e^{i\omega t},$$

in Eq. (15), we get

$$\frac{\partial^2 V_2}{\partial x^2} + \frac{\partial^2 V_2}{\partial z^2} + \eta \frac{\omega^2}{\beta_2'^2} V_2 = 0. \quad (16)$$

Applying the Fourier transform defined in Eq. (9) to Eq. (16), we get

$$\frac{d^2 \bar{V}_2}{dz^2} - \left(\zeta^2 - \eta \frac{\omega^2}{\beta_2'^2} \right) \bar{V}_2 = 0. \quad (17)$$

Thus, the solution of Eq. (17) is:

$$\bar{V}_2 = C e^{-p_2 z} \quad (18)$$

where C is the arbitrary constants, and

$$p_2 = \sqrt{\zeta^2 - \eta \frac{\omega^2}{\beta_2'^2}}. \quad (19)$$

By taking the inverse Fourier transform of Eq. (18), the displacement of SH-wave propagation in the dry sandy half-space is given by

$$V_2(x, z) = \frac{1}{2\pi} \int_{-\infty}^{\infty} \left(C e^{-p_2 z} + \frac{2}{p_2} e^{p_2 z} e^{-p_2 d} \right) e^{-i\zeta x} d\zeta, \quad (20)$$

where the second term in Eq. (20) for V_2 arises due to the contribution of the source in the lower medium (Pilot, 1979).

Boundary conditions

Since a monoclinic layer lies over a dry sandy semi-infinite medium, the boundary conditions:

(A) at the interface $z = \epsilon f(x)$ are:

(i) displacements are continuous:

$$v_1 = v_2 \quad (21)$$

(ii) shear stresses are continuous:

$$T_{yz}^{(1)} = T_{yz}^{(2)},$$

which gives,

$$\begin{aligned} C_{44} \frac{\partial v_1}{\partial z} + C_{46} \frac{\partial v_1}{\partial x} - \epsilon f'(x) \left(C_{46} \frac{\partial v_1}{\partial z} + C_{66} \frac{\partial v_1}{\partial x} \right) \\ = \frac{\mu_0}{\eta} \left(\frac{\partial v_2}{\partial z} - \epsilon f'(x) \frac{\partial v_2}{\partial x} \right) \end{aligned} \quad (22)$$

(B) at the upper boundary $z = -H$,

shear stress vanishes, we have

$$T_{yz}^{(1)} = 0,$$

which gives,

$$C_{44} \frac{\partial v_1}{\partial z} + C_{46} \frac{\partial v_1}{\partial x} = 0, \quad (23)$$

where, $f'(x) = \frac{df(x)}{dx}$.

For the irregular interface, A, B , and C are the functions of ϵ . Expanding them in the increasing powers of small ϵ and retaining terms up to first order, we have:

$$\begin{aligned} A \cong A_0 + \epsilon A_1, \quad B \cong B_0 + \epsilon B_1, \quad C \cong C_0 + \epsilon C_1, \\ e^{\pm g\epsilon f} \cong 1 \pm g\epsilon f, \quad \cos(p_1\epsilon f) \cong 1, \quad \sin(p_1\epsilon f) \cong p_1\epsilon f \end{aligned} \quad (24)$$

where, g is any quantity.

Using Eq. (24), the boundary conditions (21), (22), and (23) reduces to

$$\begin{aligned} (A_0 + \epsilon A_1) \left[C_{44} p_1 \sin p_1 H - C_{44} \frac{S}{2} \cos p_1 H - i\zeta C_{46} \cos p_1 z \right] \\ + (B_0 + \epsilon B_1) \left[C_{44} p_1 \cos p_1 H + C_{44} \frac{S}{2} \sin p_1 H \right. \\ \left. + i\zeta C_{46} \sin p_1 z \right] = 0 \end{aligned} \quad (25)$$

$$\begin{aligned} \epsilon \int_{-\infty}^{\infty} \left(A_0 \frac{S}{2} - B_0 p_1 - C_0 p_2 + 2e^{-dp_2} \right) f(x) e^{-i\zeta x} d\zeta \\ = \int_{-\infty}^{\infty} \left[A_0 - C_0 - \frac{2}{p_2} e^{-p_2 d} + \epsilon(A_1 - C_1) \right] e^{-i\zeta x} d\zeta, \end{aligned} \quad (26)$$

and,

$$\begin{aligned} \epsilon \int_{-\infty}^{\infty} \left\{ \left[C_{44} \left(-A_0 p_1^2 - S p_1 B_0 + \frac{S^2}{4} A_0 \right) \right. \right. \\ \left. \left. - i\zeta C_{46} \left(p_1 B_0 - \frac{S}{2} A_0 \right) - \frac{\mu_0}{\eta} (C_0 p_2^2 + 2p_2 e^{-p_2 d}) \right] f(x) \right. \\ \left. + \left[-C_{46} \left(p_1 B_0 - \frac{S}{2} A_0 \right) + i\zeta C_{66} A_0 \right. \right. \\ \left. \left. - i\zeta \frac{\mu_0}{\eta} \left(C_0 + \frac{2}{p_2} e^{-p_2 d} \right) \right] f'(x) \right\} e^{-i\zeta x} d\zeta \\ = - \int_{-\infty}^{\infty} \left[C_{44} \left(p_1 B_0 - \frac{S}{2} A_0 \right) + p_2 \frac{\mu_0}{\eta} C_0 - 2 \frac{\mu_0}{\eta} e^{-p_2 d} \right. \\ \left. + \epsilon \left(C_{44} p_1 B_1 - C_{44} \frac{S}{2} A_1 - i\zeta C_{46} A_1 + p_2 \frac{\mu_0}{\eta} C_1 \right) \right. \\ \left. - i\zeta C_{46} A_0 \right] e^{-i\zeta x} d\zeta, \end{aligned} \quad (27)$$

respectively.

DEVELOPMENT OF DISPERSION RELATION

To develop dispersion relation of SH-wave propagation in a monoclinic layer over a dry sandy half-space, we use Fourier and inverse Fourier transform of $f(x)$ defined as (Kreyszig, 2006)

$$\left. \begin{aligned} \bar{f}(\xi) &= \int_{-\infty}^{\infty} f(x) e^{i\xi x} dx, \\ f(x) &= \frac{1}{2\pi} \int_{-\infty}^{\infty} \bar{f}(\xi) e^{-i\xi x} d\xi. \end{aligned} \right\} \quad (28)$$

Applying the Fourier transform given in Eq. (28) to Eqs. (26) and (27), we get

$$\begin{aligned} \frac{\epsilon}{2\pi} \int_{-\infty}^{\infty} \int_{-\infty}^{\infty} \left(A_0 \frac{S}{2} - B_0 p_1 - C_0 p_2 \right. \\ \left. + 2e^{-dp_2} \right) \bar{f}(\xi) e^{-i(\zeta+\xi)x} d\xi d\zeta \\ = \int_{-\infty}^{\infty} \left[A_0 - C_0 - \frac{2}{p_2} e^{-p_2 d} \right. \\ \left. + \epsilon(A_1 - C_1) \right] e^{-i\zeta x} d\zeta, \end{aligned} \quad (29)$$

and,

$$\begin{aligned} \frac{\epsilon}{2\pi} \int_{-\infty}^{\infty} \int_{-\infty}^{\infty} \left\{ \left[C_{44} \left(-A_0 p_1^2 - S p_1 B_0 + \frac{S^2}{4} A_0 \right) \right. \right. \\ \left. \left. - i\zeta C_{46} \left(p_1 B_0 - \frac{S}{2} A_0 \right) - \frac{\mu_0}{\eta} (C_0 p_2^2 + 2p_2 e^{-p_2 d}) \right] \right. \\ \left. + \left[i\zeta C_{46} \left(p_1 B_0 - \frac{S}{2} A_0 \right) + \zeta \xi C_{66} A_0 \right. \right. \\ \left. \left. - \zeta \xi \frac{\mu_0}{\eta} \left(C_0 + \frac{2}{p_2} e^{-p_2 d} \right) \right] \right\} \bar{f}(\xi) e^{-i(\zeta+\xi)x} d\xi d\zeta \end{aligned}$$

$$\begin{aligned}
&= - \int_{-\infty}^{\infty} \left[C_{44} \left(p_1 B_0 - \frac{S}{2} A_0 \right) + p_2 \frac{\mu_0}{\eta} C_0 \right. \\
&\quad \left. - 2 \frac{\mu_0}{\eta} e^{-p_2 d} \right] \\
&\quad + \epsilon \left(C_{44} p_1 B_1 - C_{44} \frac{S}{2} A_1 - i\zeta C_{46} A_1 + p_2 \frac{\mu_0}{\eta} C_1 \right) \\
&\quad \left. - i\zeta C_{46} A_0 \right] e^{-i\zeta x} d\zeta, \quad (30)
\end{aligned}$$

respectively.

Taking $k = \zeta + \xi$ in the left-hand side of Eqs. (29) and (30) and treating ξ as constant we have $d\zeta = dk$. Substituting $\zeta = k$ in the right-hand side of Eqs. (29) and (30), we get

$$\epsilon R_1(k) = A_0 - C_0 - \frac{2}{p_2} e^{-p_2 d} + \epsilon(A_1 - C_1), \quad (31)$$

and,

$$\begin{aligned}
\epsilon R_2(k) = C_{44} \left(-p_1 B_0 + \frac{S}{2} A_0 - \epsilon p_1 B_1 + \frac{S}{2} \epsilon A_1 \right) \\
+ ik C_{46} (A_0 + \epsilon A_1) \\
+ \frac{\mu_0}{\eta} (2e^{-p_2 d} - p_2 C_0 - \epsilon p_2 C_1) \quad (32)
\end{aligned}$$

where,

$$\begin{aligned}
R_1(k) = \frac{1}{2\pi} \int_{-\infty}^{\infty} \left[\frac{S}{2} A_0 - p_1 B_0 - p_2 C_0 \right. \\
\left. + 2e^{-p_2 d} \right]^{\zeta=k-\xi} \bar{f}(\xi) e^{-i\xi x} d\xi \quad (33)
\end{aligned}$$

and,

$$\begin{aligned}
R_2(k) = \frac{1}{2\pi} \int_{-\infty}^{\infty} \left\{ C_{44} \left(-A_0 p_1^2 - s p_1 B_0 + \frac{S^2}{4} A_0 \right) \right. \\
- ik C_{46} \left(p_1 B_0 - \frac{S}{2} A_0 \right) \\
- \frac{\mu_0}{\eta} (C_0 p_2^2 + 2p_2 e^{-p_2 d}) \left. \right\} \\
+ \left\{ i\zeta C_{46} \left(p_1 B_0 - \frac{S}{2} A_0 \right) + k\zeta C_{66} A_0 \right. \\
\left. - k\zeta \frac{\mu_0}{\eta} \left(C_0 + \frac{2}{p_2} e^{-p_2 d} \right) \right\}^{\zeta=k-\xi} \bar{f}(\xi) e^{-i\xi x} d\xi \quad (34)
\end{aligned}$$

Equating the absolute terms and the coefficient of ϵ in Eqs. (25), (31) and (32), we get

$$\begin{aligned}
A_1 \left[C_{44} p_1 \sin p_1 H - C_{44} \frac{S}{2} \cos p_1 H - i\zeta C_{46} \cos p_1 H \right] \\
+ B_1 \left[C_{44} p_1 \cos p_1 H + C_{44} \frac{S}{2} \sin p_1 H + i\zeta C_{46} \sin p_1 H \right] \\
= 0, \quad (35)
\end{aligned}$$

$$\begin{aligned}
A_0 \left[C_{44} p_1 \sin p_1 H - C_{44} \frac{S}{2} \cos p_1 H - i\zeta C_{46} \cos p_1 H \right] \\
+ B_0 \left[C_{44} p_1 \cos p_1 H + C_{44} \frac{S}{2} \sin p_1 H + i\zeta C_{46} \sin p_1 H \right] \\
= 0, \quad (36)
\end{aligned}$$

$$A_1 - C_1 = R_1(k), \quad (37)$$

$$A_0 - C_0 = \frac{2}{p_2} e^{-p_2 d} \quad (38)$$

$$A_1 \left[\frac{S}{2} C_{44} + ik C_{46} \right] - p_1 C_{44} B_1 - \frac{\mu_0}{\eta} p_2 C_1 = R_2(k), \quad (39)$$

and,

$$\begin{aligned}
A_0 \left[\frac{S}{2} C_{44} + ik C_{46} \right] - p_1 C_{44} B_0 - \frac{\mu_0}{\eta} p_2 C_0 \\
= -2 \frac{\mu_0}{\eta} e^{-p_2 d}. \quad (40)
\end{aligned}$$

Solving Eqs. (35) to (40), we get

$$\begin{aligned}
A_0 = \frac{-8\mu_0 e^{-p_2 d}}{\eta \bar{R}_1(k)} (2p_1 C_{44} + s C_{44} \tan p_1 H \\
+ 2ik C_{46} \tan p_1 H) \quad (41)
\end{aligned}$$

$$\begin{aligned}
B_0 = \frac{8\mu_0 e^{-p_2 d}}{\eta \bar{R}(k)} (2p_1 C_{44} \tan p_1 H - s C_{44} \\
- 2ik C_{46}) \quad (42)
\end{aligned}$$

$$\begin{aligned}
C_0 = -\frac{2e^{-p_2 d}}{p_2 \bar{R}(k)} \left(4 \frac{\mu_0}{\eta} p_2 p_1 C_{44} + 2 \frac{\mu_0}{\eta} p_2 s C_{44} \tan p_1 H \right. \\
+ 4ik \frac{\mu_0}{\eta} p_2 C_{46} \tan p_1 \\
+ 4iks C_{44} C_{46} \tan p_1 H - 4k^2 C_{46}^2 \tan p_1 H \\
+ C_{44}^2 s^2 \tan p_1 H \\
\left. + 4p_1^2 C_{44}^2 \tan p_1 H \right) \quad (43)
\end{aligned}$$

$$A_1 = -\frac{2(\mu_0 p_2 R_1 - R_2)}{\eta \bar{R}(k)} (2p_1 C_{44} + s C_{44} \tan p_1 H + 2ik C_{46} \tan p_1 H),$$

$$B_1 = \frac{2(\mu_0 p_2 R_1 - R_2)}{\eta \bar{R}(k)} (2p_1 C_{44} \tan p_1 H - s C_{44} - 2ik C_{46}),$$

$$\begin{aligned}
C_1 = \frac{1}{\bar{R}(k)} (4p_1 C_{44} R_2 + 2s C_{44} R_2 \tan p_1 H + \\
4ik C_{46} R_2 \tan p_1 H - 4iks C_{44} C_{46} R_1 \tan p_1 H \\
+ 4k^2 C_{46}^2 R_1 \tan p_1 H - \\
s^2 C_{44}^2 R_1 \tan p_1 H - \\
4p_1^2 C_{44}^2 R_1 \tan p_1 H) \quad (46)
\end{aligned}$$

where,

$$\begin{aligned}
\bar{R}(k) = 4iks C_{44} C_{46} \tan p_1 H - 4k^2 C_{46}^2 \tan p_1 H \\
- 4ik p_2 \frac{\mu_0}{\eta} C_{46} \tan p_1 H + s^2 C_{44}^2 \tan p_1 H \\
- 2 \frac{\mu_0}{\eta} p_2 s C_{44} \tan p_1 H - 4 \frac{\mu_0}{\eta} p_2 p_1 C_{44} \\
+ 4p_1^2 C_{44}^2 \tan p_1 H. \quad (47)
\end{aligned}$$

Therefore, the displacement of SH-wave in M_1 layer is given by

$$V_1 = -\frac{1}{2\pi} \int_{-\infty}^{\infty} \frac{8\mu_0 e^{-p_2 d} e^{-\frac{s}{2}z}}{\eta \bar{R}(k)} \left[1 + \frac{\epsilon \left(\frac{\mu_0}{\eta} p_2 R_1 - R_2 \right) e^{p_2 d}}{4 \frac{\mu_0}{\eta}} \right] N e^{-ikx} dk, \quad (48)$$

where,

$$N = [\cos p_1 z (2p_1 C_{44} + s C_{44} \tan p_1 H + 2ik C_{46} \tan p_1 H) + \sin p_1 z (2ik C_{46} + s C_{44} - 2p_1 C_{44} \tan p_1 H)].$$

The Fourier transform of Eq. (1) representing the triangular irregularity at the interface is given by

$$\bar{f}(\xi) = \frac{h}{\epsilon} \int_{-a}^a \left(1 - \frac{|x|}{a} \right) e^{i\xi x} dx$$

which on solving gives,

$$\bar{f}(\xi) = \frac{4(1 - \cos(\xi a))}{\xi^2}. \quad (49)$$

Using Eq. (49) in Eqs. (33) and (34), we get

$$\frac{\mu_0}{\eta} p_2 R_1 - R_2 = \frac{4\mu_0}{\eta\pi} \int_{-\infty}^{\infty} [\phi(k - \xi) + \phi(k + \xi)] \frac{(1 - \cos(\xi a))}{\xi^2} d\xi \quad (50)$$

where,

$$\begin{aligned} \phi(k - \xi) = & \left[-2C_{44}^2 s^2 p_1 p_2 - 8p_1^3 C_{44} p_2 + 2p_2^2 \bar{R}(k) \right. \\ & - 2s^2 \frac{\mu_0}{\eta} p_2^2 C_{44} \tan p_1 H \\ & - 4iks C_{46} \frac{\mu_0}{\eta} p_2^2 \tan p_1 H - 8C_{44} p_1^2 \frac{\mu_0}{\eta} p_2^2 \tan p_1 H \\ & + 4p_1^2 s C_{44}^2 p_2 \tan p_1 H \\ & + 8ik C_{46} p_1 \frac{\mu_0}{\eta} p_2^2 - 8ik C_{46} C_{44} s p_1 p_2 \\ & + 4ik C_{46} C_{44} s^2 p_2 \tan p_1 H \\ & + s^3 C_{44}^2 p_2 \tan p_1 H \\ & - 8k\xi C_{46}^2 p_1 p_2 + 4\xi k C_{46}^2 p_2 \tan p_1 H \\ & + 8ik^2 \xi C_{46} C_{66} p_2 \tan p_1 H \\ & + 8k\xi C_{66} C_{44} p_1 p_2 \\ & + 4k\xi s p_2 C_{66} C_{44} \tan p_1 H - 4ik^2 \xi \frac{\mu_0}{\eta} p_2 C_{46} \tan p_1 H \\ & - 2k\xi s \frac{\mu_0}{\eta} p_2 C_{44} \tan p_1 H \\ & - 4k\xi \frac{\mu_0}{\eta} p_2 p_1 C_{44} - 4ik^2 \xi s C_{44} C_{46} \tan p_1 H \\ & \left. + \xi k \bar{R}(k) - 4k\xi p_1^2 C_{44}^2 \tan p_1 H \right] \end{aligned} \quad (51)$$

$$\begin{aligned} & -C_{44}^2 s^2 k\xi \tan p_1 H + 4k^3 \xi C_{46}^2 \tan p_1 H \\ & - 4k^2 s p_2 C_{46}^2 \tan p_1 H \\ & - 2is^2 p_2 \xi C_{46} C_{44} \tan p_1 H + 8k^2 p_1 p_2 C_{46}^2 \\ & - 8i\xi C_{46} C_{44} p_1^2 p_2 \tan p_1 H \left] \frac{e^{-p_2 d}}{p_2 \bar{R}(k)} \right]_{\xi=k-\xi}^{\xi=k+\xi}. \end{aligned}$$

Using the asymptotic formula (Willis, 1948; Tranter, 1966), we have

$$\int_{-\infty}^{\infty} [\phi(k - \xi) + \phi(k + \xi)] \frac{(1 - \cos(\xi a))}{\xi^2} d\xi \cong 2\pi a \phi(k). \quad (52)$$

Using Eq. (52) in Eq. (50), we get

$$\epsilon \frac{\frac{\mu_0}{\eta} p_2 R_1 - R_2}{4 \frac{\mu_0}{\eta}} = h \phi(k). \quad (53)$$

Using Eq. (53) in Eq. (48), the displacement in the monoclinic layer reduces to

$$\begin{aligned} V_1 = & -\frac{1}{2\pi} \int_{-\infty}^{\infty} \frac{8\mu_0 e^{-p_2 d} e^{-\frac{s}{2}z}}{\eta \bar{R}(k)} [1 + h\phi(k) e^{p_2 d}] N e^{-ikx} dk \\ = & -\frac{1}{2\pi} \int_{-\infty}^{\infty} \frac{8\mu_0 e^{-p_2 d} e^{-\frac{s}{2}z}}{\eta \bar{R}(k) [1 - h\phi(k) e^{p_2 d}]} N e^{-ikx} dk. \end{aligned} \quad (54)$$

The contribution to the displacement due to dispersion is obtained from the singularities of the integrand of Eq. (54). Thus, the dispersion relation for SH-waves is (Kalyani and Kar, 1986)

$$\begin{aligned} & \bar{R}(k) [1 - h\phi(k) e^{p_2 d}] \\ & = 0. \end{aligned} \quad (55)$$

Substituting $\bar{R}(k)$ and $\phi(k)$ from Eqs. (47) and (51), respectively in Eq. (55), we get

$$\begin{aligned} & 4ik C_{44} C_{46} s p_2 \tan p_1 H - 4k^2 p_2 C_{46}^2 p_2 \tan p_1 H \\ & - 4ik C_{46} p_2^2 \frac{\mu_0}{\eta} \tan p_1 H \\ & + C_{44}^2 s^2 p_2 \tan p_1 H - 2 \frac{\mu_0}{\eta} p_2^2 s C_{44} \tan p_1 H - 4 \frac{\mu_0}{\eta} p_2^2 p_1 C_{44} \\ & + 4C_{44}^2 p_1^2 p_2 \tan p_1 H \\ & - h[-2C_{44}^2 s^2 p_1 p_2 - 8p_1^3 C_{44} p_2 + 2p_2^2 \bar{R}(k) - 2s^2 \frac{\mu_0}{\eta} p_2^2 C_{44} \tan p_1 H \\ & - 4iks C_{46} \frac{\mu_0}{\eta} p_2^2 \tan p_1 H - 8C_{44} p_1^2 \frac{\mu_0}{\eta} p_2^2 \tan p_1 H \\ & + 4p_1^2 s C_{44}^2 p_2 \tan p_1 H \\ & + 8ik C_{46} p_1 \frac{\mu_0}{\eta} p_2^2 - 8ik C_{46} C_{44} s p_1 p_2 + 4ik C_{46} C_{44} s^2 p_2 \tan p_1 H \\ & + s^3 C_{44}^2 p_2 \tan p_1 H - 4k^2 s p_2 C_{46}^2 \tan p_1 H + 8k^2 C_{46}^2 p_1 p_2] = 0 \end{aligned} \quad (56)$$

If c denotes the wave velocity of SH-waves propagating along the interface, using Eqs. (12) and (19), we have

$$p_1 = \sqrt{\frac{\omega^2}{\beta_1^2} - \zeta^2 \frac{C_{66}}{C_{44}} + \zeta^2 \frac{C_{46}^2}{C_{44}^2}}, \quad s = -\frac{2i\zeta C_{46}}{C_{44}}, \quad p_2 = \sqrt{\zeta^2 - \eta \frac{\omega^2}{\beta_2'^2}},$$

then, by replacing ζ with k and ω with ck , we obtain

$$p_1 = kP_1, \quad s = kS, \quad p_2 = kP_2$$

where

$$P_1 = \sqrt{\frac{c^2}{\beta_1^2} - \frac{C_{66}}{C_{44}} + \frac{C_{46}^2}{C_{44}^2}}, \quad S = -\frac{2iC_{46}}{C_{44}}, \quad P_2 = \sqrt{1 - \eta \frac{c^2}{\beta_2'^2}}.$$

Solving Eq. (56), we get

$$\tan \left(kH \sqrt{\frac{c^2}{\beta_1^2} - \frac{C_{66}}{C_{44}} + \frac{C_{46}^2}{C_{44}^2}} \right) = \frac{D_1}{D_2} + i \frac{D_3}{D_4}, \quad (57)$$

where,

$$\begin{aligned} D_1 &= \left(\frac{\mu_0}{\eta} P_2 C_{44} - 2hk C_{44}^2 P_1^2 - 2hk \frac{\mu_0}{\eta} C_{44} P_2 \right) \left(C_{44}^2 - 2hk C_{44}^2 P_2 \right. \\ &\quad \left. + 2hk C_{44} \frac{\mu_0}{\eta} P_2 \right) + 4h^2 k^2 P_2 \frac{\mu_0}{\eta} C_{46}^2 C_{44} \\ D_2 &= P_1 \left(C_{44}^2 - 2hk C_{44}^2 P_2 + 2hk C_{44} \frac{\mu_0}{\eta} P_2 \right)^2 + 4h^2 k^2 P_1 C_{46}^2 C_{44}^2 \\ D_3 &= 2hk C_{46} \frac{\mu_0}{\eta} P_2 \left(C_{44}^2 - 2hk C_{44}^2 P_2 + 2hk C_{44} \frac{\mu_0}{\eta} P_2 \right) \\ &\quad - 2hk C_{44} C_{46} \left(\frac{\mu_0}{\eta} P_2 C_{44} - 2hk C_{44}^2 P_1^2 \right. \\ &\quad \left. - 2hk \frac{\mu_0}{\eta} C_{44} P_2 \right) \\ D_4 &= P_1 \left(C_{44}^2 - 2hk C_{44}^2 P_2 + 2hk C_{44} \frac{\mu_0}{\eta} P_2 \right)^2 + \\ &\quad 4h^2 k^2 P_1 C_{46}^2 C_{44}^2. \end{aligned}$$

We now equate the real and imaginary parts on both sides of Eq. (57). We observe that the imaginary part gives $D_3 = 0$, which does not result in the dispersion relation for the governing equation of SH-waves. However, the real part gives the dispersion relation for SH-waves propagating in a monoclinic layer overlying a dry sandy half-space with a triangular irregularity at the interface is given by:

$$\tan \left(kH \sqrt{\frac{c^2}{\beta_1^2} - \frac{C_{66}}{C_{44}} + \frac{C_{46}^2}{C_{44}^2}} \right) = \frac{\left(\frac{\mu_0}{\eta} P_2 C_{44} - 2hk C_{44}^2 P_1^2 - 2hk \frac{\mu_0}{\eta} C_{44} P_2 \right) \left(C_{44}^2 - 2hk C_{44}^2 P_2 + 2hk C_{44} \frac{\mu_0}{\eta} P_2 \right) + 4h^2 k^2 P_2 \frac{\mu_0}{\eta} C_{46}^2 C_{44}^2}{P_1 \left(C_{44}^2 - 2hk C_{44}^2 P_2 + 2hk C_{44} \frac{\mu_0}{\eta} P_2 \right)^2 + 4h^2 k^2 P_1 C_{46}^2 C_{44}^2} \quad (58)$$

For the existence of pure SH-waves, we consider the range of the dimensionless phase velocity (c/β_1) in Eq. (58) as

$$\sqrt{\frac{C_{66}}{C_{44}} - \frac{C_{46}^2}{C_{44}^2}} < \frac{c}{\beta_1} < \frac{\beta_2'}{\beta_1}.$$

SH-wave propagation in an isotropic layer

From the developed Eq. (58), SH-wave propagation in an isotropic layer overlying an isotropic half-space can be deduced by assuming

$$C_{44} = C_{66} = \mu, \quad C_{46} = 0, \quad \eta = 1, \quad \text{and} \quad h/H = 0.$$

Thus, Eq. (58) reduces to

$$\tan \left(kH \sqrt{\frac{c^2}{\beta_1^2} - 1} \right) = \frac{\mu_0 \sqrt{1 - \frac{c^2}{\beta_2'^2}}}{\mu \sqrt{\frac{c^2}{\beta_1^2} - 1}} \quad (59)$$

Eq. (59) closely matches the well-known established dispersion equation in an isotropic layer overlying isotropic half-space given by Ewing et al. (1957).

NUMERICAL CALCULATION

Having developed the dispersion relation, the effect of triangular irregularity at the interface when the layer is either isotropic or monoclinic and the half-space is with or without sandiness, which have strong influence on the dispersion of the SH-waves, has been studied using the following data (Gubbins, 1990; Pradhan et al., 2023; Madan et al., 2023a)

$$\begin{aligned} C_{44} &= 9.4 \times 10^{10} \text{ N/m}^2, & C_{46} &= -1.1 \times 10^{10} \text{ N/m}^2, \\ C_{66} &= 9.3 \times 10^{10} \text{ N/m}^2, & \mu_0 &= 6.54 \times 10^{10} \text{ N/m}^2, \\ \rho_1 &= 7450 \text{ kg/m}^3, & \rho_2 &= 3409 \text{ kg/m}^3. \end{aligned}$$

The results obtained are illustrated graphically in Figures 2-4.

Figure 2 illustrates the dependence of phase velocity (c/β_1) on wave number (kH) in absence of both sandiness ($\eta = 1$) in the half-space and irregularity ($h/H = 0$) at the interface, revealing that the phase velocity decreases as the medium of the layer changes from isotropic to monoclinic, showing the influence of monoclinic symmetry (Thomsen, 1986) on wave behaviour and validating the model by comparing it with isotropic results.

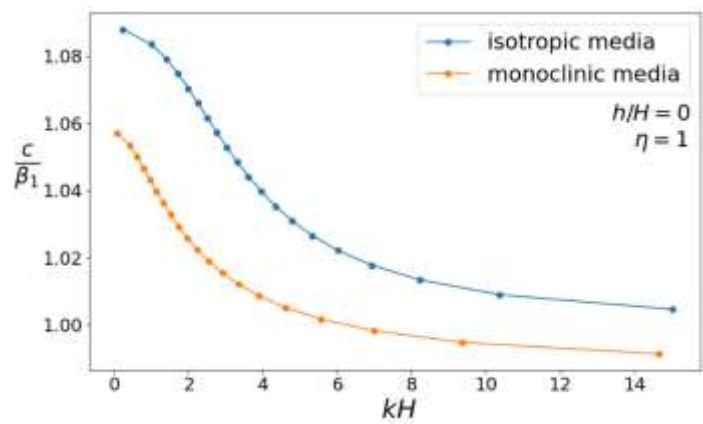


Figure 2. Phase velocity (c/β_1) versus wave number (kH)

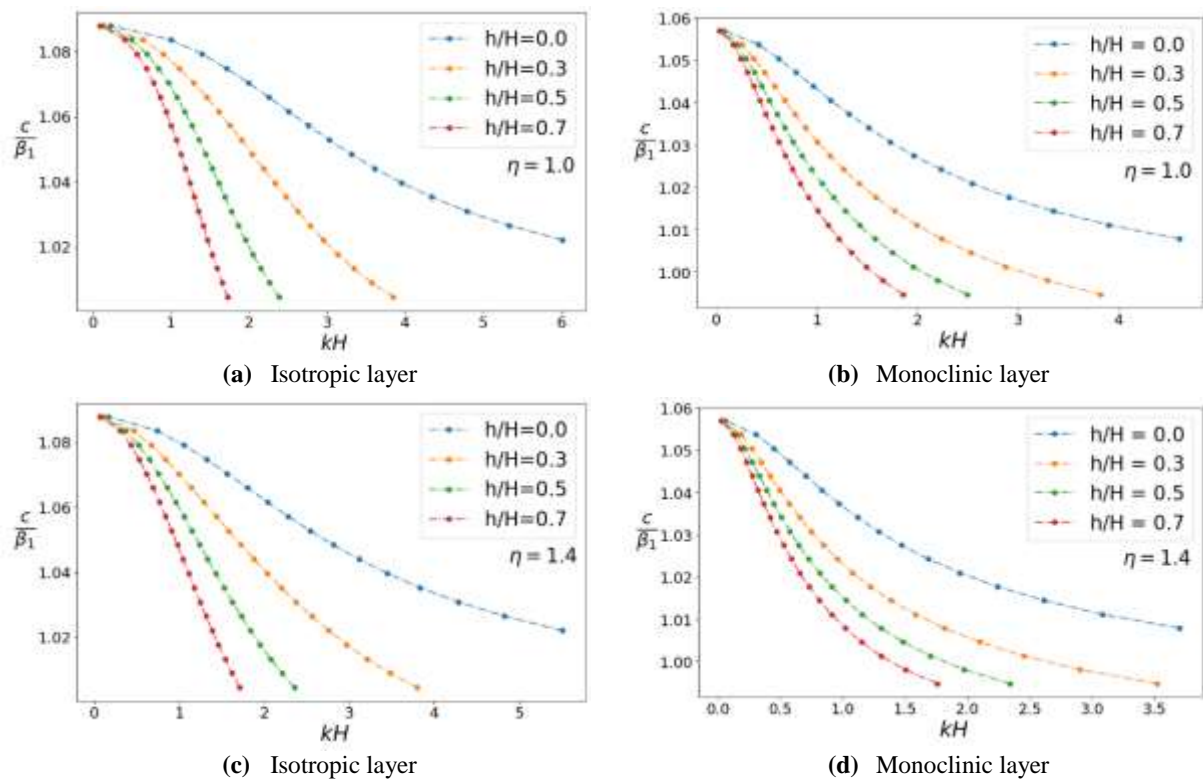


Figure 3. Effect of triangular irregularity, when the layer is (i) isotropic (a, c), and (ii) monoclinic (b, d)

Table 2. Variation of phase velocity with depth of triangular irregularity for isotropic and monoclinic media

Depth of triangular irregularity	$\eta = 1, kH = 1$		$\eta = 1.4, kH = 1$	
	c/β_1 in isotropic medium	c/β_1 in monoclinic medium	c/β_1 in isotropic medium	c/β_1 in monoclinic medium
$h/H = 0$	1.083	1.043	1.088	1.037
$h/H = 0.3$	1.077	1.030	1.070	1.023
$h/H = 0.5$	1.069	1.022	1.060	1.015
$h/H = 0.7$	1.058	1.014	1.047	1.008

In the absence of sandiness ($\eta = 1$) in the half-space, Figures 3(a) and 3(b) depict the variation in phase velocity with wave number in isotropic and monoclinic media respectively for different values of the depth of triangular irregularity. From these figures, it is observed that the phase velocity decreases as the depth of triangular irregularity increases in both media, which is consistent with the observations by Chattopadhyay et al. (2008) and Madan et al. (2024), where similar results were observed. Further, in the presence of sandiness ($\eta = 1.4$), Figures 3(c) and 3(d) depict the variation in phase velocity with wave number in isotropic and monoclinic media, respectively, for different values of the depth of triangular irregularity. Similar trends of decreasing phase velocity with increasing depth of triangular irregularity are observed in these figures. Moreover, it is noteworthy from Table 2 that when the layer changes from isotropic to monoclinic, the phase velocity decreases by approximately 4% in both the presence and absence of sandiness.

Figures 4(a) and 4(b) depict the variation of dimensionless phase velocity with dimensionless wave number for isotropic and monoclinic media, respectively, without irregularity at the interface ($h/H = 0$). These figures indicate that as the sandiness parameter increases from $\eta = 1$ to $\eta = 1.4$, the phase velocity decreases for both media. It is also observed from Table 3 that, at kH equals to 4, the phase velocity decreases as the medium of the layer changes from isotropic to monoclinic.

Further, in the presence of a triangular irregularity ($h/H = 0.4$) and the layer is either isotropic or monoclinic, it is observed from Figures 4(c) and 4(d) that the phase velocity decreases as the wave number increases for all values of the sandiness parameter. From Table 3, similar trends are also observed at kH equals to 1.5, where the phase velocity in the monoclinic medium is lower than that in the isotropic medium.

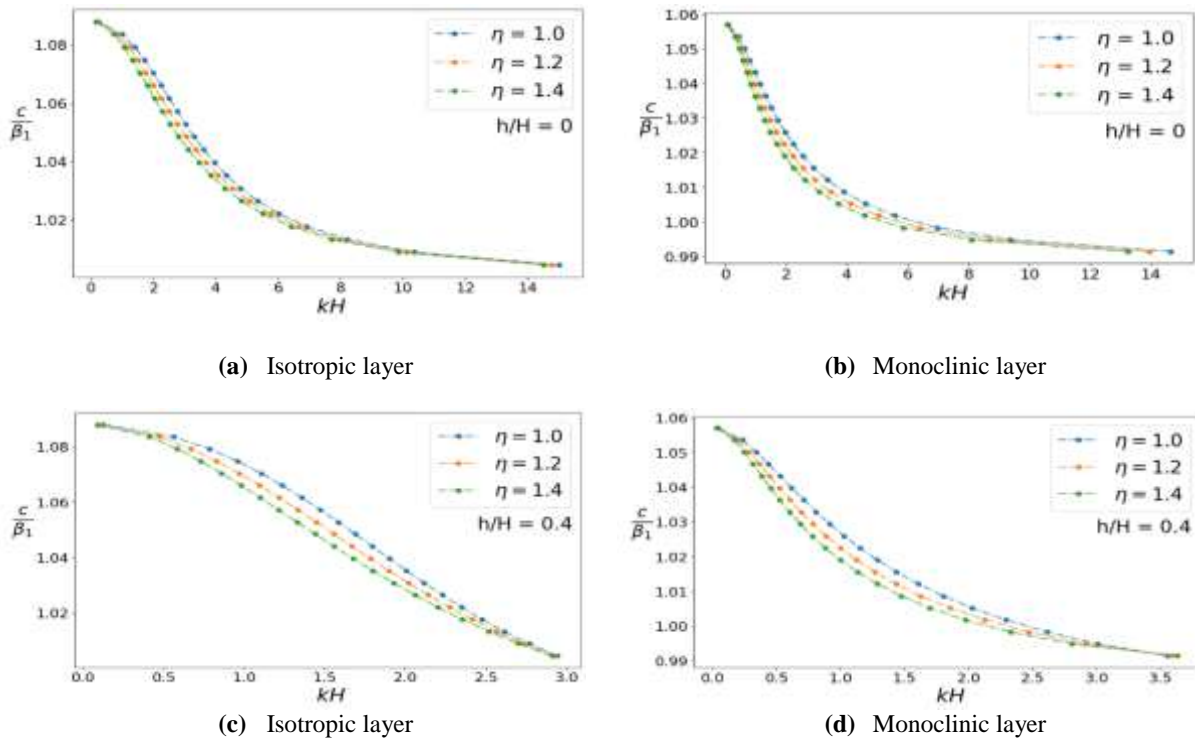


Figure 4. Effect of sandiness, when the layer is (i) isotropic (a, c), and (ii) monoclinic (b, d)

Table 3. Variation of phase velocity with sandiness parameter for isotropic and monoclinic media

Sandiness parameter	$h/H = 0, kH = 4$		$h/H = 0.4, kH = 1.5$	
	c/β_1 in isotropic medium	c/β_1 in monoclinic medium	c/β_1 in isotropic medium	c/β_1 in monoclinic medium
$\eta = 1$	1.039	1.008	1.056	1.014
$\eta = 1.2$	1.036	1.006	1.050	1.010
$\eta = 1.4$	1.033	1.004	1.046	1.008

CONCLUSIONS

This study investigates the influence of a triangular irregularity on the dispersion characteristics of SH-waves propagating in a monoclinic crustal layer overlying a dry sandy half-space. The analysis considers variations in sandiness in the half-space and in the depth of interface irregularity. Further, monoclinic and isotropic media are compared to show the impact of symmetry on wave behaviour and validate the developed model in the present study. Our findings enhance the understanding of SH-wave propagation in complex geological settings and offer practical implications for geophysical exploration and engineering applications involving layered, anisotropic, and heterogeneous subsurface structures. The highlights of the findings of this study are given below:

1. SH-waves exhibit dispersive behaviour in the monoclinic medium, as the phase velocity varies with wave number and converges at different values depending on the material properties.
2. The phase velocity of SH-waves is hindered in the monoclinic medium, showing a decreasing trend with increasing wave number.
3. The transition of the layer medium from isotropic to monoclinic, results in a consistent decrease in phase velocity regardless of the presence of sandiness or interface irregularity.
4. An increase in the depth of triangular irregularity at the interface leads to a reduction in phase velocity for both isotropic and monoclinic media, independent of the sandiness in the half-space.
5. An increase in the sandiness parameter of the half-space reduces the phase velocity in both types of media, irrespective of whether the interface is smooth or irregular.

ACKNOWLEDGMENT

The author, Tanishqa Shivaji Veer, gratefully acknowledges the financial assistance provided by Dr. Vishwanath Karad MIT World Peace University, Pune-411038, Maharashtra, India, through a Junior Research Fellowship. The authors express their gratitude to Dr. O. P. Pandey, the Chief Editor, for his insightful feedback and for editing the final manuscript. The authors are also thankful to reviewers for their comments and suggestions in the improvement of the manuscript.

Author Credit Statement

All authors have contributed equally. All authors have read and approved the manuscript.

Data availability

No data were used in this study.

Compliance with ethical standards

Authors declare no conflict of interest and adhere to copyright norms.

REFERENCES

- Acharya, D. P. and Roy, I., 2009. Effect of surface stress and irregularity of the interface on the propagation of SH-waves in the magneto-elastic crustal layer based on a solid semi space. *Sādhanā*, 34, 309-330.
- Chattopadhyay, A., 1975. On the dispersion equation for Love waves due to irregularity in the thickness of the non-homogeneous crustal layer. *Acta Geophys. Polonica*, 23, 307-317.
- Chattopadhyay, A. and De, R. K., 1983. Love type waves in a porous layer with irregular interface. *Int. J. Eng. Sci.*, 21(11), 1295-1303.
- Chattopadhyay, A. and Saha, S., 1996. Reflection and refraction of P waves at the interface of two monoclinic media. *Int. J. Eng. Sci.*, 34(11), 1271-1284.
- Chattopadhyay, A., Gupta, S., Sharma, V. K. and Kumari, P., 2008. Propagation of SH waves in an irregular monoclinic crustal layer. *Arch. Appl. Mech.*, 78, 989-999.
- Ewing, M., Jardetzky, W. and Press, F., 1957. *Elastic Waves in Layered Media*. McGraw-Hill, New York.
- Gubbins, D. 1990., *Seismology and plate tectonics*. Cambridge University Press, Cambridge.
- Gupta, S., Das, S. K. and Pramanik, S., 2021. Impact of irregularity, initial stress, porosity, and corrugation on the propagation of SH wave. *Int. J. Geomech.*, 21(2), 04020245.
- Kalyani, V. K. and Kar, B. K., 1986. Propagation of Love waves in an irregular anisotropic porous layer sandwiched between two homogeneous half-spaces. *Gerlands Beilr. Geophys.*, 95(1), 27-35.
- Kalyani, V. K., Sinha, A., Pallavika, Chakraborty, S. K. and Mahanti, N. C., 2008. Finite difference modeling of seismic wave propagation in monoclinic media. *Acta Geophys.*, 56, 1074-1089.
- Kar, B. K., Pal, A. K. and Kalyani, V. K., 1986. Propagation of Love waves in an irregular dry sandy layer. *Acta Geophys. Polonica*, 34(2), 157-170.
- Kaur, J. and Tomar, S. K., 2004. Reflection and refraction of SH-waves at a corrugated interface between two monoclinic elastic half-spaces. *Int. J. Numer. Anal. Methods Geomech.*, 28(15), 1543-1575.
- Khan, A. A., Dilshad, A., Rahimi-Gorji, M. and Alam, M. M., 2021. Effect of initial stress on an SH wave in a monoclinic layer over a heterogeneous monoclinic half-space. *Math.*, 9(24), 3243.
- Kreyszig, E., 2006. *Advanced Engineering Mathematics*. John Wiley and Sons, New Jersey, 9th edition.
- Kumar, N. and Madan, D. K., 2022. Propagation of love waves in dry sandy medium laying over orthotropic semi-infinite medium with irregular interface. *AIP Conf. Proc.*, 2481(1), 040019.
- Kumar, R., Madan, D. K. and Sikka, J. S., 2015. Effect of irregularity and inhomogeneity on the propagation of Love waves in fluid saturated porous isotropic layer. *J. Appl. Sci. Techno.*, 20, 16-21.
- Madan, D. K., Kumar, N. and Goyal, R., 2023a. SH wave propagation in dry sandy media overlying an orthotropic elastic layer and a pre-stressed dry sandy half-space. *Punjab Univ. J. Math.*, 55(8), 327-342.
- Madan, D. K., Kumar, N. and Rani, A. 2023b. Rayleigh wave propagation in isotropic sandy layer sliding over isotropic

- sandy semi-infinite medium with sliding contact. *Int. J. Appl. Mech. Eng.*, 28(1), 58-70.
- Madan, D. K., Kumar, N. and Muwal, R. 2024., Dispersion of Love wave in a viscoelastic sandy layer overlying anisotropic half-space with parabolic interface. *Jñānābha*, 54(1), 244-253.
- Nye, J. F., 1985. *Physical Properties of Crystals: Their Representation by Tensors and Matrices*. Oxford University Press, Oxford, New York.
- Pal, A. K., 1985. The propagation of Love waves in a dry sandy layer. *Acta Geophys. Polonica*, 33(2), 183-188.
- Pal, P., Majhi, S. and Kumar, S., 2016. Propagation of SH-waves in a sandwiched dry sandy medium. *Conference GSI*, 70-73.
- Pilant, W. L., 1979. *Elastic Waves in the Earth (Developments in Solid Earth Geophysics)*. Elsevier, Holland.
- Pradhan, N., Manna, S. and Samal, S. K., 2023. SH-type wave motion in a geophysical model with monoclinic and heterogeneous media due to a point source at the interface. *Arch. Appl. Mech.*, 93, 2613-2629.
- Pradhan, N., Manna, S., Samal, S. K. and Saha, S., 2025. SH-wave in two-layered structure of functionally graded viscoelastic and monoclinic media under the influence of an interior point source. *Eur. Phys. J. Plus*, 140, 181.
- Sethi, M. and Sharma, A., 2016. Propagation of SH waves in a regular non-homogeneous monoclinic crustal layer lying over a non-homogeneous semi-infinite medium. *Int. J. Appl. Mech. Eng.*, 21(2), 447-459.
- Thomsen, L., 1986. Weak elastic anisotropy. *Geophys.*, 51(10), 1954-1966.
- Tomar, S. K. and Kaur, J., 2007. SH-waves at a corrugated interface between a dry sandy half space and an anisotropic elastic half-space. *Acta Mech.*, 190, 1-28.
- Tranter, C. J., 1966. *Integral Transform in Mathematical Physics*. Methuen and Co. Ltd., London.
- Willis, H. F., 1948. LV. A formula for expanding an integral as a series. *London Edinburgh Philos. Mag. & J. Sci.*, 39(293), 455-459.

Received on: 25-06-2025; Revised on: 19-08-2025; Accepted on: 21-08-2025

Future projections of land evapotranspiration over India: Insights from Multi-Model CMIP6 under SSP2-4.5 and SSP5-8.5

Garima Singh, Harshita Saxena* and Sudhir Kumar Singh

K. Banerjee Centre of Atmospheric and Ocean Studies, University of Allahabad, Prayagraj-211002 (Uttar Pradesh), India

*Corresponding author: saxenacaet@gmail.com

ABSTRACT

Evapotranspiration (ET) is a key water cycle process, linking hydrology and land surface energy balance. This study examines future ET changes using CMIP6 under moderate (SSP2-4.5) and extreme (SSP5-8.5) scenarios for the mid-future (2040-2069) and far-future (2070-2099) relative to the reference period (1985-2014). ET is projected to increase across all the models; however, the magnitude varies across models and regions. Notably, this increase in ET further intensifies in SSP5-8.5 compared to SSP2-4.5. These changes also exhibit seasonal variability, with the monsoon season showing the most significant alterations. Notably, the largest inter-model variability is observed over central India, particularly under the SSP2-4.5 scenario, although some models project localized decreases. Monsoon season has enhanced the ensemble mean of ET variability for the studied CMIP6 models, indicating more precipitation and land-atmosphere interaction. This variability underscores the complexity of climate change impacts, driven by regional differences in climatic responses and model-specific uncertainties.

Key words: Evapotranspiration, CMIP6 models, Emission scenario, Future projections, Climate change.

INTRODUCTION

Global warming is considered to increase worldwide threatening climate change (Rawat et al., 2024). The Intergovernmental Panel on Climate Change (IPCC) estimates report the increase of global mean temperature by 0.2 ± 0.1 °C every decade (Stocker et al., 2013). Climate change is currently a stark actuality that affects the biophysical systems and disturbs socioeconomic development all around. Precipitation, temperature, and evapotranspiration (ET), are the key factors influencing regional surface temperatures (Mondal et al., 2021). Precipitation and ET drive the environmental water cycle of a specific region, where ET is considered as one of the primary components of the water cycle (Wang et al., 2021).

ET is the combined water loss from plant transpiration and surface evaporation (Kumar et al., 2023), encompassing soil and aquatic environments, that are essential for assessing global changes (Allen et al., 1998; Cook et al., 2014). The processes that regulate ET primarily link the energy and moisture flux in the Earth system (Wang et al., 2021). These connections make ET a significant fluctuation in both prolonged climate projections and brief quantitative meteorological predictions. Either directly or indirectly, climate change influences the hydrological cycle and alterations in water balance aspects (Mondal and Majumdar, 2015). Therefore, the regular occurrence of excessive weather probability, resulting from climate change, makes sustainable and effective water management essential everywhere. A fundamental factor of the hydrological cycle and degrees of water accessibility is potential evapotranspiration (PET) (Abdallah et al., 2025). Thus, appropriate water resource management depends on ET forecasts under scenarios of climate change (Aragón-Hernández et al., 2024). The hydrological process dictates farming methods and the needs

for irrigation water balance (Singh et al., 2021), which subsequently determine the sustainability of the environment, making ET a crucial factor (Mahanta et al., 2024). Furthermore, ET is a crucial indicator of ecosystem sustainability on several scales (Wang et al., 2021). However, the complex interactions between soil, plant, and atmosphere involve ET as a component (Cook et al., 2014; Mondal and Majumdar, 2015). Researchers often use process-based land surface models to simulate ET, yet they may be vulnerable to ill-posed presumptions, unpredictability, and costly computing expenses (Long et al., 2014). Accurate assessment of land surface ET is crucial for improving forecasts and understanding hydroclimatic changes and sustainability in a changing global context (Kim and Hogue, 2008; Singh et al., 2022).

Transpiration (T_v) is the most uncertain ET component, influenced by weather, soil moisture, and plant physiology (Pan et al., 2020). Consequently, the global transpiration-to-ET ratio (T_v/ET) remains a debated topic (Lian et al., 2018). Lian et al. (2018) found that virtually Earth System Models underestimate the global ET ratio. More recently, investigations on worldwide ET revealed that it has generally increased during the 1980s (Zeng et al., 2012; Yao et al., 2016; Zhang et al., 2016). Evaporation has decreased globally throughout the last half-century (Fu et al., 2009; Peterson et al., 1995). This implies an increase in actual ET. Future predictions rely upon an awareness of the uncertainty in worldwide terrestrial ET estimations from several sources (Zhang et al., 2016; Kim et al., 2021; Mondal et al., 2021).

Many researchers have lately compared numerous terrestrial ET estimations worldwide (Mueller et al., 2013; Zhang et al., 2016; Liu et al., 2020; Kim et al., 2021; Lu et al., 2021; Mondal et al., 2021; Nooni et al., 2021; Wang et al., 2021; Song et al., 2022; Yahaya et al., 2024). Researchers have improved

geographical assessments on the management of water resources and the implementation regarding guidelines supporting agricultural sustainability which depend on evaluation of ET change, primarily in arid conditions areas of a heated planet (Stocker et al., 2013; Niang et al., 2014). We expect rising ET will result in an increase in the frequency and severity of meteorological phenomena, including droughts, floods, and heatwaves. Understanding future climate under global warming is crucial for responding to its impacts (Arnell and Lloyd-Hughes, 2014). The CMIP framework serves as a collaborative tool for research, designed to enable our knowledge of the physical climatic reaction to predicted emissions in the warming context (Covey et al., 2003; Meehl et al., 2005; Taylor et al., 2012; Eyring et al., 2016). The CMIP6 included several climate models, but the models' performance in calculating ET remains unknown. The World Climate Research Program (WCRP) directed CMIP, which provided the opportunity to consolidate several Land Surface Models (LSMs) for hydrological investigations. Climate models exhibit substantial uncertainty in simulating land-atmosphere fluxes, including ET, due to the complex interactions at the land-atmosphere interface, limited historical observations, and varying approaches to representing land surface processes (Mueller and Seneviratne,

2014). Comprehensive observations of the various ET components are not readily available; hence, a significant obstacle to such an evaluation is the segmentation of ET at the regional level, which is not precisely known.

This study uses CMIP6 models to examine ET partitioning in modern climate simulations (Eyring et al., 2016; Checa-Garcia et al., 2018). Still, methodological uncertainty influences such observations, which are rare for now. We also investigate potential relationships between overall predicted climate in these models and the dispersion of ET and evaluate the potential developments in models of partitioning. We have conducted a unique investigation across homogenous regions of India to identify uncertainties in various techniques' estimations. In this work, we have investigated the ET variability and trends within the studied area using fifteen models of the CMIP6 under SSP5-8.5 and SSP2-4.5. Future climate projections in CMIP6 are shaped by advancements in emissions modeling, land use scenarios, and physical process representations based on SSPs (Eyring et al., 2016; O'Neill et al., 2017; Riahi et al., 2017). The primary motivation for this work is a thorough assessment of historical and future prospects in ET, which has not previously been conducted over India.

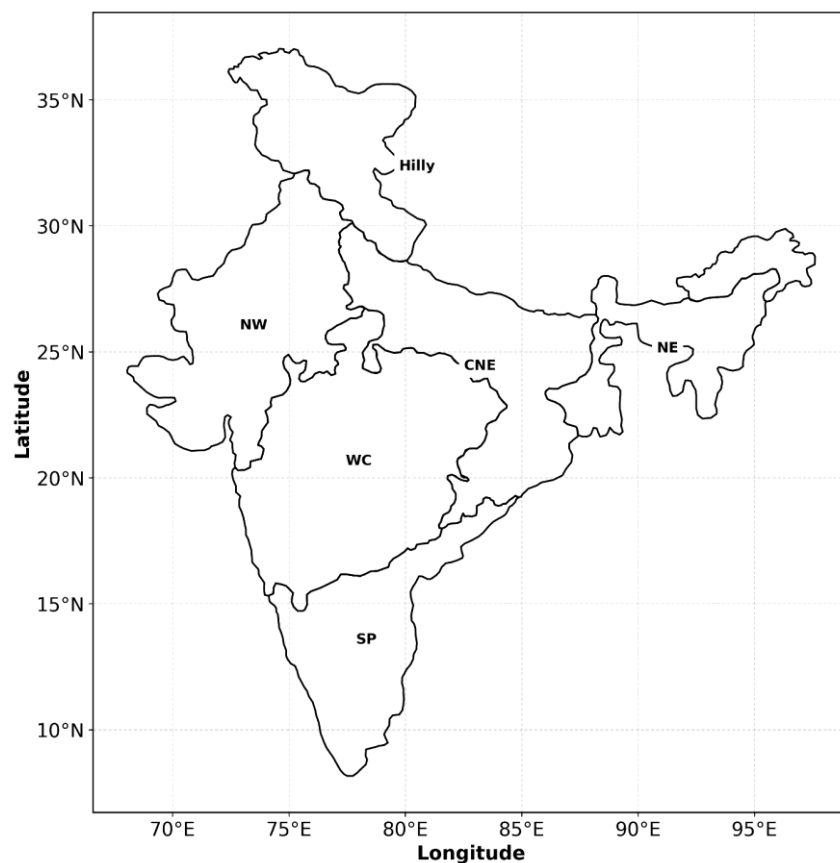


Figure 1. Map showing the homogeneous rainfall regions considered in this study which are West Central India (WC), North East India (NE), North West India (NW), Hilly regions, Southern Peninsular India (SP) and Central North East (CNE).

Table 1. CMIP6 models used in the present study.

Sr. No.	Models	Spatial resolution (lon/lat)	Country
Model 1	CanESM5-CanOE	128 × 64	Canada
Model 2	CanESM5	128 × 64	Canada
Model 3	BCC-CSM2-MR	320 × 160	China
Model 4	CMCC-CM2-SR5	288 × 192	Italy
Model 5	CMCC-ESM2	288 × 192	Italy
Model 6	CNRM-ESM2-1	256 × 128	France
Model 7	CNRM-CM6-1-HR	256 × 128	France
Model 8	FGOALS-f3-L	360 × 180	China
Model 9	GFDL-ESM4	288 × 180	USA
Model 10	FIO-ESM-2-0	288 × 192	China
Model 11	INM-CM5-0	180 × 120	Russia
Model 12	MCM-UA-1-0	96 × 80	USA
Model 13	KACE-1-0-G	192 × 144	Korea
Model 14	MIROC-ES2L	128 × 64	Japan
Model 15	MRI-ESM2-0	320 × 160	Japan

STUDY AREA

Over the Indian subcontinent, which lies north of the equator, between 8° and 37° N and 68° and 97° E, this study assesses the CMIP6 model's performance by simulating ET. From tropical in the south to alpine near the Himalayas in the north, India boasts a distinct climate. Its geographic position, and size characteristics also influence certain weather conditions. We have analyzed the ET over six homogeneous Indian rainfall regions, Hilly region, Central North East (CNE), North West (NW), North East (NE), West Central (WC) and Southern Peninsular (SP) regions, as shown in Figure 1.

DATA AND METHODOLOGY

The current study uses monthly data from selected historical simulations of 15 CMIP6 models covering the years 1985–2014 (Erying et al., 2016). Using two SSPs (SSP2-4.5 and SSP5-8.5), the monthly projection data of evapotranspiration for mid future (MF) and far future (FF) are computed. We observed the variability during monsoon season (June to September, JJAS). Future changes in JJAS mean ET for MF (2040-2069) and FF (2070-2099), were analyzed using CMIP6 models under SSP2-4.5 and SSP5-8.5, relative to 1985-2014. Further, we also computed the MF and FF for monthly climatology. We have demonstrated the model quality (Table 1) considering 15 models and comparing the spatial and temporal variability.

These datasets may be accessed with the given ESGF link, <https://esgf-node.llnl.gov/search/cmip6> and the models used for the study are illustrated in Table 1. We have taken the ensemble mean of ET to analyse the mid future and far future variability under SSP2-4.5 and SSP5-8.5 across the Indian region. Additionally, the changes in ET are also observed by taking monthly climatology for historical, mid future and far future periods.

RESULTS AND DISCUSSION

Future changes of ET in Mid-Future (MF) and Far-Future (FF) under SSP2-4.5

Figure 2 illustrates the projected changes in ET over the study region under the SSP2-4.5 scenario, highlighting noticeable spatial and inter-model variability in MF. While the overall direction and intensity of ET change differ across regions and models, the most considerable inconsistencies are observed over the WC and NW zones. Notably, KACE-1-0-G, FGOALS-f3-L, CanESM5 and CanESM5-CanOE project an increase in ET over study regions, whereas remaining suggest a decline.

A reduction in ET may reflect decreased vegetation cover, soil moisture, and less precipitation, which indicate weak land-atmosphere interactions (Mondal et al., 2021). However, increased ET indicates improved canopy functioning, potentially resulting in increase in precipitation regionally (Liu et al., 2008; Wang et al., 2019). However, the divergence in model projections for the same regions and scenario, underscores the uncertainties inherent in ET response simulations. These inconsistencies arise from differences in model structures, land surface parameterizations, and canopy-climate interactions.

Under the SSP2-4.5 climate scenario, projected changes in ET for the FF period, indicate a general increase in magnitude across several regions of India (Figure 3). This rise in ET is closely linked to elevated surface temperatures, which enhance atmospheric moisture demand and intensify the latent heat flux, thereby increasing ET rates. Such conditions have been associated with increased risk of heat stress and reduced water availability, particularly in water-limited ecosystems (Mondal et al., 2021; Niang et al., 2014).

Model-specific responses, however, exhibit substantial spatial and structural variability. For example, simulations from MRI-ESM2-0 and FIO-ESM-2-0 project a decline in ET over the NW, WC, and CNE regions. This projected reduction may imply intensified thermal extremes in these areas, as lower ET often corresponds to reduced vegetation activity, declining soil moisture, and a weakened land–atmosphere feedback mechanism (Seneviratne et al., 2010).

In contrast, several other models, including MCM-UA-1-0, KACE-1-0-G, INM-CM5-0, INM-CM4-8, GFDL-ESM4, FGOALS-f3-L, CMCC-CM2-SR5, CanESM5, BCC-CSM2-MR and CanESM5-CanOE, project an increase in ET over

these same regions. These diverging trends highlight the uncertainty in model representations of hydrological processes, particularly the interactions between temperature, vegetation dynamics, and soil moisture availability (Mueller and Seneviratne, 2012). Such inter-model variability underscores the importance of multi-model evaluation to improve the understanding of ET responses under climate change, especially over homogeneous rainfall regions of India. Over the Hilly region, all the models used for this study predicted that the ET will increase. Over NE and SP regions, most of the models predict rise in ET except MIROC-ES2L, GFDL-ESM4 and FIO-ESM-2-0.

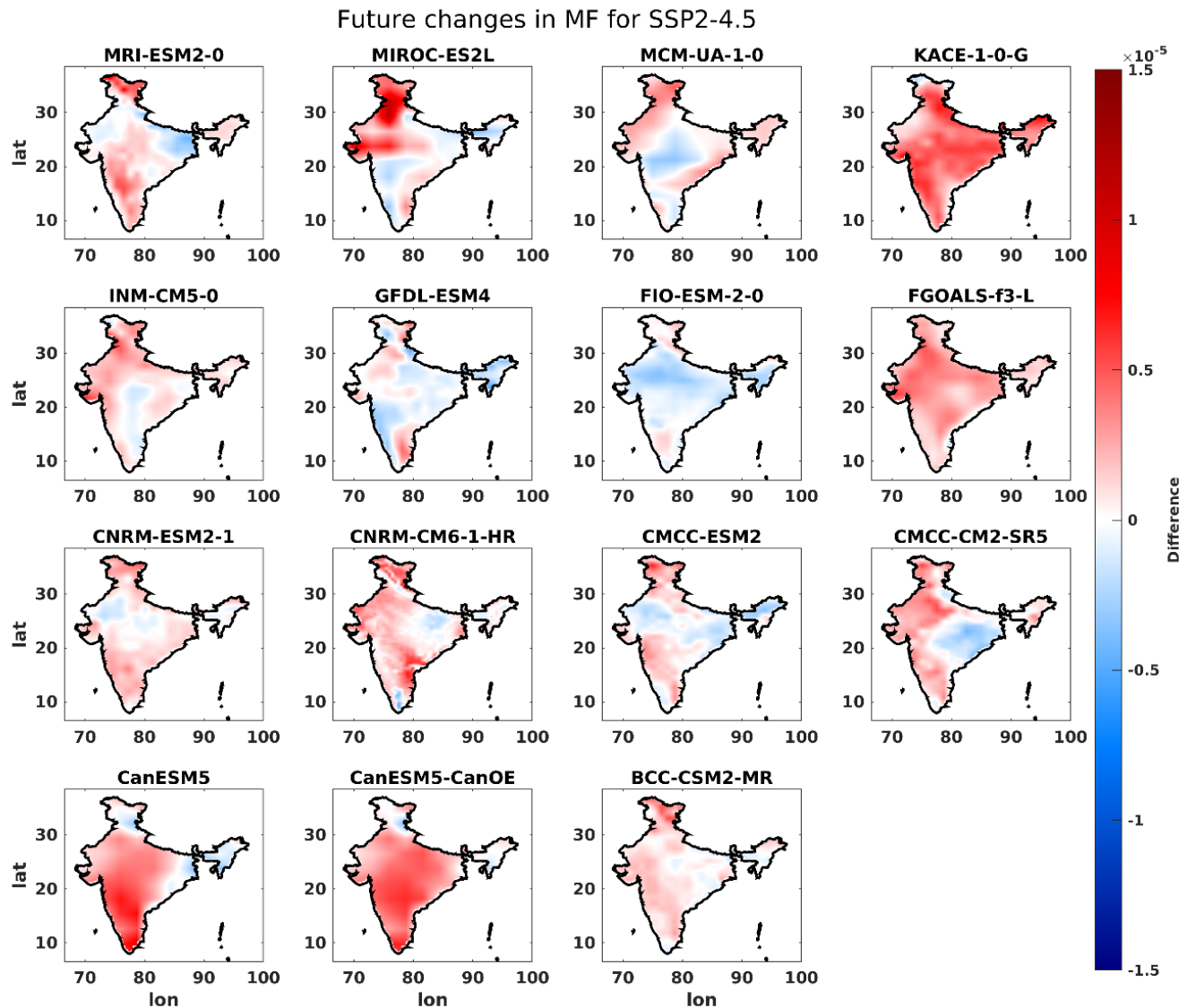


Figure 2. Spatial distribution of projected change (future–historical) in ET for extreme emission scenario SSP2-4.5 for mid future (MF) during 2040–2069 with historical data from 1985 to 2014.

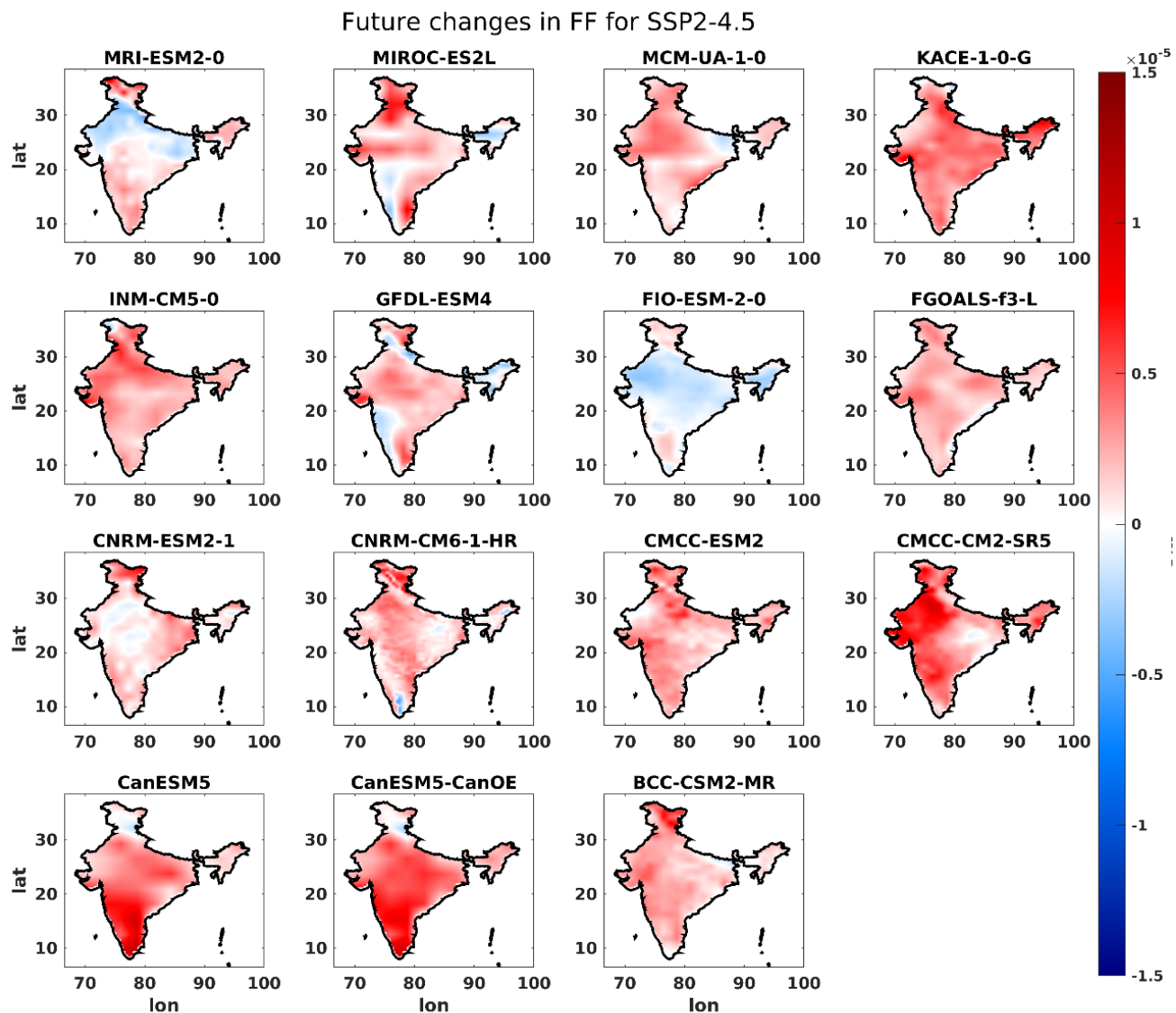


Figure 3. Spatial distribution of projected change (future–historical) in ET for extreme emission scenario SSP2-4.5 for far future (FF) during 2070–2099 with historical data from 1985 to 2014.

Future changes of ET in Mid Future (MF) and Far Future (FF) under SSP5-8.5

Projections from CMIP6 climate models suggest that ET is likely to increase across India in the future, as shown in Figure 4. KACE-1-0-G, INM-CM5-0, CMCC-CM2-SR5, FGOALS-f3-L, CanESM5-CanOE, CNRM-ESM2-1, and CanESM5 show a rise in ET under future climate conditions, suggesting an active hydrological cycle driven by warmer temperature. However, few models, such as MRI-ESM2-0, MIROC-ES2L, MCM-UA-1-0, FIO-ESM-2-0, and GFDL-ESM4, show either little change or even a decrease in ET in the MF. FIO-ESM-2-0 and GFDL-ESM4 indicating a decline in ET across large parts of India, contrasting sharply with others like CMCC-CM2-SR5 and CanESM5, which show very similar patterns of increasing ET.

The projections grow more in line with the FF. Nearly every model predicts that ET will increase in these regions due to increases in vegetation cover and rainfall. This comparison of MF and FF projections highlights how intricate and location-specific ET variations are in high-emission scenarios. The contrasting projections of these models for the MF highlight the complexity of ET distribution under SSP5-8.5, underscoring the need for further investigation to elucidate the underlying causes of the divergent patterns. There are also some notable regional trends. Reduced ET in the MF over the CNE, WC, and NW regions is projected by MRI-ESM2-0. On the other hand, GFDL-ESM4 and MRI-ESM2-0 indicate a decrease in ET in NW India, whilst INM-CM4-8 indicates an increase. However, the models generally concur over the hilly areas.

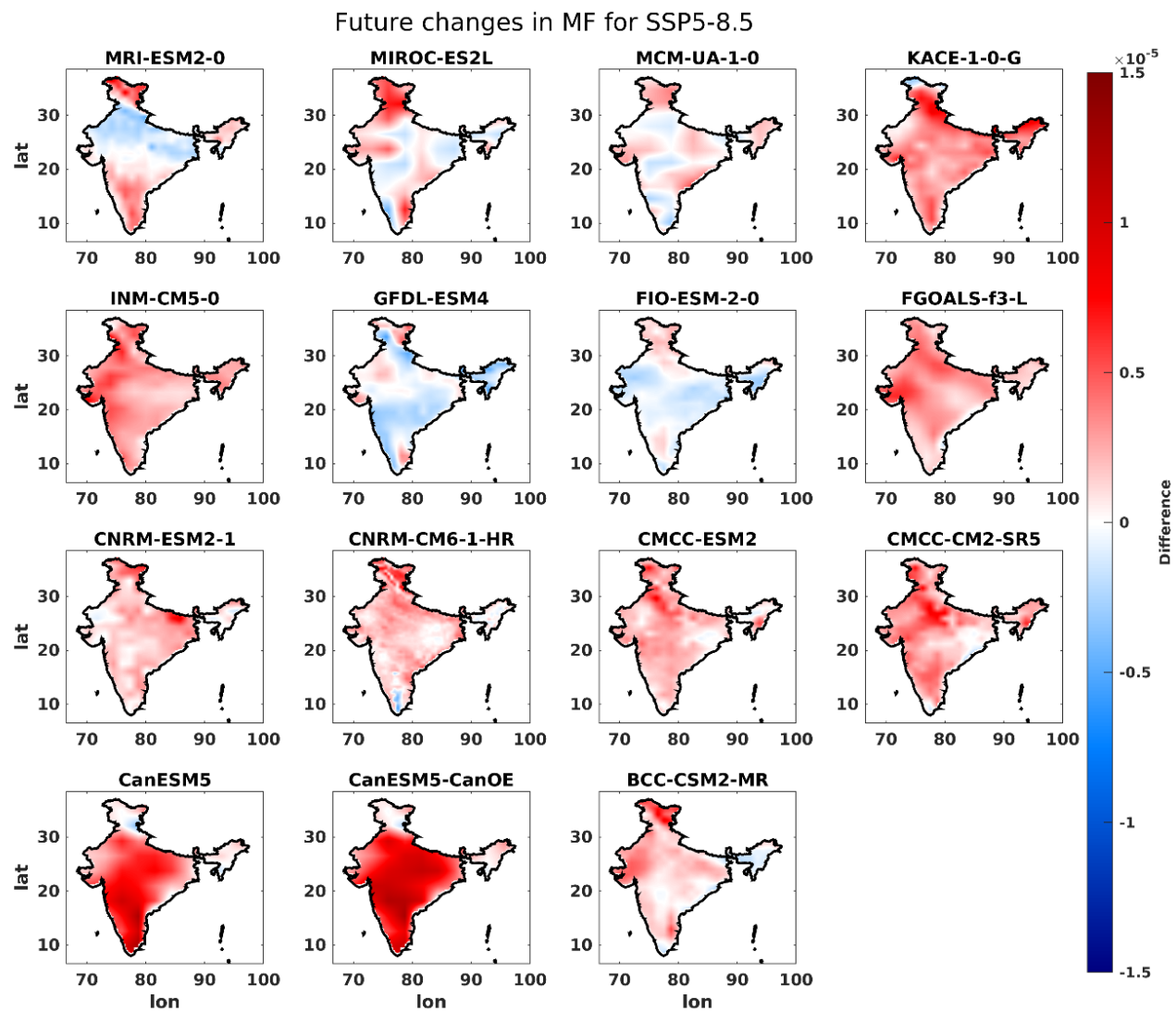


Figure 4. Spatial distribution of projected change (future–historical) in ET for extreme emission scenario SSP5-8.5 for mid future (MF) during 2040–2069 with historical data from 1985 to 2014.

While the overall trend indicates that ET is rising in many regions, the variation across models, particularly in the MF, emphasizes the need for a deeper understanding of the regional factors.

Compared to the future changes of ET in MF, most of the models predict that the magnitude of ET distribution increases over CNE, Hilly, NE, SP and WC regions for future changes of ET in FF (Figure 5). Interestingly, changes in FF from the model MRI-ESM2-0, predicts lesser magnitude over the NW region as compared to MF. GFDL-ESM4, and FIO-ESM-2-0 show the decline in ET variability.

Monthly climatology of ET

Figure 6 shows the monthly climatology of ET over the Indian region, comparing with outputs from CMIP6 models for the historical period, mid-future scenario (SSP2-4.5), and far-future scenario (SSP5-8.5). Each line represents an individual model's monthly ET values, while the bold black lines show

the ensemble means for each scenario. Across all the models and time periods, ET exhibits a pronounced seasonal cycle, peaking consistently during the monsoon months (JJAS). This seasonal peak corresponds to the period of maximum precipitation and vegetation activity in India, when soil moisture and canopy transpiration are at their highest. In the historical period, models show good agreement in ET patterns, with peak values aligning well during JJAS. However, under SSP5-8.5, the magnitude of ET increases during the monsoon season. This enhancement reflects projected increases in surface temperature and atmospheric moisture demand, leading to stronger evapotranspiration fluxes (Wang et al., 2019; Mondal et al., 2021). The SSP5-8.5 scenario shows a more pronounced increase compared to SSP2-4.5, indicating that stronger radiative forcing and warming scenarios drive higher ET.

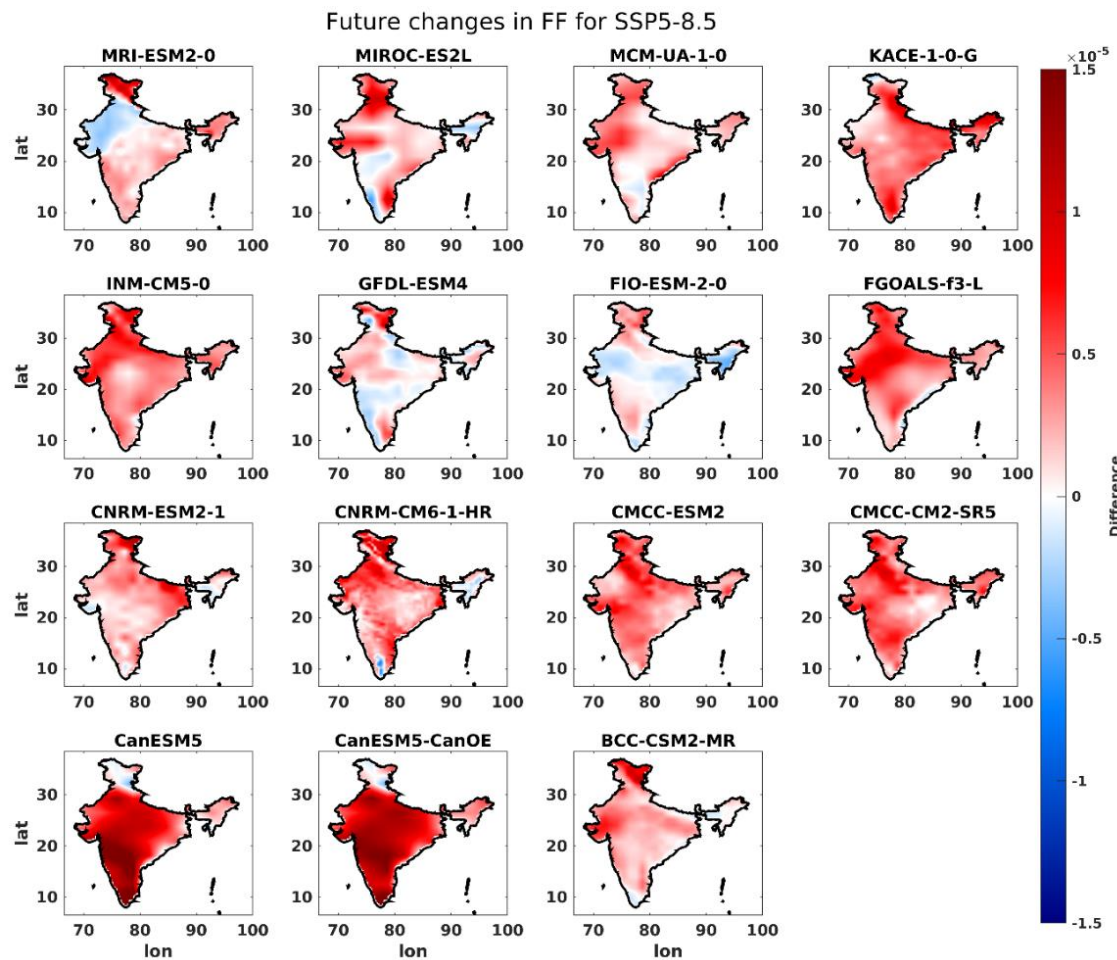


Figure 5. Spatial distribution of projected change (future–historical) in ET for extreme emission scenario SSP5-8.5 for far future (FF) during 2070–2099 with historical data from 1985 to 2014

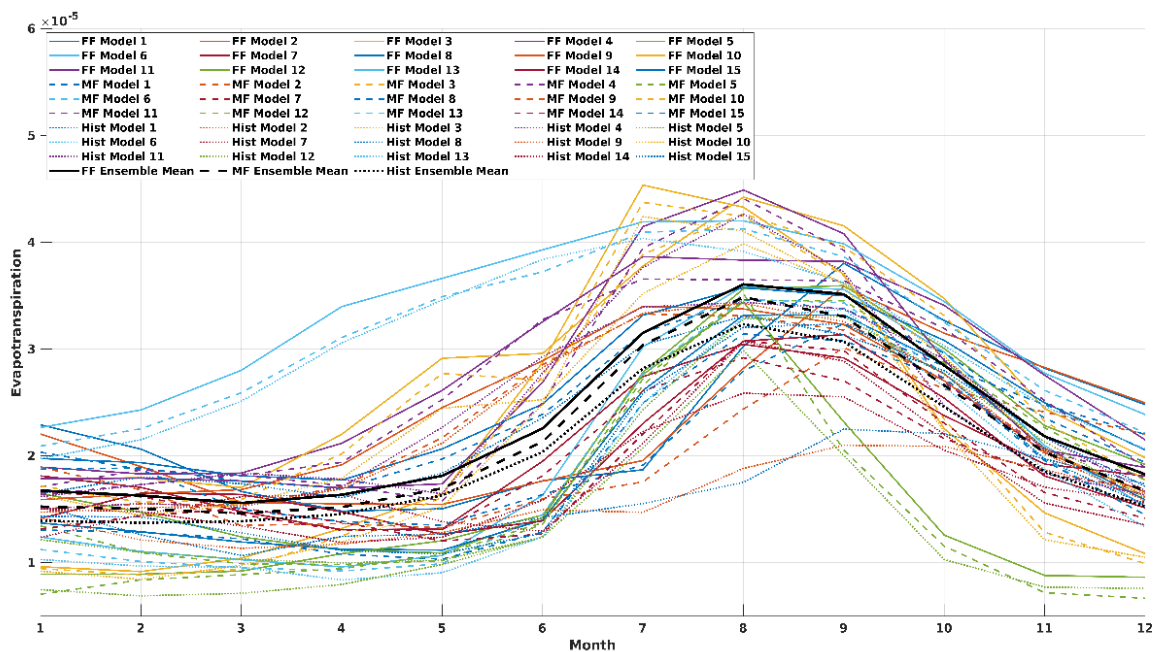


Figure 6. Monthly climatology of ET for historical data (1985–2014), mid future projections (2040–2069) and far future projections (2070–2099) under CMIP6 models.

Notably, there is considerable inter-model variability, especially in the far future scenarios. While ensemble means provide a general trend of increasing ET, the spread between individual models is large, in some cases exceeding the magnitude of change in the ensemble mean. Some models (FIO-ESM-2-0, MRI-ESM2-0), exhibit relatively lower ET in the far future, particularly in NW and CNE India, possibly reflecting regional drying or vegetation stress. In contrast, CanESM5, KACE-1-0-G, and CMCC-CM2-SR5 project a more robust increase in ET, suggesting enhanced vegetation activity or elevated surface energy partitioning toward latent heat flux.

CONCLUSIONS

ET is a fundamental key component of the hydrological cycle and plays a crucial role in the surface energy balance, with strong linkages to precipitation and land-atmosphere interactions. Understanding its future trajectory is therefore essential, particularly in the context of climate change. This study investigates projected changes in ET over India using an ensemble of fifteen CMIP6 models under two emission scenarios: SSP2-4.5 and SSP5-8.5. Under the high-emission scenario (SSP5-8.5), ET is projected to increase during the MF period and intensify further in the FF. This rise is especially pronounced during the monsoon season (JJAS), consistent with global projections and indicative of enhanced precipitation, vegetation activity, and land surface feedbacks. The ensemble mean of ET also shows increased variability during JJAS, suggesting greater uncertainty in hydrological responses under changing climate conditions. Notably in the FF, ET variability is expected to rise, while the historical mean may decline by a factor of three in certain regions, indicating a shift in the underlying dynamics of moisture availability and energy partitioning. These changes have critical implications for water resource management, as increased ET could lead to higher water loss from soil and vegetation, potentially stressing freshwater availability. Similarly, shifts in ET patterns may affect crop water requirements, posing challenges for irrigation planning and agricultural productivity, particularly in rain-fed regions. Future research should focus on quantifying the relationships between ET, precipitation, and surface temperature across homogeneous rainfall zones in India. Such studies will provide a more detailed understanding of the regional impacts of climate change on vegetation dynamics and agro-ecosystems. These insights are essential for informing climate-resilient agricultural practices and evidence-based policy planning in India's water and land management sectors.

Acknowledgements

The authors express gratitude to the relevant agencies of CMIP6 for providing the openly accessible datasets used in the research. The datasets used for this research are accessible to the public. The authors acknowledge to the DST sponsored

Varahamihira Centre of Excellence in Climate Change, University of Allahabad, for providing infrastructural facilities.

Author Credit Statement

The first author of the current investigation (GS) conceptualizes the objective of the study and wrote the original manuscript. The second author (HS) performed the data analysis, editing and revision under the guidance of the third author (SKS). The manuscript was edited by GS, SKS and HS and evaluated by SKS.

Data availability

Data will be provided upon request, though all data used in the current work are in the public domain. We have all the code used in this work, which can be supplied on reasonable request.

Compliance with ethical standards

We agree on the publication ethics and adhere to copyright norms. The authors declare no competing interests.

REFERENCES

- Abdallah, M., Zhang, K., Singh, S. K., Abdi, M. J., Elameen, A. M., Mohammed, A. A. and Elzain, H. E., 2025. Hydrological insights: Comparative analysis of gridded potential evapotranspiration products for hydrological simulations and drought assessment. *J. Hydrology: Regional Studies*, 57, 102113.
- Allen, R.G., Pereira, L.S., Raes, D. and Smith, M., 1998. Crop evapotranspiration-Guidelines for computing crop water requirements-FAO Irrigation and drainage paper 56. Fao, Rome, 300(9), D05109.
- Aragón-Hernández, J. L., Hernández González, L. A., Salas de León, D. A. and González Villarreal, F. J., 2024. Water availability: spatially distributed analysis and evaluation of input variables. *H2Open Journal*, 7(5), 333-350.
- Arnell, N. W. and Lloyd-Hughes, B., 2014. The global-scale impacts of climate change on water resources and flooding under new climate and socio-economic scenarios. *Climatic Change*, 122, 127-140.
- Checa-Garcia, R., Hegglin, M. I., Kinnison, D., Plummer, D. A. and Shine, K. P., 2018. Historical tropospheric and stratospheric ozone radiative forcing using the CMIP6 database. *Geophys. Res. Lett.*, 45(7), 3264-3273.
- Cook, B. I., Smerdon, J. E., Seager, R. and Coats, S., 2014. Global warming and 21 st century drying. *Climate dynamics*, 43, 2607-2627.
- Covey, C., Achuta Rao, K.M., Cubasch, U., Jones, P., Lambert, S.J., Mann, M.E., Phillips, T.J. and Taylor, K.E., 2003. An overview of results from the Coupled Model Intercomparison Project. *Global and Planet. Change*, 37(1-2), 103-133.
- Eyring, V., Bony, S., Meehl, G. A., Senior, C. A., Stevens, B., Stouffer, R. J. and Taylor, K. E., 2016. Overview of the Coupled Model Intercomparison Project Phase 6 (CMIP6) experimental design and organization. *Geoscientific Model Development*, 9(5), 1937-1958.
- Fu, G., Charles, S. P. and Yu, J., 2009. A critical overview of pan evaporation trends over the last 50 years. *Climatic change*, 97(1), 193-214.

- Kim, J. and Hogue, T. S., 2008. Evaluation of a MODIS-based potential evapotranspiration product at the point scale. *J. Hydrometeorology*, 9(3), 444-460.
- Kim, D., Ha, K. J. and Yeo, J. H., 2021. New drought projections over East Asia using evapotranspiration deficits from the CMIP6 warming scenarios. *Earth's Future*, 9(6), e2020EF001697.
- Kumar, N., Singh, S. K., Singh, P. K., Gautam, D. K., Patle, P., Pandey, H. K. and Chauhan, P., 2023. Water accounting of a trans-boundary river basin using satellite observations and WA+ framework. *Phys. Chem. Earth, Parts a/b/c*, 129, 103343.
- Lian, X., Piao, S., Huntingford, C., Li, Y., Zeng, Z., Wang, X., Ciais, P., McVicar, T.R., Peng, S., Ottlé, C. and Yang, H., 2018. Partitioning global land evapotranspiration using CMIP5 models constrained by observations. *Nature Climate Change*, 8(7), pp.640-646.
- Liu, M., Tian, H., Chen, G., Ren, W., Zhang, C. and Liu, J., 2008. Effects of land-use and land-cover change on evapotranspiration and water yield in China during 1900-2000. *J. Am. Water Res. Assn.*, 44(5), 1193-1207.
- Liu, X., Li, C., Zhao, T. and Han, L., 2020. Future changes of global potential evapotranspiration simulated from CMIP5 to CMIP6 models. *Atmosph. Oceanic Sci. Lett.*, 13(6), 568-575.
- Long, D., Longuevergne, L. and Scanlon, B. R., 2014. Uncertainty in evapotranspiration from land surface modeling, remote sensing, and GRACE satellites. *Water Res. Res.*, 50(2), 1131-1151.
- Lu, J., Wang, G., Li, S., Feng, A., Zhan, M., Jiang, T., Su, B. and Wang, Y., 2021. Projected land evaporation and its response to vegetation greening over China under multiple scenarios in the CMIP6 models. *J. Geophys. Res.: Biogeosciences*, 126(9), e2021JG006327.
- Mahanta, A. R., Rawat, K. S., Kumar, N., Szabo, S., Srivastava, P. K. and Singh, S. K., 2024. Assessment of multi-source satellite products using hydrological modelling approach. *Phys. Chem. Earth, Parts A/B/C*, 133, 103507.
- Meehl, G. A., Covey, C., McAvaney, B., Latif, M. and Stouffer, R. J., 2005. Overview of the coupled model intercomparison project. *Bull. Am. Meteorol. Soc.*, 86(1), 89-93.
- Mondal, A. R. P. I. T. A. and Mujumdar, P. P., 2015. Regional hydrological impacts of climate change: implications for water management in India. *Proc. Int. Assn. of Hydrological Sci.*, 366, 34-43.
- Mondal, S.K., Tao, H., Huang, J., Wang, Y., Su, B., Zhai, J., Jing, C., Wen, S., Jiang, S., Chen, Z. and Jiang, T., 2021. Projected changes in temperature, precipitation and potential evapotranspiration across Indus River Basin at 1.5–3.0 C warming levels using CMIP6-GCMs. *Science of the Total Environment*, 789, 147867.
- Mueller, B. and Seneviratne, S. I., 2014. Systematic land climate and evapotranspiration biases in CMIP5 simulations. *Geophys. Res. Lett.*, 41(1), 128-134.
- Mueller, B. and Seneviratne, S.I., 2012. Hot days induced by precipitation deficits at the global scale. *Proc. National Acad. Sciences*, 109(31), 12398-12403.
- Mueller, B., Hirschi, M., Jiménez, C., Ciais, P., Dirmeyer, P.A., Dolman, A.J., Fisher, J.B., Jung, M., Ludwig, F., Maignan, F. and Miralles, D.G., 2013. Benchmark products for land evapotranspiration: Land Flux-EVAL multi-data set synthesis. *Hydrology and Earth Sys. Sci.*, 17(10), 3707-3720.
- Niang, I., Ruppel, O.C., Abdrabo, M.A., Essel, C., Lennard, C., Padgham, J., Urquhart, P. and Descheemaeker, K., 2014. Africa. In: *Climate Change 2014: Impacts, Adaptation, and Vulnerability. Part B: Regional Aspects. Contribution of Working Group II to the Fifth Assessment (1199-1265)*. Cambridge University Press.
- Nooni, I.K., Hagan, D.F.T., Wang, G., Ullah, W., Lu, J., Li, S., Dzakupasu, M., Prempeh, N.A. and Lim Kam Sian, K.T., 2021. Future changes in simulated evapotranspiration across continental Africa based on CMIP6 CNRM-CM6. *Int. J. Environ. Res. and Public Health*, 18(13), 6760.
- O'Neill, B.C., Krieglner, E., Ebi, K.L., Kemp-Benedict, E., Riahi, K., Rothman, D.S., Van Ruijven, B.J., Van Vuuren, D.P., Birkmann, J., Kok, K. and Levy, M., 2017. The roads ahead: Narratives for shared socioeconomic pathways describing world futures in the 21st century. *Global Environmental Change*, 42, 169-180.
- Pan, S., Pan, N., Tian, H., Friedlingstein, P., Sitch, S., Shi, H., Arora, V.K., Haverd, V., Jain, A.K., Kato, E. and Lienert, S., 2020. Evaluation of global terrestrial evapotranspiration using state-of-the-art approaches in remote sensing, machine learning and land surface modeling. *Hydrology and Earth Syst. Sci.*, 24(3), 1485-1509.
- Peterson, T. C., Golubev, V. S. and Groisman, P. Y., 1995. Evaporation losing its strength. *Nature*, 377(6551), 687-688.
- Rawat, A., Kumar, D. and Khatri, B.S., 2024. A review on climate change impacts, models, and its consequences on different sectors: a systematic approach. *J. Water and Climate Change*, 15(1), 104-126.
- Riahi, K., Van Vuuren, D.P., Krieglner, E., Edmonds, J., O'Neill, B.C., Fujimori, S., Bauer, N., Calvin, K., Dellink, R., Fricko, O. and Lutz, W., 2017. The Shared Socioeconomic Pathways and their energy, land use, and greenhouse gas emissions implications: An overview. *Global Environ. Change*, 42, 153-168.
- Seneviratne, S.I., Corti, T., Davin, E.L., Hirschi, M., Jaeger, E.B., Lehner, I., Orlowsky, B. and Teuling, A.J., 2010. Investigating soil moisture-climate interactions in a changing climate: A review. *Earth-Science Rev.*, 99(3-4), 125-161.
- Singh, P., Srivastava, P. K. and Mall, R. K., 2021. Estimation of potential evapotranspiration using INSAT-3D satellite data over an agriculture area. In: *Agricultural Water Management (143-155)*. Academic Press.
- Singh, V. G., Singh, S. K., Kumar, N., Kumar, P., Gupta, P. K., Singh, P. K. et al., 2022. Water accounting using satellite products and water accounting plus framework in a semi-arid Betwa river basin, India. *Water*, 14(21), 3473.
- Song, Y. H., Chung, E. S. and Shahid, S., 2022. Uncertainties in evapotranspiration projections associated with estimation methods and CMIP6 GCMs for South Korea. *Science of the Total Environment*, 825, 153953.
- Stocker, T.F., Qin, D., Plattner, G.K., Alexander, L.V., Allen, S.K., Bindoff, N.L., Bréon, F.M., Church, J.A., Cubasch, U., Emori, S. and Forster, P., 2013. Technical summary. In: *Climate change 2013: the physical science basis. Contribution of Working Group I to the Fifth Assessment Report of the Intergovernmental Panel on Climate Change (33-115)*. Cambridge University Press.
- Taylor, K. E., Stouffer, R. J. and Meehl, G. A., 2012. An overview of CMIP5 and the experiment design. *Bull. Am. Meteorol. Soc.*, 93(4), 485-498.
- Wang, H., Xiao, W., Zhao, Y., Wang, Y., Hou, B., Zhou, Y., Yang, H., Zhang, X. and Cui, H., 2019. The spatiotemporal variability of evapotranspiration and its response to climate change and land use/land cover change in the three gorges reservoir. *Water*, 11(9), 1739.
- Wang, Z., Zhan, C., Ning, L. and Guo, H., 2021. Evaluation of global terrestrial evapotranspiration in CMIP6 models. *Theoretical and Appl. Climatology*, 143, 521-531.

- Yahaya, I., Li, Z., Zhou, J., Jiang, S., Su, B., Huang, J., Xu, R., Havea, P.H. and Jiang, T., 2024. Estimations of potential evapotranspiration from CMIP6 multi-model ensemble over Africa. *Atmospheric Res.*, 300, 107255.
- Yao, Y., Liang, S., Li, X., Liu, S., Chen, J., Zhang, X., Jia, K., Jiang, B., Xie, X., Munier, S. and Liu, M., 2016. Assessment and simulation of global terrestrial latent heat flux by synthesis of CMIP5 climate models and surface eddy covariance observations. *Agricultural and Forest Meteorology*, 223, 151-167.
- Zeng, Z., Piao, S., Lin, X., Yin, G., Peng, S., Ciais, P. and Myneni, R. B., 2012. Global evapotranspiration over the past three decades: estimation based on the water balance equation combined with empirical models. *Environ. Res. Lett.*, 7(1), 014026.
- Zhang, Y., Peña-Arancibia, J.L., McVicar, T.R., Chiew, F.H., Vaze, J., Liu, C., Lu, X., Zheng, H., Wang, Y., Liu, Y.Y. and Miralles, D.G., 2016. Multi-decadal trends in global terrestrial evapotranspiration and its components. *Scientific Reports*, 6(1), 19124.

Received on: 19-02-2025; Revised on: 19-08-2025 ; Accepted on: 24-08-2025

GUIDE FOR AUTHORS

The Journal of Indian Geophysical Union (JIGU), a SCI Journal published bimonthly by the Indian Geophysical Union (JIGU), is an inter disciplinary journal from India that publishes high-quality research in earth sciences with special emphasis on the topics pertaining to the Indian subcontinent and the surrounding Indian Ocean region. The journal covers several scientific disciplines related to the Earth sciences such as solid Earth Geophysics, geology and geochemistry, apart from marine, atmosphere space and planetary sciences. J-IGU welcomes contributions under the following categories:

*Research articles, short notes and students section reporting new findings, results, etc.

*Review articles providing comprehensive overview of a significant research field.

In addition, JIGU also welcomes short communications, after communications and report on scientific activity, book reviews, news and views, etc.

The manuscript should be submitted electronically as a single word format (.doc file) including the main text, figures, tables, and any other supplementary information along with the signed "Declaration Letter". The manuscript should be submitted by email (jigul1963@gmail.com) to the Chief Editor.

After acceptance of the manuscript the corresponding author would be required to submit all source files (text and Tables in word format) and figure in high resolution standard (*.jpg, *.tiff, *.bmp) format. These files may be submitted to JIGU as a single *.zip file along with the "Copyright Transfer Statement".

IMPORTANT INFORMATION

Ethics in publishing: J-IGU is committed to ensuring ethics in publication and takes a serious view of plagiarism including self-plagiarism in manuscripts submitted to the journal. Authors are advised to ensure ethical values by submitting only their original work and due acknowledgement to the work of others used in the manuscript. Authors must also refrain from submitting the same manuscript to more than one journal concurrently, or publish the same piece of research work in more than one journal, which is unethical and unacceptable. Editor of JIGU is committed to make every reasonable effort to investigate any allegations of plagiarism brought to his attention, as well as instances that come up during the peer review process and has full authority to retract any plagiarized publication from the journal and take appropriate action against such authors if it is proven that such a misconduct was intentional.

Similarly, Editor and Reviewers are also expected to follow ethical norms of publishing by ensuring that they don't use any unpublished information, communicated to them for editorial or review purpose, in their own research without the explicit written consent of the author. They are also expected to keep manuscript' data/ observations/ any other information related to the peer review confidential to protect the interest of the authors. Reviewers should refrain from reviewing the manuscripts in which they have conflicts of interest resulting from competitive, collaborative, or other relationships or connections with any of the authors, companies, or institutions connected to the manuscript.

Conflict of interest

All authors are requested to disclose any actual or potential conflict of interest including any financial, personal or other relationships with other people or organizations within three years of beginning the submitted nor that could inappropriately influence, or be perceived to influence, their work.

Submission declaration

Submission of a manuscript implies that the work has not been published previously and it is not under consideration for publication elsewhere, and that if accepted it will not be published elsewhere in the same or any other form, in English or in any other language, without the written consent of the publishers. It also implies that the authors have taken necessary approval from the competent authority of the institute/organization where the work was carried out.

Copyright

After acceptance of the manuscript the corresponding author would be required to sign and submit the "Copyright Transfer Statement".

MANUSCRIPT PREPARATION

The corresponding author should be identified (include E-mail address, Phone/Mobile number). Full affiliation and postal address must be given for all co-authors.

Abstract:

An abstract of not more than 300 words must be included.

Text:

The manuscript should be structured to include a front page containing the title, Author(s) name, affiliation and address of the institute, where the work was carried out, and 5-to-6 Key words. Author(s) present address, if different from the above mentioned address, may be given in the footnote. The corresponding author should be identified with an asterisk and his/her email ID should be provided. This page should be followed by the main text consisting of Abstract, Introduction, Methods/ Techniques/ Area description, Results, Discussion, Conclusions, Acknowledgements, and References. Tables and Figures with captions should be inserted at the end of main text. It should not be inserted in the body of the text.

Figures/ Illustrations:

figures should be provided in camera-ready form, suitable for reproduction (which may include reduction) without retouching. Figures in high-resolution (at least 300 dpi) standard formats (*.jpg, *.tiff, *.bmp) are acceptable. Figures should be numbered according to their sequence in the text. References should be made in the text to each figure. Each figure should have a suitable caption.

Tables:

Authors should take note of the limitations set by the size and layout of the journal. Table should not exceed the printed area of the page. They should be typed on separate sheets and details about the tables should be given in the text. Heading should be brief. Large tables should be avoided and may be provided as supplementary information, if required.

Equations:

Equations should be numbered sequentially with Arabic numerals and cited in the text. Subscripts and Superscripts should be set off clearly.

Equation writing software that presents each equation as an object in MS Word will be accepted. Style and convention adopted for the equations should be uniform throughout the paper.

References:

All references to publications cited in the main text should be presented as a list of references in order following the text and all references in the list must be cited in the text. References should be arranged chronologically, in the text. The list of references should be arranged alphabetically at the end of the paper.

References should be given in the following form:

Kaila, K.L., Reddy PR., Mall D.M., Venkateswarlu, N., Krishna V.G. and Prasad, A.S.S.S.R.S., 1992, Crustal structure of the west Bengal el eon deep seismic sounding investigations. Geophys. J. Int., 1,45-66.

REVIEW PROCESS:

All manuscripts submitted to the journal are peer-reviewed. It is advisable to send the contact details of 4 potential reviewers along with the manuscript to expedite the review process. Editor has the option to select reviewers from the list or choose different reviewers. The review process usually takes about 3 months. All enquiries regarding the manuscript may be addressed to the Chief Editor.

GALLEY PROOF:

Technical editing of manuscripts is performed by the editorial board. The author is asked to check the galley proof for typographical errors and to answer queries from the editor. Authors are requested to return the corrected proof within two days of its receipt to ensure uninterrupted proceedings. The editor will not accept new material in proof unless permission from the editorial board has been obtained for the addition of a "note added in proof". Authors are liable to be charged for excessive alterations to galley proof.

PUBLICATION CHARGES:

There are no page charges for publication. The corresponding author will receive a soft copy (pdf format) of his/her published article. Should the author desire to purchase reprints of his/her publication, he/she must send the duly signed Reprint Order Form (accompanies the galley proof and contains price details) along with the corrected galley proof to the Editor. The reprint charges must be paid within one month of sending the Reprint Order Form.

Any payment related to printing or purchase of reprints should be made in the form of a Demand Draft in the name of Treasurer, Indian Geophysical Union, payable at Hyderabad.

You may download the pdf file from:
<http://iguonline.in/journal/instructions.php>